OUKA
The University of Osaka
Institutional Knowledge Archive

Title	Volume holographic optical elements using patterned chiral liquid crystals
Author(s)	趙, 成龍
Citation	大阪大学, 2021, 博士論文
Version Type	VoR
URL	https://doi.org/10.18910/85248
rights	
Note	

The University of Osaka Institutional Knowledge Archive : OUKA

https://ir.library.osaka-u.ac.jp/

The University of Osaka

Doctoral Dissertation

Volume holographic optical elements using patterned chiral liquid crystals
(パターン配向カイラル液晶を用いた体積ホログラフィック光学素子に関する研究)

SeongYong Cho

January 2021

Graduate School of Engineering,
Osaka University

Table of Contents

Table of Contents i
Abstract v

Chapter 1 Introduction ..... - 1 -
1.1 Preface ..... - 1 -
1.2 Liquid crystals ..... - 3 -
1.2.1 Cholesteric liquid crystals ..... - 4 -
1.2.2 Blue phases ..... - 8 -
1.3 Volume HOEs based on chiral liquid crystals ..... - 13 -
1.4 Photoalignment technology ..... - 16 -
1.5 Motivation and contents of this dissertation ..... - 19 -

Chapter 2 Transparent hologram and waveguide hologram with patterned cholesteric liquid crystals ..... - 21 -
2.1 Introduction ..... - 21 -
2.2 Theoretical background ..... - 22 -
2.3 Transparent computer-generated hologram ..... - 24 -
2.3.1 Device fabrication and materials ..... - 24 -
2.3.2 Spectral measurement ..... - 26 -
2.3.3 Hologram playback ..... - 27 -
2.4 Visible playback of BB hologram ..... - 29 -
2.5 Transparent computer-generated waveguide holography ..... - 31 -
2.5.1 Device design and fabrication ..... - 32 -
2.5.2 Characterization of waveguide holography ..... - 33 -
2.6 Discussion ..... - 35 -
2.7 Conclusion ..... - 37 -

Chapter 3 Orientation control of 3D self-organized cubic blue phases for omnidirectional circular polarization-selective holograms ..... - 39 -
3.1 Introduction ..... - 39 -

3.2 Field-induced reorientation of blue phase I ..... - 41 -
3.2.1 Sample fabrication and materials ..... - 41 -
3.2.2 Field-induced reorientation mechanism ..... - 42 -
3.2.2.1 Effect on field-induced focal conic state ..... - 45 -
3.2.2.2 Effect on field-induced tetragonal blue phase X ..... - 48 -
3.3 Omnidirectional circular polarization-selective hologram ..... - 50 -
3.3.1 Background ..... - 51 -
3.3.2 Device design and fabrication ..... - 57 -
3.3.3 Hologram generation at various incident angles ..... - 59 -
3.4 Circular-polarized, large-angle, and reflective volume grating based on simple cubic BP II ..... - 60 -
3.4.1 Sample fabrication ..... - 60 -
3.4.2 Lattice structure in photo-patterned BP II ..... - 61 -
3.4.3 Electro-optic response of slanted BP II ..... - 64 -
3.4.4 Switchable deflection behavior from the proposed device ..... - 66 -
3.5 Discussion ..... - 68 -
3.6 Conclusion ..... - 69 -

Chapter 4 Emission direction-controllable photonic crystal laser based on slanted cholesteric liquid crystals ..... - 71 -
4.1 Introduction ..... - 71 -
4.2 Device design and its photonic band structure ..... - 73 -
4.3 Off-axis laser emission ..... - 76 -
4.3.1 Device fabrication and materials ..... - 76 -
4.3.2 POM texture and transmission spectrum ..... - 79 -
4.3.3 Transmission electron microscope images ..... - 80 -
4.3.4 Laser emission characteristics ..... - 81 -
4.4 Emission-direction tuning through external stimuli ..... - 83 -
4.4.1 Materials ..... - 84 -
4.4.2 Laser emission characteristics ..... - 84 -
4.5 Discussion ..... - 88 -
4.6 Conclusion ..... - 89 -

Chapter 5 Conclusion ..... - 91 -

Bibliography ..... - 94 -
Acknowledgments ..... - 104 -
Achievements ..... - 105 -

Appendices ..... - 109 -
Appendix A. Berreman's 4 × 4 matrix ..... - 109 -
Appendix B. Gerchberg-Saxton algorithm ..... - 114 -
Appendix C. Simulation of diffraction pattern ..... - 116 -
C. 1 Rayleigh-Sommerfeld diffraction ..... - 116 -
C.2 Fresnel diffraction ..... - 118 -
C.3 Fraunhofer diffraction ..... - 120 -

Abstract

In this dissertation, volume holographic optical elements (HOEs) with advanced optical functionalities were designed and fabricated using self-organized chiral liquid crystals (LCs). Two types of chiral LCs are used in this study: cholesteric liquid crystals (ChLCs) with one-dimensional (1D) helical structures and blue phases (BPs) with three-dimensional (3D) cubic structures. The HOEs operate based on the Bragg-Berry (BB) effect for which full wavefront control of reflected optical phase from 0 to 2π radians is enabled by modulating the alignment of the LC molecules from 0 to π radians on a substrate. Various methods used to manipulate the structures of chiral LCs and achieve the desired optical effects are described such as photo-alignment technologies. The chiral LCs have a number of advantages such as circular-polarization (CP) selectivity, tunable optical effects through external stimuli, and simple fabrication procedures owing to self-organized nanostructures, which are distinct from other technologies such as conventional HOEs and metamaterials. This dissertation is organized into five chapters, which are summarized below.

Chapter 1: Introduction

The background, purpose, and overview of the dissertation are described. An introduction to diffractive optical elements such as conventional volume HOEs and chiral LC-based HOEs, along with the fundamental optical properties of chiral liquid crystals, is also provided.

Chapter 2: Transparent hologram and waveguide hologram with patterned cholesteric liquid crystals

A completely transparent computer-generated hologram (CGH) in the visible light region is realized using a ChLC. Because ChLCs have a sinusoidal dielectric tensor distribution along the helical axis, they possess only a single Fourier component, resulting in the suppression of all higher-order reflections. The angular dependent Bragg reflection bands of ChLCs is performed to show the fact that the higher-order reflections are suppressed for all angles of incidence accessible from free-space. Thus, using a ChLC that reflects only infrared light, a transparent CGH is achieved through the BB effect, i.e., 0 – 2π full control of reflected optical phase is enabled by varying the helix phase from 0 – π radians on a substrate. On the other hand, I show that the encoded hologram is played back by visible light illuminated at a sufficiently

large angle. Two types of optical designs are used to increase the incident angle: attaching an index-matching prism on the device, and integrating the device with a waveguide layer. The proposed device will be useful for practical applications where transparency is required, such as security elements and augmented realities.

Chapter 3: Orientation control of self-organized cubic blue phases for omnidirectional circular polarization-selective holograms

Although the ChLCs described in Chapter 2 show the CP selectivity when illuminated by light along the helical axis, the CP selectivity disappears for a light illuminated at large angles because the dielectric tensor distribution deviates from a complete sinusoidal wave. Thus, it is difficult to realize HOEs with the capability of omnidirectional CP selectivity using ChLCs. Moreover, previous technologies such as conventional HOEs and metasurfaces require complex designs and fabrication procedures of 3D chiral structures for omnidirectional CP selectivity.

In this chapter, two types of HOEs with advanced functionalities are demonstrated using self-organized cubic BPs. First, an omnidirectional CP-selective volume HOE is fabricated using a body-centered BP I based on BB effect. To achieve BB holograms using the BP, a facile method to control two independent crystal axes of BP I on a substrate by electric field treatment is first proposed. The BP I obtained from two field-induced intermediate phases has the (110) crystal plane parallel to the substrate and the [001] axis oriented along the surface anchoring, enabling the BB effect. The omnidirectional CP-selectivity is described through the analysis of the photonic band structures of the BP I, and the theory is experimentally supported by measuring the angular dependence of the Bragg reflection using a homogeneously aligned BP I. The omnidirectional CP-selective hologram is realized based on the BB effect, and is reconstructed for only a CP light upon all angles of incidence with a dichroic ratio of >85:1. The realization of an omnidirectional CP-selective device is extremely difficult using conventional HOEs or metamaterials because complex designs and fabrication processes of 3D structures are required.

Second, a defect-free and large-angle (~41.7°) deflector is demonstrated by introducing a periodic modulation of the LC director on a substrate. Through the analysis of Kossel diagrams and transmission spectra of the fabricated device, a possible orientation of the BP II lattice in the patterned cell is presented. In addition, a tunable and switchable light deflector is demonstrated by investigating the electro-optical characteristics of the fabricated device.

Chapter 4: Emission direction-controllable photonic crystal lasers based on slanted cholesteric liquid crystals

In this chapter, an emission direction-controllable photonic crystal (PC) band-edge laser is proposed using a ChLC-based HOE. In addition to the periodic modulation in a dielectric tensor along the helical axis, a short-pitch modulation of the LC director is introduced in a direction perpendicular to the helical axis through a polarization holography method, resulting in the cavity responsible for the laser oscillation to be slanted from the device normal. Using the slanted ChLC, a PC band-edge laser is realized with an emission angle of 30° from the helical axis. In addition, a theoretical prediction shows the emission angle can be tuned by modulating the helical pitch through external stimuli, which is experimentally demonstrated by realizing a PC laser with a tunable emission angle of approximately 4°. The proposed device possesses additional advantages such as a circular-polarized emission and a single beam emission, which can be applied to various applications such LiDARs and holography.

Chapter 5: Conclusion

The results and findings obtained in Chapters 2–4 are summarized, and main concluding remarks are provided. Further studies, various expected applications, and prospects are also discussed.

Chapter 1 Introduction

1.1 Preface

Light is important in our lives because it determines what we can see. Thus, the technologies to control light as we want are inseparable from our daily lives. The development of optical applications such as displays has been directed towards quickly and efficiently delivering light to the user's field of view. The devices consist of a number of conventional optical elements such as lenses, prisms, and polarizers to control light. The basic principles of conventional optical elements are the refraction and reflection of the light, allowing the control of a wavefront propagating through the medium by engineering the refractive index in the optical path. The wavefront is gradually accumulated during the propagation in conventional optical elements, resulting in change of amplitude, phase, and polarization of light. However, they require a sufficient thickness to control full 0-2π wavefront. In addition, such approaches are typically designed to realize only a single optical functionality, resulting in the limitation to miniaturize its size. Since compact and light-weight optical elements have been explosively required in various field such as wearable devices, various researches are being actively conducted through two approaches; directly decreasing the size of the device, and integrating several optical functionalities in a single device.

One of the intensively investigated technologies is metasurfaces, which locally manipulate the amplitude, phase, and polarization of light through appropriately designed nano-structures on a substrate, which enable the integration of a number of functionalities in an ultra-compact element [1–3]. The control of the size, shape, and orientation of the nanostructures allows various optical functionalities such as holograms [4, 5], lenses [6, 7], deflectors [1], and beam shapers [8] in a single platform. In addition, a negative refractive index [9] and a perfect light absorber [10] have been demonstrated from the infrared (IR) to the visible wavelength range. In particular, the development in algorithms to numerically obtain a complex light distribution for computer-generated holography (CGH) have enabled various optical functionalities to be integrated in a single device [11, 12]. Despite the significant advances in the metasurface such as a wide operation bandwidth and high light-conversion efficiency, such approaches still require complex vacuum technologies such as electron and focused-ion beam lithography to spatially control the nanostructures at a sub-wavelength scale.

Another approach is the use of holographic optical elements (HOEs) that enable arbitrary control of the wavefront of light. Since the hologram was first discovered by Gabor in 1948

[13], it has found various applications, such as diffractive optical components [14], displays [15, 16], and distributed feedback lasers (DFLs) [17, 18]. In particular, the development of the laser has enabled practical 3D holograms by Denisyuk [19] and Leith and Upatnieks [20]. Figure 1.1 shows the fabrication and reconstruction process of conventional HOEs. A reference beam and reflected or transmitted beam from a target object are superimposed over each other, creating an interference pattern. The interference pattern is recorded on a photo-reactive recoding plate such as a dichromated gelatin [21], silver-halide emulsion [22], photoresist [23], and photopolymer [24, 25], resulting in spatial modulation in the refractive index of the holographic plate. The encoded holograms are reconstructed by illuminating the reference beam on the HOEs.

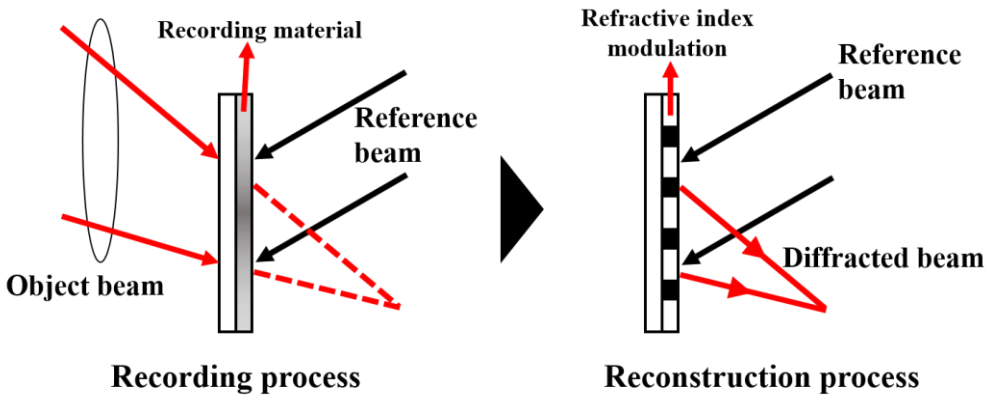


Figure 1.1 Principle of recoding and reconstruction process for HOEs.

Typically, HOEs are classified into two types, i.e., thin and thick (volume) holograms depending on the thickness of the recoding plate. The thin holograms are those where the thickness of the recording medium is less than the wavelength of the recording light. Recently, thin holograms with thickness of 60 nm have been reported using a topological insulator material of a Sb_2Te_3 film [26]. Thin holograms have the potential to be integrated with electronic devices such as smartphones. However, they show significantly low light-conversion efficiency because the incident light is diffracted in various directions. In addition, they show a high angular selectivity in the conversion efficiency. By contrast, volume holograms are those in which the thickness of a recording plate is larger than the wavelength of the recoding light, and enable a high light-conversion efficiency because its operation is based on a Bragg reflection. In addition, the narrow operation bandwidth allows them to be applied to compact diffractive optical elements (DOEs) such as wavelength-selective filters [27], deflectors [28], and out-couplers for waveguide displays [15, 16, 29]. Volume HOEs can be also used as a laser

cavity for distributed feedback owing to the capability of creating a periodic modulation in the refractive index [17, 18]. The narrow wavelength-selectivity of volume holograms provides a narrow emission bandwidth compared to semiconductor lasers. However, conventional HOEs require a complex laser interference setup for fabrication, and it is difficult to integrate multiple functionalities in a single device. In addition, several advanced functionalities such as omnidirectional circular-polarization (CP) selectivity or a tunable direction of the laser emission cannot be attained through the use of conventional volume HOEs because complex 3D structures are required.

Chiral liquid crystals (LCs) are a promising candidate to control light through the Bragg-Berry (BB) effect. One of the most widely used chiral LCs is cholesteric LCs (ChLCs), which have a one-dimensional (1D) periodic structure with a helical modulation along the optic axis [30, 31]. The Bragg reflected optical phase is controlled from 0 to 2π radians by modulating the orientation of the LC director from 0 to π radians on a substrate [32], enabling the fabrication of volume HOEs with advanced functionalities such as large-angle deflection [32–35], focusing [32, 36], hologram generation [37, 38], diffusion [39], and vortex beam generation [40, 41], in a sub-micrometer scale. Another approach is to use blue phase (BP) LCs, which also show the BB effect through the control of the azimuthal orientation of the cubic structure from 0 to π radians on a substrate. However, despite theoretical predictions [33], the demonstration of volume HOEs using BPs has been extremely rare because of the difficulty in spatially control the lattice orientation. In this study, focus is given to methods to manipulate the self-assembly process of chiral LCs to control light-matter interaction. Through such technologies, chiral LC-based volume HOEs were fabricated with advanced optical functionalities that cannot be achieved using previous technologies such as metasurfaces and conventional HOEs. This chapter provides a brief introduction of chiral LCs, including their BB effects. Next, the motivation and contents of this dissertation are provided.

1.2 Liquid crystals

LCs are a distinct state of matter that appear between crystalline solid and fluid liquid states, and simultaneously have the anisotropy of a solid state and the fluidity of a liquid state. Since they were first discovered by Feinitzer in 1888 [42], fundamental studies have been conducted to reveal the structure and orientation of LCs. LCs are categorized into various phase depending on their shape and orientation, as well as their appearance, as shown in Fig. 1.2. Nematic LCs (NLCs) have an orientation order in which the LC molecules are, on average, oriented in a direction described as the director. Smectic LCs have a positional order of LC molecules, and

are sub-categorized depending on their positional order and tilt of the LC molecules [31]. Because rod-like LCs are optically anisotropic, the light propagating in the LCs behave differently depending on the polarization with respect to the orientation of the LCs, enabling various optical devices by spatially controlling the LC orientation [30].

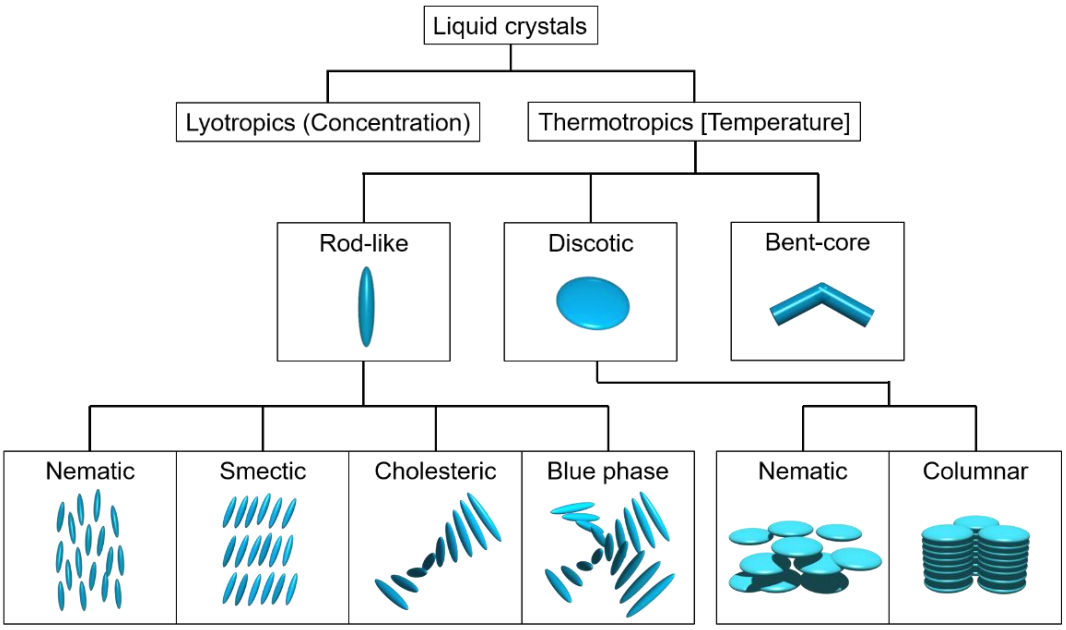


Figure 1.2 Categorization of LC phases. The LC phases are categorized depending on how they appear (controlling the concentration or temperature), their molecule shape, and the orientation of the LC molecules.

Among the various LC phases, in this dissertation, focus is given to two types of chiral LCs: ChLCs and BPs. In the section below, the fundamentals of the two chiral LCs including their structure and optical characteristics are given.

1.2.1 Cholesteric liquid crystals

ChLCs (also called chiral nematic phase) are formed through a uniaxial twist of the LC director along an optical axis. As shown in Fig. 1.3 (a), the LC molecules have a uniform in-plane orientation, and are continuously rotated in a direction perpendicular to the plane to minimize the elastic-free energy. The axis along which the LC molecules are rotated is called the helical axis. The helical pitch of the ChLC is defined as the distance within which the LC molecules are rotated by 2π radians along the helical axis. Owing to the periodicity of the LC orientation along the helical axis, the ChLC are regarded as having a 1D photonic crystal structure. The helical pitch is one of the important factors determining the optical properties of

ChLCs, such as the Bragg reflection wavelength. ChLCs can be obtained using cholesterol derivatives, but nowadays, most ChLCs are prepared by mixing a small amount of a chiral dopant in non-chiral LCs. Figure 1.3 (b) shows the chemical structure of a common cholesterol derivative and a right-handed chiral dopant (R-811). The handedness and helical pitch of the ChLCs are determined by the helical twisting power of the chiral molecules.

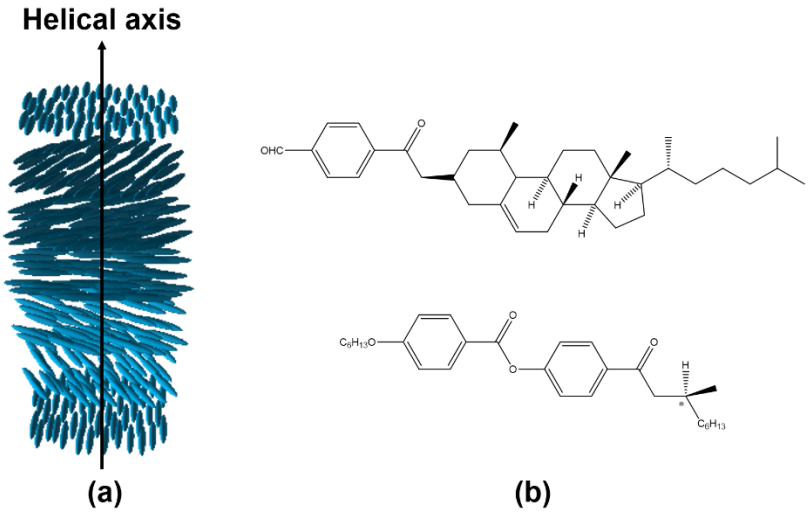


Figure 1.3 (a) A schematic of ChLCs. The LC molecules are continuously rotated along the helical axis. (b) A common cholesterol derivative (upper) and a chiral dopant (below).

The dielectric tensor distribution of ChLCs can be modeled by considering a continuous rotation of the LC director along the helical axis. The LC director in Fig. 1.4 can be expressed in a Cartesian coordinate system as follows:

$$\boldsymbol{n} = (\cos\phi\cos\theta, \cos\phi\cos\theta, \sin\theta), \tag{1.1}$$

where ϕ is the azimuthal angle of the LC director defined as the angle between the LC director projected on the *x*-*y* plane and *x*-axis, and θ is the tilt angle measured from the *x*-*y* plane.

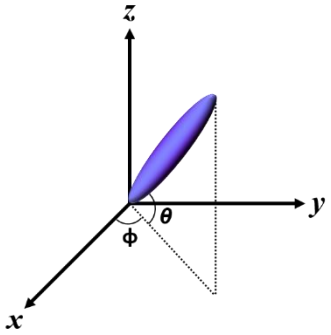


Figure 1.4 Anisotropic LC molecules placed in Cartesian coordinate system, where ϕ and θ are the azimuthal and tilt angles of the LC director, respectively.

In ChLCs, because the LC director is continuously twisted along the helical axis (*z*-axis), the azimuthal angle can be expressed by

$$\phi = \frac{2\pi}{p} z, \tag{1.2}$$

where *p* is the helical pitch. Thus, the dielectric tensor of ChLCs with a planar alignment (the tilt angle is zero) can be expressed by

$$\boldsymbol{n} = (\cos qz, \sin qz, 0), \tag{1.3}$$

where $q = 2\pi/p$. Here, the sign of *p* indicates the handedness of the helix; a positive values of *p* indicate a right-handed helix, whereas a negative sign shows a left-handed helix. The dielectric tensor distribution of ChLCs along the *z*-axis ($\boldsymbol{\varepsilon}$) can be obtained by considering the rotation of the diagonalzed dielectric constants as follows:

$$\begin{aligned} \boldsymbol{\varepsilon} &= \boldsymbol{R}_z(\phi)\boldsymbol{R}_y(\theta)\begin{pmatrix} \varepsilon_{\parallel} & 0 & 0 \\ 0 & \varepsilon_{\perp} & 0 \\ 0 & 0 & \varepsilon_{\perp} \end{pmatrix}\boldsymbol{R}_y^{-1}(\theta)\boldsymbol{R}_z^{-1}(\phi) \\ &= \begin{pmatrix} \varepsilon_{\parallel}\cos^2\phi + \varepsilon_{\perp}\sin^2\phi & (\varepsilon_{\parallel} - \varepsilon_{\perp})\cos\phi\sin\phi & 0 \\ (\varepsilon_{\parallel} - \varepsilon_{\perp})\cos\phi\sin\phi & \varepsilon_{\parallel}\sin^2\phi + \varepsilon_{\perp}\cos^2\phi & 0 \\ 0 & 0 & \varepsilon_{\perp} \end{pmatrix}, \end{aligned} \tag{1.4}$$

where $\boldsymbol{R}_z(\phi)$ and $\boldsymbol{R}_y(\theta)$ are the rotation matrix, and $\varepsilon_{\perp}$ and $\varepsilon_{\parallel}$ are the ordinary and extraordinary dielectric constant of the LCs. Eq. (1.4) can be simplified as

$$\boldsymbol{\varepsilon}(z) = \begin{pmatrix} \bar{\varepsilon} & 0 & 0 \\ 0 & \bar{\varepsilon} & 0 \\ 0 & 0 & \varepsilon_{\perp} \end{pmatrix} + \alpha\begin{pmatrix} \cos 2qz & \sin 2qz & 0 \\ \sin 2qz & -\cos 2qz & 0 \\ 0 & 0 & 0 \end{pmatrix}, \tag{1.5}$$

where $\bar{\varepsilon} = \frac{\varepsilon_{\parallel} + \varepsilon_{\perp}}{2}$ and $\alpha = \frac{\varepsilon_{\parallel} - \varepsilon_{\perp}}{2}$. Figure 1.5 shows the dielectric tensor distribution along the helical axis of a left-handed ChLC with a helical pitch of 400 nm. From Eq. (1.5) and Fig. 1.5, it is revealed that ChLC has a sinusoidal dielectric tensor distribution along the helical axis with a periodicity of a half-pitch owing to the head-tail symmetry of the LC molecules.

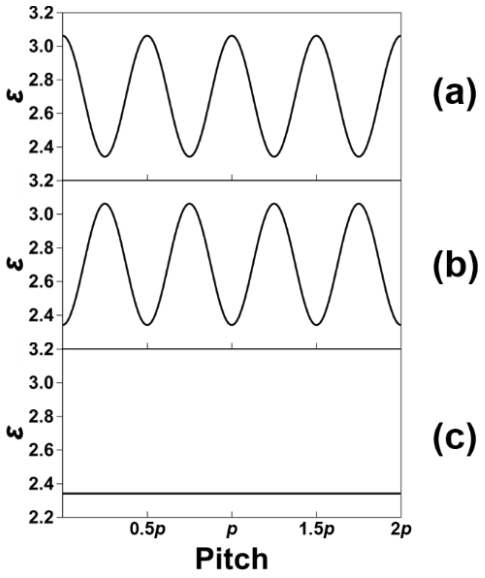


Figure 1.5 Dielectric tensor distribution of ChLCs along the helical axis. (a) ε_{xx}, (b) ε_{yy}, and (c) ε_{zz} components.

Because of the periodic dielectric tensor distribution, ChLCs shows a Bragg reflection over a certain wavelength range given by $n_o p – n_e p$, where n_o and n_e are the ordinary and extraordinary refractive indices of LC molecules. Figure 1.6 shows the typical Bragg reflection from a left-handed ChLC for normal incidence upon LCP and RCP light, which is calculated using Berreman's 4 × 4 matrix method (see Appendix A for the calculation method) [43]. Because of its helical structure, the Bragg reflection shows CP selectivity, where only a CP light with the same handedness as the helix is reflected, and opposite CP light is completely transmitted through the medium. The bandwidth of the Bragg reflection is determined by the birefringence of the LC material and helical pitch, given by $\Delta\lambda = \Delta n p$, where Δn is the birefringence of the LC ($\Delta n = n_e - n_o$). This Bragg reflection can also be obtained by solving Maxwell's equation for light propagating in a direction along the helical axis [44]. Because ChLCs show the sinusoidal dielectric tensor distribution, they possess only a single Fourier component, and thus all higher-order reflections are suppressed upon normal incidence [31]. This fact will be further described in Chapter 2.

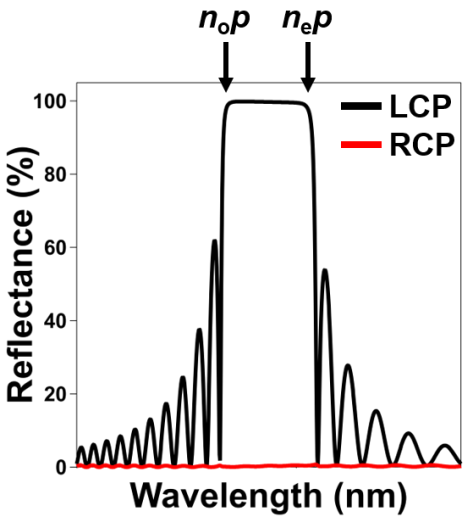


Figure 1.6 A typical Bragg reflection spectrum of a ChLC. The Bragg reflection only appears when illuminated by a CP light with same handedness as the helix. The reflection wavelength is determined by the birefringence of the LC molecules and the helical pitch, which is given by $n_op - n_ep$.

By appropriately controlling the structure of the ChLCs, they can be used for various tunable optical applications. For example, the wavelength and CP selectivity of the Bragg reflection can be directly used for band-pass color filters and circular-polarizing beam splitters. The periodic modulation in the refractive index also provides a cavity responsible for lasing oscillation [45, 46]. The lasers show a narrow bandwidth with a low threshold energy, and the capability to tune the emission wavelength owing to the external stimuli-responsivity of the LCs. In addition, more recently, various HOEs have been demonstrated based on the BB effect [32–41], which will be described in detail in Section 1.3. A helical structure can be tuned using external stimuli such as heat [47], electric field [46, 48], light [49], and mechanical stress [50], resulting in various tunable optical elements.

1.2.2 Blue phases

There is an exotic LC phase called BPs that appear in a narrow temperature range between the cholesteric and isotropic phases. BPs were discovered by Reinitzer in 1888 [42], but owing to their narrow temperature range, they were considered to be thermodynamically unstable and were not originally investigated. Since it was revealed that BPs are in a thermodynamically stable state and one of the liquid crystal phases [51], various investigations into their structure and electro-optical properties have been conducted. Whereas ChLCs are created through a

uniaxial twisting of the LC director, BPs are formed through a biaxial twisting with the axes of the twists perpendicular to each other, as shown in Fig. 1.6 (a). They are assembled into a cylindrical block called a double-twist cylinder (DTC) (Fig. 1.6 (b)). Depending on the packing symmetry of the DTCs in 3D space, BPs are categorized into two-types of cubic structures: BP I (Fig. 1.7 (c)) and BP II (Fig. 1.7 (d)) with a periodicity (hereafter, called a lattice constant (*a*)) of a few 100 nm. BP I has a body-centered cubic structure with O_8 symmetry, whereas BP II shows a simple cubic structure with O_2 symmetry. Although the molecular orientation of the LCs in a DTC have yet observed, the 3D lattice structures of cubic BPs have been directly confirmed through observations using a transmission electron microscope [52] and laser confocal microscope [53]. When the DTCs are filled in a 3D space to form cubic BPs, empty space inevitably occurs because DTCs cannot fully fill in a 3D space. In an empty space, defect lines in which LC molecules are randomly oriented are formed, as shown in the red lines in Figs. 1.7 (c) and (d). The BPs are thermodynamically stable and have a frustrated structure by the coexistence of the DTC and defect lines.

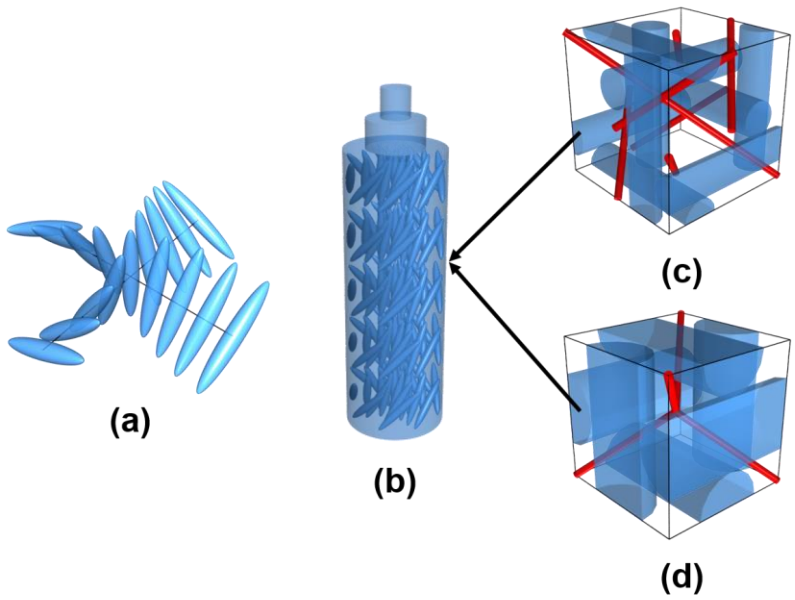


Figure 1.7 A schematic of the BPs structure. (a) Two-axis twist of LC director with its axes perpendicular to each other. (b) Structure of double-twist cylinder. (c) Body-centered cubic BP I with its defect lines. (d) Simple cubic BP II with its defect lines.

Although the BPs are attractive materials for various applications, their narrow temperature range limits their use in practical applications. Various approaches have been proposed to stabilize BPs within a wide temperature range. Polymer-stabilization is the most powerful

method, which was proposed by Kikuchi et al. in 2002 [54]. A small amount of acrylate-based monomers added in BPs are locally polymerized around the defect lines, resulting in a BP I with a temperature range over 60°C. Recently, Jo et al. demonstrated a polymer-stabilized BP II using a BP II doped with bent-core molecules [55]. Another approach is to design the chemical structure of the LCs proposed by Coles et al. in 2005 [56]. The use of LC molecules with dimers formed by a flexoelectric-optic effect results in BPs with a temperature range over 40°C. Various methods have also been proposed to stabilize the BPs by adding additives such as T-shape molecules [57], bent-core molecules [58], and nanoparticles [59]. They stabilize the defect lines, expanding the temperature range of the BPs. In addition, our group has proposed a method to confine the BP in a micro-sized polymer network, enabling a temperature range over 10°C during the cooling process [60].

BPs are attractive materials for various applications owing to their self-organized periodic 3D cubic structure. Because the lattice constant (a) of a 3D cubic structure is usually several hundred nanometers, BPs also show a Bragg reflection band in the visible light region. The dielectric tensor distribution of BPs can be obtained from the Landau-de Gennes theory [61], which describes the LC orientation by a symmetric and transless second rank tensor $\mathbf{Q}_{\alpha\beta}$. The free energy for a chiral LC under a zero electric field can be expressed by the following:

$$f = c\,\mathrm{Tr}\mathbf{Q}^2 - \sqrt{6}\,b\,\mathrm{Tr}\mathbf{Q}^3 + a\left(\mathrm{Tr}\mathbf{Q}^2\right)^2 + \frac{1}{4}K_1\left[\left(\nabla\cdot\mathbf{Q}\right)_{\alpha\beta} + 2\,q_0\,\mathbf{Q}_{\alpha\beta}\right]^2 + \frac{1}{4}K_0\left[\left(\nabla\cdot\mathbf{Q}\right)_{\alpha}\right]^2, \quad (1.6)$$

where the first three terms with the parameters of a, b (both positive constant), and c (variable depending on the temperature) indicate the local free energy through Landau expansion, and the last two terms indicate the free energy on spatially variable order of the LCs. The K_0 and K_1 are the spray and twist elastic constants of the LC material, and q_0 is $2\pi/p$ indicating the chiral strength and handedness. Equation (1.6) can be simplified by using rescaled order parameters as follows:

$$f(\chi)/f_0 = c\,\mathrm{Tr}\,\chi^2 - \sqrt{6}\mathrm{Tr}\,\chi^3 + \left(\mathrm{Tr}\,\chi^2\right)^2 + \kappa^2\left\{\left[\left(\nabla\cdot\chi\right)_{\alpha\beta} + 2\,q_0\chi_{\alpha\beta}\right]^2 + \eta\left[\left(\nabla\cdot\chi\right)_{\alpha}\right]^2\right\}, \quad (1.7)$$

where $f_0 \equiv b^4/a^3$ is the unit of the free energy density. In Eq. (1.7), $\chi_{\alpha\beta} \equiv (a/b)Q_{\alpha\beta}$, $\kappa \equiv \sqrt{aK_1q_0^2/b^2}$, and $\eta = K_0/K_1$ are the rescaled order parameter, chirality, and anisotropy of the elasticity, respectively, which are related to the physical parameters of the LC material. In addition, $\tau \equiv ac/b^2$ is the rescaled temperature. Here, the total free energy in a BP can be expressed by the following:

$$\begin{aligned} \boldsymbol{F} &= \int d\,\boldsymbol{r}\; f(\chi)/f_0 \\ &= \int d\,\boldsymbol{r}\left[c\,\mathrm{Tr}\,\chi^2 - \sqrt{6}\,\mathrm{Tr}\,\chi^3 + \left(\mathrm{Tr}\,\chi^2\right)^2 + \kappa^2\left\{\left[(\nabla\cdot\chi)_{\alpha\beta} + 2q_0\chi_{\alpha\beta}\right]^2 + \eta\left[(\nabla\cdot\chi)_{\alpha}\right]^2\right\}\right]. \end{aligned} \tag{1.8}$$

The dielectric tensor distribution of BP I was obtained from the relationship

$$\varepsilon_{ij} = \varepsilon_{iso}\delta_{ij} + \varepsilon_a\chi_{ij}, \tag{1.9}$$

where $\varepsilon_{iso} = \dfrac{2n_o^2 + n_e^2}{3}$, $\varepsilon_a = \dfrac{n_e^2 - n_o^2}{\chi_o}$, χ_0 is the degree of orientation order in the bulk . Figure 1.8 shows the averaged dielectric tensor distribution of a BP I when illuminated by a light along the [110] crystal axis. The order parameter tensor distribution of a right-helix BP $I_{(110)}$ was obtained by minimizing the free-energy in Eq. (1.8) on a 32 × 32 × 32 grid (The order parameter distribution was provided from Prof. Jun-ichi Fukuda at Kyushu University). The rescaled material parameters were set as τ = -0.3, κ = 0.7, and η = 1. It is revealed that BPs also have a sinusoidal dielectric tensor distribution along the propagation direction of light. The periodicity of the dielectric tensor distribution is half the periodicity of the (110) crystal planes. By contrast, unlike the ChLC, the ε_{zz} component is also periodically modulated owing to the 3D helical cubic structure of the BPs.

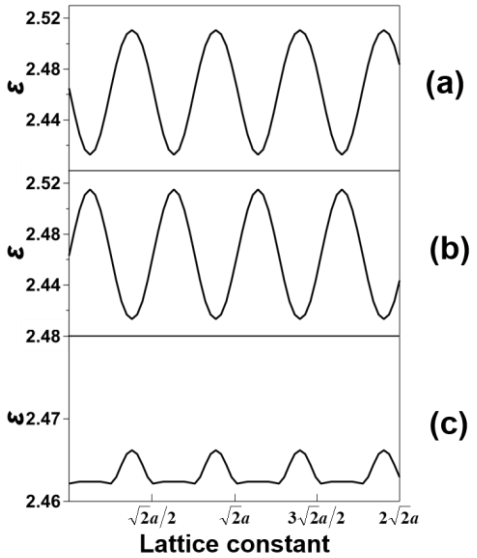


Figure 1.8 Averaged dielectric tensor distribution of BP I along the [110] crystal axis. (a) ε_{xx}, (b) ε_{yy}, and (c) ε_{zz} components.

Figure 1.9 shows the simulated Bragg reflection of a BP I with a (110) crystal plane using Berreman's 4 × 4 matrix method [43] using the dielectric tensor distribution shown in Fig. 1.8. In general, the central wavelength of the Bragg reflection (λ_{center}) can be obtained as follows:

$$\lambda_{\text{center}} = \frac{2na}{\sqrt{h^2+k^2+l^2}}, \tag{1.10}$$

where n is the average refractive index of the BPs and (hkl) indicates Miller indices representing the crystal plane orientation. According to the extinction rule for crystals, BP I shows a Bragg reflection when the sum of the Miller indices (h+k+l) is even, and BP II shows the Bragg reflection for all values of Miller indices. BPs generally show a narrow bandwidth compared to that of ChLCs [62]. BPs also have a sinusoidal modulation in the dielectric tensor distribution; only a CP light with the same handedness as a helix are reflected, whereas an opposite CP light is totally transmitted. In addition, a 3D cubic structure is expected to realize omnidirectional CP-selective device that cannot be achieved in ChLCs, which will be described in detail in Chapter 3.

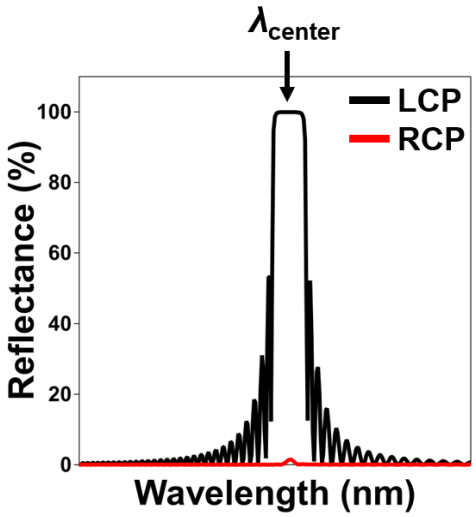


Figure 1.9 Typical Bragg reflection of BP I with (110) crystal plane.

A 3D laser emission has been proposed using BP II [63], while a widely wavelength-tunable laser spanning approximately 200 nm has been achieved using a BP I doped by a bent-core molecule [64]. In addition, because BPs show a fast response time of 100 μs under the application of an electric field [54], they are regarded as a promising material for next-generation displays. Samsung Electronics has developed a BP-based LCD panel by inducing birefringence in the BP through the Kerr effect. In addition, our group has predicted that BPs can be used for the fabrication of flat optical elements such as deflectors, lenses, and holograms based on the BB effect [33].

1.3 Volume HOEs based on chiral liquid crystals

LCs are an attractive material for the realization of volume holograms owing to their self-organized structures and external-stimuli responsivity. Various LC phases such as NLC, ChLCs, and BPs can be used for the fabrication of volume HOEs by appropriately controlling the orientation of LC molecules on a substrate. Table 1.1 shows the description of the basic operation principles for HOEs realized by NLCs, ChLCs, and BPs. The principle of volume HOEs using NLC is based on the Pancharatnam-Berry (PB) or geometric phase [65, 66]. When CP light is transmitted through an anisotropic medium with a half-wave retardation condition, the polarization is converted into the opposite CP light with an additional optical phase proportional to twice the orientation of the LC director. Thus, various HOEs can be realized by spatially controlling the optical axis of the LC molecules on a substrate [67, 68]. Whereas the NLCs enable transmissive HOEs, the ChLCs and BPs allow the realization of reflective volume HOEs based on the BB effect. In this section, the BB effect in which a Bragg reflected optical phase can be modulated from 0 – 2π radians by controlling the structural phase (orientation of LC molecules for ChLC, and orientation of lattice structure for BPs) from 0 – π radians on a substrate is described [33].

Table 1. 1 Comparison of transmissive and reflective HOEs using various LC phases

	NLCs	ChLCs and BPs (with left helix)
Operation mode	Transmissive	Reflective
Operation principle	Pancharatnam-Berry	Bragg-Berry phase
Operating wavelength	Wavelength with Half-wave retardation	Within Bragg reflection band
Diffraction properties (for LCP illumination)	+1 order diffraction	+1 or -1 order Reflected and diffracted
Diffraction properties (for RCP illumination)	-1 order diffraction	Transmitted and no diffracted

Figure 1.10 (a) shows the schematics of a left-handed ChLC with various orientations of LC molecules on a substrate. The angle of φ is the helix phase defined as an angle between the x-axis and long-axis of LC molecules on a substrate. Figures 1.9 (b) and (c) show the simulated Bragg reflectance and reflected/transmitted optical phase from the ChLC upon LCP and RCP illumination. The simulation was conducted using Berreman's 4 × 4 matrix method [43] with the physical values of n_o = 1.53, n_e = 1.75, p = 350 nm, and d = 7000 nm, where d is the total thickness of the device (containing 20 helices). The helix phase was varied from 0 to π radians with a step of 1°. Light with a wavelength of 600 nm, which is a wavelength falling within the

Bragg reflection spectrum of the modeled ChLC, was incident along the helical axis (*z*-axis in Fig. 1.10 (a)). For LCP illumination, one can see that the variation of the helix phase causes the reflected optical phase to be linearly modulated from 0 to 2π radian, while maintaining the reflectance at 100% (Fig. 1.10 (b)). By contrast, for RCP illumination, the light is totally transmitted without a change in the optical phase (Fig. 1.10 (c)). Thus, various CP-selective HOEs can be realized by spatially controlling the helix phase of LC molecules on a substrate. This result can also be obtained from an exact solution by solving the Maxwell equation based on coupled-mode theory [40].

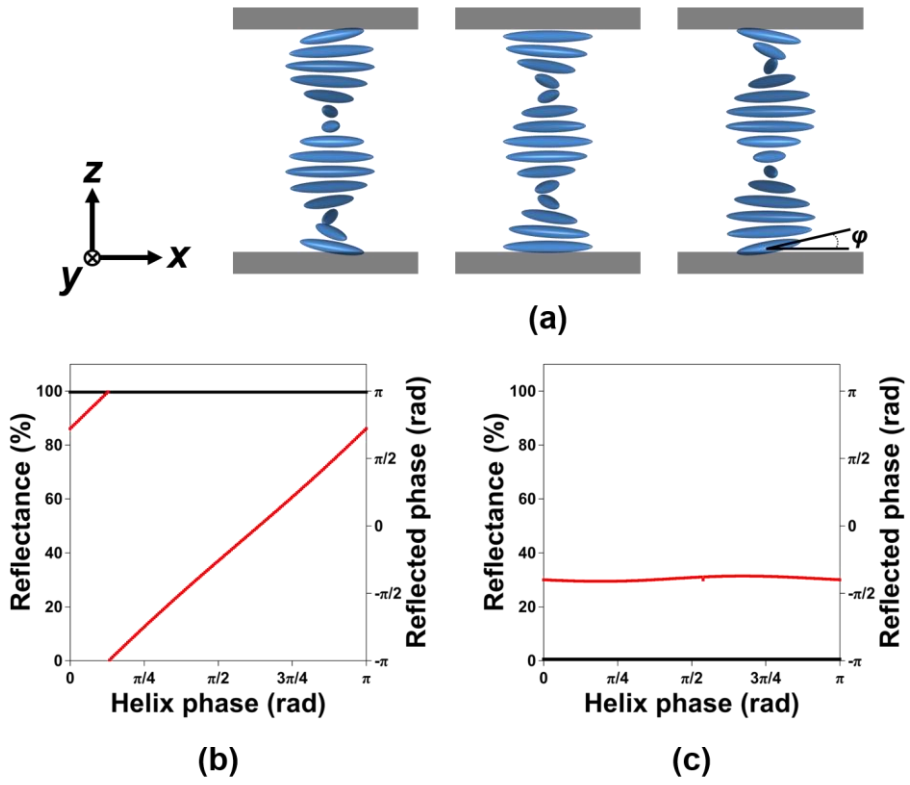


Figure 1.10 BB effect from ChLC. (a) A schematic of a ChLC with various helix phase. (b) Simulated Bragg reflection intensity and reflected optical phase upon LCP light incidence with wavelength of 600 nm. (c) Simulated Bragg reflectance and transmitted optical phase upon RCP light incidence with wavelength of 600 nm.

The BB HOEs using ChLCs have a number of advantages compared to conventional HOEs. The self-organized helical structure does not require complex laser setups to record the light information. Because the reflection intensity is maintained at 100%, ChLC-based HOEs enable the control of light with high conversion efficiencies. The intrinsic chirality enables the realization of CP-selective HOEs in which the optical phase is modulated in only reflected light,

while transmitted light has no change. Moreover, the BB effect is always valid for the wavelength falling within Bragg reflection spectrum, resulting in devices capable of operating within the entire visible light region [69]. The external stimuli-responsivity of LCs enables devices capable of tunable optical effects to be developed by controlling either the helical pitch [32, 49] or refractive index [48]. As a practical use of ChLC-based HOEs, there is the possibility of fabricating low-cost and large-area devices using a film-type ChLC coated through spin-coating [34] or a roll-to-roll process [70] on a substrate.

The BB effect is also observed in BPs in the same manner as with the ChLCs. Here, the optical effect of a BP I with a (110) crystal plane oriented parallel to the substrate, as shown in Fig. 1.11 (a), is investigated. The analysis was conducted using the 4 × 4 matrix method with physical parameters of $n_o = 1.5$, $n_e = 1.7$, $a = 225$ nm, and $d = 7550$ nm that contains 20 lattices along the direction of the light propagation. The averaged dielectric tensor distribution of BP I with the (110) crystal plane is shown in Fig. 1.8, which is obtained based on the Landau-de Gennes theory [61]. A light with wavelength of 580 nm was assumed to propagate along the [110] crystal axis. For the investigation of the BB effect, the azimuthal angle of the lattice structure, which is the angle between the *x*-axis and the [001] crystal axis, is varied from 0 to π radians on a substrate (Fig. 1.11 (b)). As shown in Figs. 1.11 (c) and (d), the reflected optical phase is modulated from 0 to 2π radians when illuminated by RCP light, whereas the opposite CP light is transmitted without an optical phase change in a same manner as in the ChLCs. Although the theoretical prediction of the BB effect of BPs enables the fabrication of volume HOEs, the realization of HOEs using BPs is extremely rare, because it remains a challenge to spatially control the crystal plane and azimuthal orientation on a substrate. BP-based HOEs are described in Chapter 3 based on a facile method to simultaneously control the crystal plane and the azimuthal orientation.

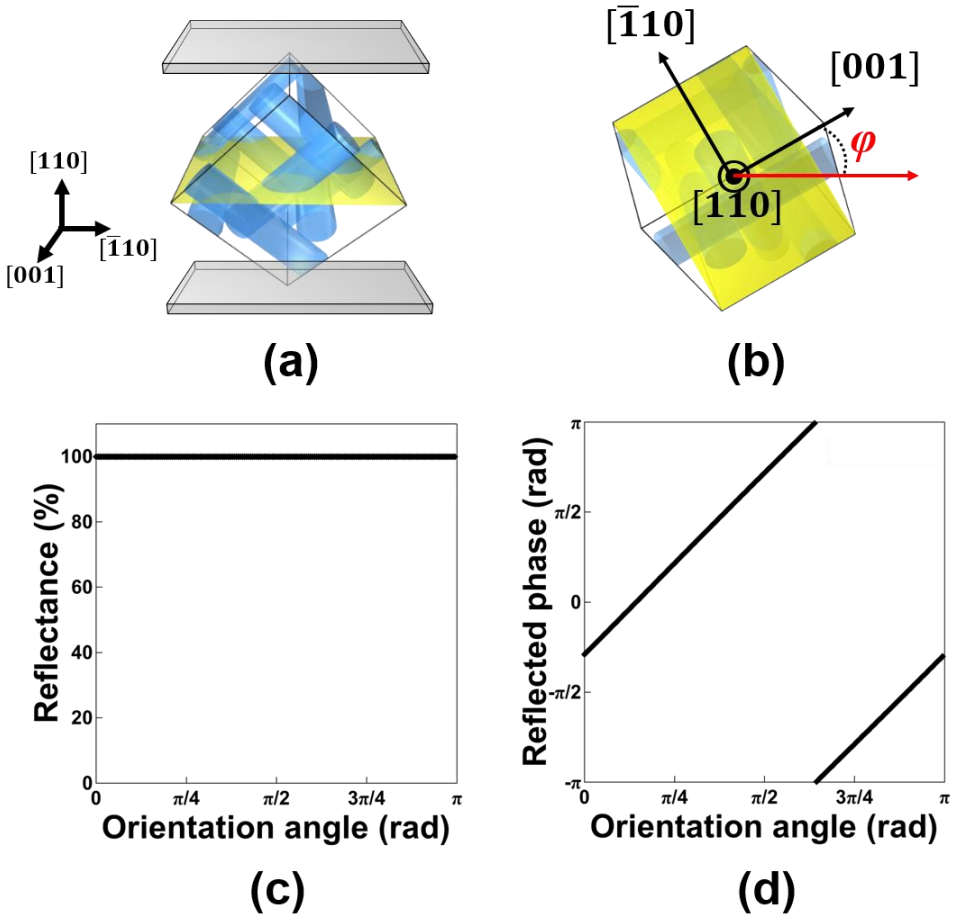


Figure 1.11 A schematic of BP I with its crystal axes. (a) BP I with the (110) crystal plane sandwiched in a cell. The [001] crystal axis is aligned in a direction parallel to the orientational easy axis on the substrate. (b) Top view of the (110) crystal plane of BP I, where φ is the azimuthal orientation angle defined at an angle between the [001] crystal axis and the *x*-axis. (c) Reflectance depending on the azimuthal orientation angle of the BP lattcies. (d) Reflected optical phase with respect to the azimuthal orientation angle of the BP lattices.

1.4 Photoalignment technology

To obtain the desired optical effects from chiral LCs, it is important to appropriately control the orientation of the LC director on the substrate. Various technologies have been used to control the local orientation of the LC director including micro- and nano-rubbing [71], photoalignment [72, 73], and laser-lithography [74]. Among them, a photoalignment is a powerful technology because it requires only a linear polarized (LP) light to induce the alignment without direct mechanical contact on the alignment layer, resulting in defect-free alignment of the LC molecules. Since a photoalignment was first demonstrated in 1988 by

Ichimura [75], it has been widely used in the fields of displays, organic electronics, and compact optical elements.

There are various photo-responsive compounds available for a photoalignment such as azobenzen-based molecules [75] and polysiloxane- and/or cinnamate-based materials [76]. The photoalignment material used in this dissertation are the azobenzene-based molecules, which are photo-isomerized into two forms: a *trans*-state in which the molecules have a rod-like shape (thermodynamically stable state), and a *cis*-state with a bent shape. Figure 1.12 shows the basic principle of the photoalignment technology. When the azo-molecules coated on a substrate are illuminated by LP light with a wavelength of shorter than 480 nm, they are photo-isomerized into a *trans*-state with their orientation perpendicular to the incident LP light to minimize the absorption energy. The oriented azo-molecules impose a surface anchoring to the LC molecules to be aligned parallel to the azo-molecules (Fig. 1.12 (b)). Compared to a conventional alignment technology such as the rubbing process, the photoalignment enables the orientation of LC molecules to be spatially controlled with high-resolution on a substrate (Fig. 1.12 (c)). In addition, the method allows the reversible writing and erasing of the alignment.

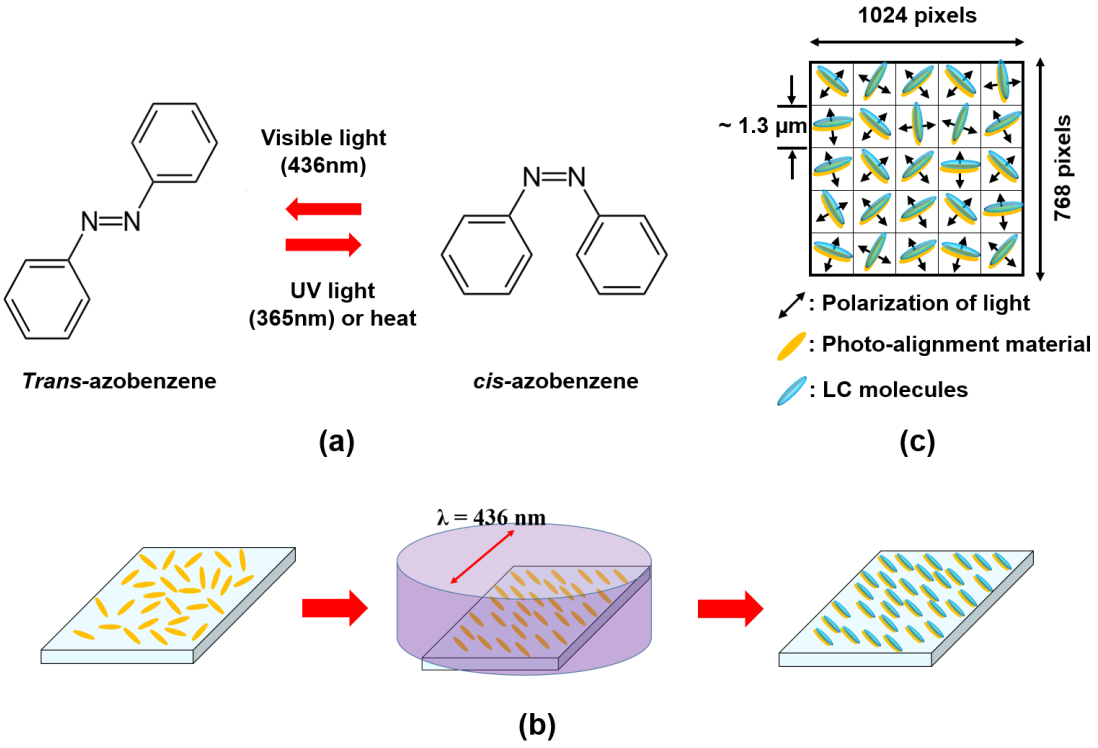


Figure 1.12 A schematic of photoalignment technology. (a) Photo-isomerization of a azobenzene-based molecules. *Trans*- and *cis*-isomerization are induced by illuminating a light with energy corresponding to π–π* transition (which usually falls within the UV region) and n-π* transition (in the visible region), respectively. (b) Photoalignment process used to control

the LC orientation. The LC molecules are aligned parallel to the alignment molecules. (c) A example of the spatial control of the LC molecules on a substrate.

The photoalignment process achieved in this dissertation has been performed using either a maskless projection system [77] or a laser interference setup called a polarization holography [34, 78]. Figure 1.13 shows a schematic of the home-made maskless projection system consisting of a LC display (LCD) projector, a focusing lens (f = 250 mm), a short-pass filter (475 nm), a non-polarizing beam-splitter, a rotatable half-wave plate, and × 10 and × 40 objectives (UPlanFL for the × 10 and LCPlanFI for the × 40, both from Olympus). The light source of the LCD projector is a high-pressure mercury lamp that emits LP light over an area manipulated through an electronic mask. The polarization angle of the LP light is modulated by placing the HWP in the optical path and rotating it. The projection pattern is monitored using a CMOS camera. For the CGHs demonstrated in Chapters 2 and 3, the angle of LP light was controlled at increments of 10°. The patterning process is composed of a pixel resolution of 1024 × 768 with a nominal pixel size of 1.3 × 1.3 μm^2 for a × 10 objective and 0.33 × 0.33 μm^2 for a × 40 objective, giving a patterned area of 1.3 × 1.0 mm^2 and 0.33 × 0.25 mm^2, respectively. The light dosage for the patterning process are 0.4 μJ/pixel and 0.1 μJ/pixel for the × 10 and × 40 objectives, respectively. Another photo-patterning process to realize a high resolution alignment of the LC molecules using a laser interference pattern will be described in Chapter 4.

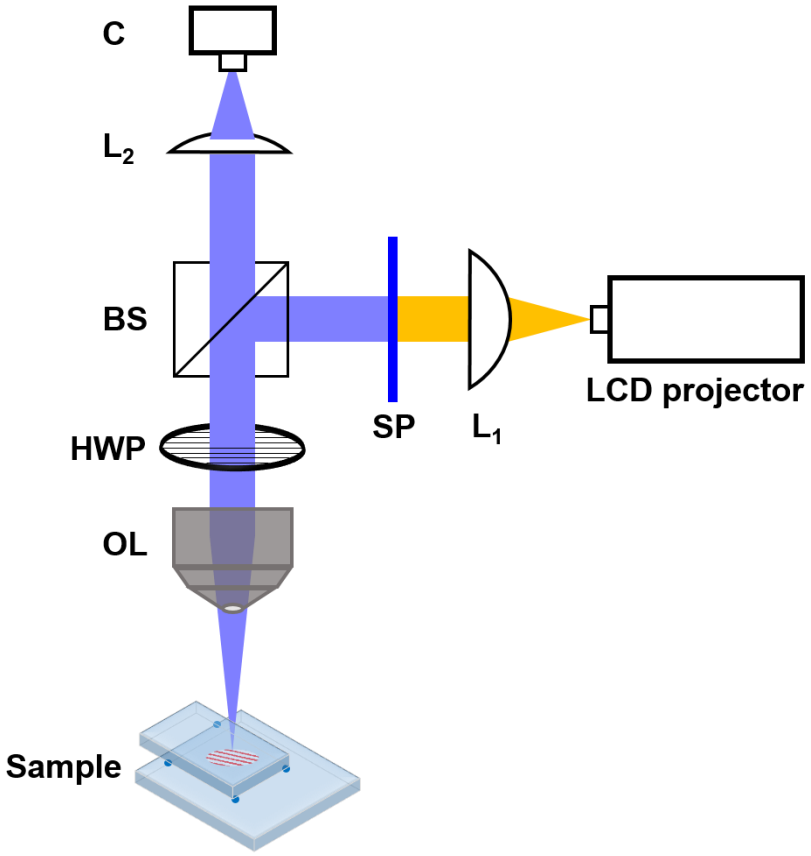


Figure 1.13 A schematic of the maskless projection system. LCD: LC display; L_1: focusing lens (f = 250 mm); SP: short-pass filter (475 nm); BS; non-polarizing beam-splitter; HWP: rotatable half-wave plate; OL: × 10 or × 40 objectives; L_2: focusing lens (f = 150 mm); C: CMOS camera.

1.5 Motivation and contents of this dissertation

Despite the development of nanofabrication and nano-optics, there are advanced optical functionalities required by practical applications that cannot be implemented using metasurfaces and conventional HOEs. For example, see-through optics are required in smart glasses, which are regarded as next-generation displays. However, reflective metasurfaces cannot be transparent owing to the absorption of light by the nanostructure or the use of a metallic reflector to ensure a high light-conversion efficiency [5]. In addition, conventional HOEs have a Bragg reflection in the visible light region, limiting their see-through capability under ambient light. This dissertation is devoted to investigating volume HOEs with advanced functionalities such as complete transparency under ambient light and omdirectional CP selectivity using the two types of chiral LCs.

The contents of this dissertation are as follows. In Chapters 2 and 3, phase-only reflective volume holograms are realized by spatially modulating the structural phase of LC molecules

on a substrate. In Chapter 2, the angular dependent Bragg reflection of a ChLC is first theoretically demonstrated to show all higher-order reflections to be suppressed for all accessible angles of incidence. The ChLC is applied to the fabrication of a transparent CGH and waveguide holography. In Chapter 3, a simple method to independently control two crystal axes of BP $I_{(110)}$ through a field-reorientation process is described. The technique is applied to the fabrication of a CP-selective CGH for all angles of incidence accessible from air. In addition, the omnidirectional CP selectivity is theoretically described by investigating the photonic band structure of a BP $I_{(110)}$, and is experimentally supported by measuring the angular dependent Bragg reflection spectrum. Moreover, a short-pitch and large-angle deflector is presented using a simple cubic BP II. A short-pitch periodic modulation of the LC director is introduced through a polarization holography method. Possible orientation behaviors of the device are presented through an analysis of the Kossel patterns and transmission spectra. The electro-optic characteristics of the device are investigated to realize a tunable and switchable light deflector. In Chapter 4, a micro-PC band-edge laser with a capability to control the emission direction is presented based on a ChLC with modulated layer structure. The tunable emission-direction is clarified by investigating the photonic band structures of the ChLC, and experimentally demonstrated by realizing a PC laser with tunable emission angle range of approximately 4°. In Chapter 5, the results from each chapter are summarized along with future areas of studies.

Note: The appendices present derivations of equations and helpful techniques for optical analyses and experiments.

Chapter 2 Transparent hologram and waveguide hologram with patterned cholesteric liquid crystals

2.1 Introduction

The demand of see-through optical elements has recently increased in various applications such as transparent displays, smart-glasses, and head-up displays. The property of being 'see-through' is necessary to superimpose the real space and virtual information on the user's field of view. Conventional volume HOEs are candidates for realizing the ability to see through optical elements owing to the narrow bandwidth of the Bragg reflection. Light with the wavelength outside the Bragg reflection band is transmitted through the device, resulting in various see-through devices such as the out-couplers of waveguide-type displays [24, 25]. However, they still have Bragg reflection band in the visible light region, making the device to show a hue.

Metasurfaces have also attracted interest for seeing through optical devices because they enable the integration of multiple functionalities in an ultra-compact single device. Reflective metasurfaces have been used for an out-coupler of a computer-generated waveguide holography; however, their output light efficiency is extremely low (>1%) due to the optical loss by the materials [79]. Metasurfaces with high efficiencies as high as 80% in the visible light region have been achieved [5], but it cannot be transparent owing to the use of a metallic reflector, and hence they have limited practical applications where the capability to see through the elements is required.

In this chapter, a completely transparent HOE in the visible light region under ambient lighting conditions is proposed using a ChLC. First, the angular-dependent Bragg reflection spectrum of a ChLC is theoretically investigated to design the transparent device. The results show that all higher-order reflections are forbidden for normal incidence, and are weakly observed (~10%) for oblique incident angles accessible from air. Thus, a transparent ChLC-based HOE can be made by setting the first-order reflection band within the IR region. In addition, reconstruction of the encoded holograms in the visible light region is also demonstrated by illuminating light at incident angles greater than the angle simply accessible by refraction from air. Two types of designs are used to increase the incident angle: attaching an index-matching prism on the device and integrating the device with a waveguide layer. The

devices proposed in this chapter will be useful for various applications where the capability to see through the device is necessary such as transparent displays and augmented reality (AR).

2.2 Theoretical background

To fabricate a completely transparent device, the device should be designed such that there is no absorption nor reflection. Because a typical ChLC material does not absorb light in the visible light region, a transparent device can be realized by making all Bragg reflection bands to be outside the visible light region for ambient light. In this section, Bragg reflection spectra of a ChLC with a first-order Bragg reflection band in the IR region is theoretically investigated. The result shows that all higher-order reflections do not appear suppressed under ambient lighting conditions, making it possible to fabricate transparent devices.

The calculations were performed using Berreman's 4 × 4 matrix method [43] with physical parameters of which are summarized in the upper row of Table 2.1. Figure 2.1 (a) shows a schematic of a modeled ChLC with the helical axis taken along the *z*-axis. The left-handed ChLC was considered to be sandwiched between two glass substrate (n_g = 1.53) with a gap of 9 μm. A helical pitch of 700 nm was set such that the central wavelength of the Bragg reflection band for normal incidence appears at a wavelength of ~ 1150 nm. The dielectric tensor distribution ($\boldsymbol{\varepsilon}$) of the ChLC along the helical axis with a helix phase of φ is expressed as follows:

$$\boldsymbol{\varepsilon}(z) = \begin{pmatrix} \bar{\varepsilon} & 0 \\ 0 & \bar{\varepsilon} \end{pmatrix} + \alpha \begin{pmatrix} \cos 2(qz+\varphi) & \sin 2(qz+\varphi) \\ \sin 2(qz+\varphi) & -\cos 2(qz+\varphi) \end{pmatrix}. \tag{2.1}$$

In the simulation, the LC director was oriented along the *x*-axis at $z = 0$, i.e., the helix phase is zero. For comparison, the Bragg reflection band of a quarter-wave stack (QWS) is also simulated through same method. The physical values of the QWS are listed in the bottom row of Table 2.1, and Fig. 2.1 (b) shows a schematic of the modeled QWS. It has a thickness of 9 μm and is assumed to exist between two substrates with a refractive index of 1.53. The QWS has a square dielectric tensor distribution along the device normal (*z*-axis), which is expressed as follows:

$$\varepsilon(z) = \begin{cases} n_1^2, & mp \le z \le mp + d_1 \\ n_2^2, & mp + d_1 \le z \le (m+1)p \end{cases}, \tag{2.2}$$

where n_1 and n_2 are the refractive indices of two layers, d_1 and d_2 are the corresponding thicknesses, p is the sum of the thicknesses of different two layers ($d_1 + d_2$), and m is an integer. The simulations were carried out using LCP and RCP illumination for the ChLC, and LP

illumination for the QWS. The incident angles are defined as the angle between the direction of light propagation in the surrounding substrate with respect to the device normal, and are varied in the *z*–*x* plane.

Table 2. 1 Numerical parameters of the ChLC and QWS used in the simulations. Here, n_1 and n_2 are the refractive indices of two dielectric layers, and d_1 and d_2 are the corresponding thicknesses.

	n_e	n_o	p		Device thickness
ChLC	1.75	1.53	700 nm		9 μm
	n_1	n_2	d_1	d_2	Device thickness
Quarter-wave stack	2.35	1.53	122 nm	188 nm	9 μm

Figures 2.1 (c) and (d) show the simulation results of the Bragg reflection spectra of a ChLC upon LCP and RCP illumination, respectively. Note that when the devices are in free-space, the light cannot be incident at angles more than 41° (indicated by the white dashed line in Fig. 2.1) according to Snell's law. For both polarizations, it is clearly confirmed that there are no higher-order reflections in visible light region for normal incidence. This is because the sinusoidal dielectric tensor distribution of the ChLC possesses only a single Fourier component [31]. The second-order reflectance is slowly enhanced as the incident angle increases, but the maximum reflectance is extremely low (>10%) at the maximum incident angle (41°). On the other hand, the first-order reflection blue-shifts with a cosine dependence as the incident angle is increased, but still appears in the IR region for all angles of incidence. Thus, the ChLC can be completely transparent under ambient lighting conditions by setting the first-order Bragg reflection band within the IR region.

By contrast, as shown in Fig. 2.1 (e), the QWS shows odd-order reflections at normal incidence with a reflectance over 90%. In addition, a second-order reflection emerges at incident angles of 15° with a central wavelength of ~ 560 nm, and its reflectivity increases up to 90% at a 41° incidence. Thus, the QWS cannot be transparent in the visible light region due to the presence of higher-order reflections under ambient lighting conditions.

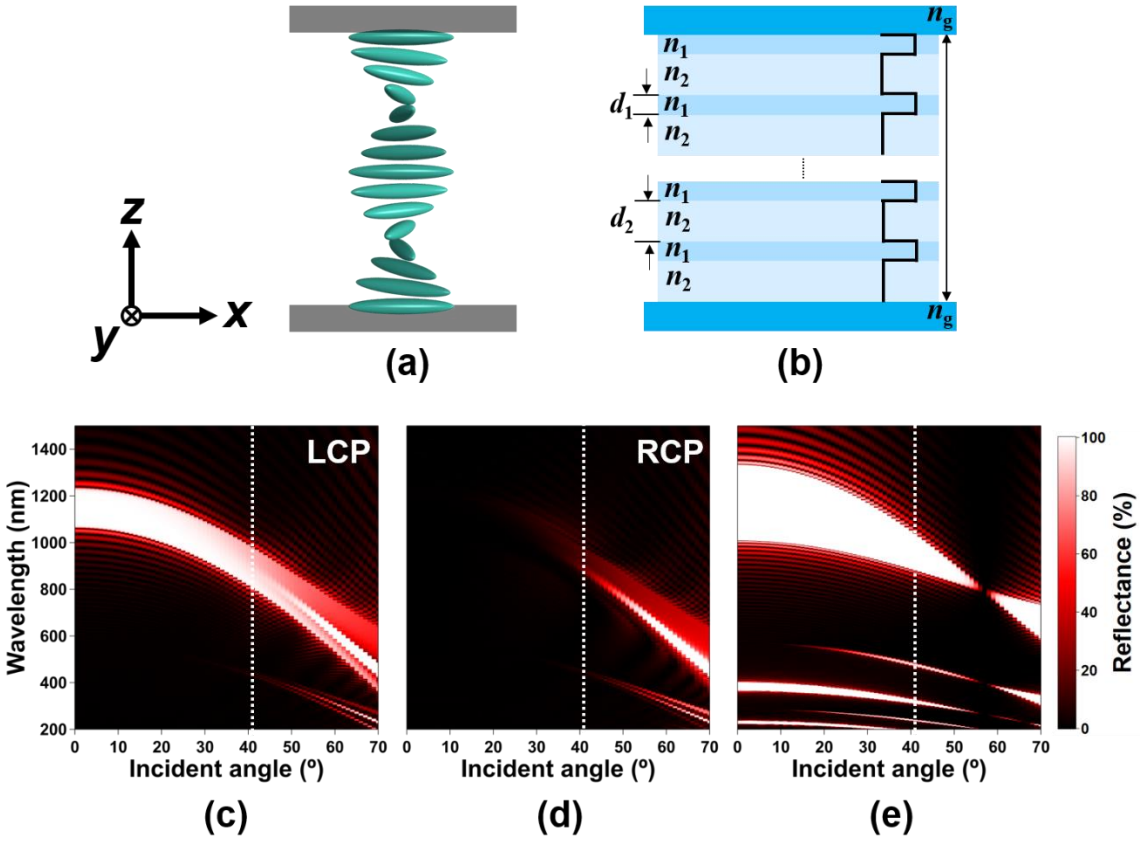


Figure 2.1 Simulated Bragg reflection from the ChLC and QWS. (a) Schematic of the ChLC with its helical axis along the *z*-axis. (b) Schematic of the QWS. (c, d) Simulated Bragg reflection spectrum of the ChLC for (c) LCP and (d) RCP illumination. (e) Simulated Bragg reflection spectrum of the QWS for LP illumination. The white dashed lines indicate the maximum incident angle in the device when devices are in free-space.

2.3 Transparent computer-generated hologram

In the previous section, it was shown that a ChLC can be transparent under ambient lighting conditions. In this section, the fabrication of a completely transparent CGH is described using the ChLC with the BB effect. The optical phase information is encoded onto the transparent ChLC by spatially varying the helix phase. The device is transparent despite the patterning of the helix phase distribution; however, the encoded holograms can be played back by visible light illuminated at large angles through appropriate optical designs.

2.3.1 Device fabrication and materials

The optical phase information for a hologram was computed using the Gerchberg-Saxton (G-S) algorithm (see Appendix B for details) [11, 12]. This algorithm is a powerful method

used to obtain the phase-only information of light propagating in a homogeneous medium through iterative Fourier and inverse Fourier transforms. Figure 2.2 (a) shows the source image (Osaka University mascot Dr. Wani) placed on a Fourier plane with a pixel resolution of 512 × 384. The optical phase information for the source image was computed through the G-S algorithm, and converted into the helical phase distribution (Fig. 2.2 (b)) through the relationship of $\varphi(x, y) = \pm 0.5\Phi(x, y)$, where $\varphi(x, y)$ and $\Phi(x, y)$ are the helix and optical phases. The algorithm was iterated 100 times to minimize the signal-to-noise ratio (SNR) of the hologram.

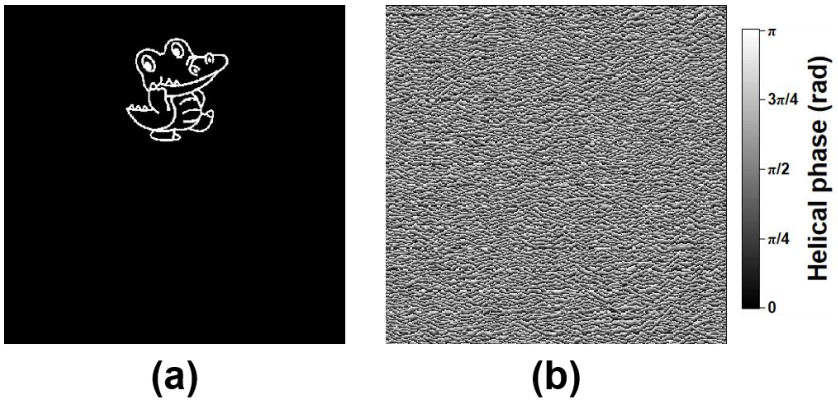


Figure 2.2 Hologram design. (a) Source image, i.e., Osaka University mascot Dr. Wani. (b) Helical phase distribution obtained through the G-S algorithm.

A sandwiched cell shown in Fig. 2.3 (a) was prepared by assembling two glass substrates covered by a photoalignment material (LIA-03, DIC). A cell gap of 9 μm is maintained by a ball spacer mixed in a photocurable adhesive (NOA68T, Norland). Two types of devices were fabricated: a uniformly aligned ChLC, and the hologram device upon which the optical phase distribution was imprinted (hereafter, the device of which the phase information is encoded is called a BB hologram). The patterning was conducted using a makeless photoalignment setup with a × 10 objective shown in Fig. 1.13, with phase steps of 10° (18 phase levels). The patterning was applied over a 6 × 8 array, giving a device with a total area of ~8 × 8 mm^2.

The transparent ChLC was prepared by blending a host nematic LC mixture (MLC-2140, Merck) and a left-handed chiral dopant (S-5011, HCCH) at a weight concentration of 98.8:1.2. The mixture was dissolved in chloroform for homogeneously blending, and heated at 80°C for 2 h to evaporate the solvent. The mixture was then injected into two devices at isotropic phase (100°C) and cooled to room temperature (25°C) at a rate of 0.3°C/min (Fig. 2.3 (c)).

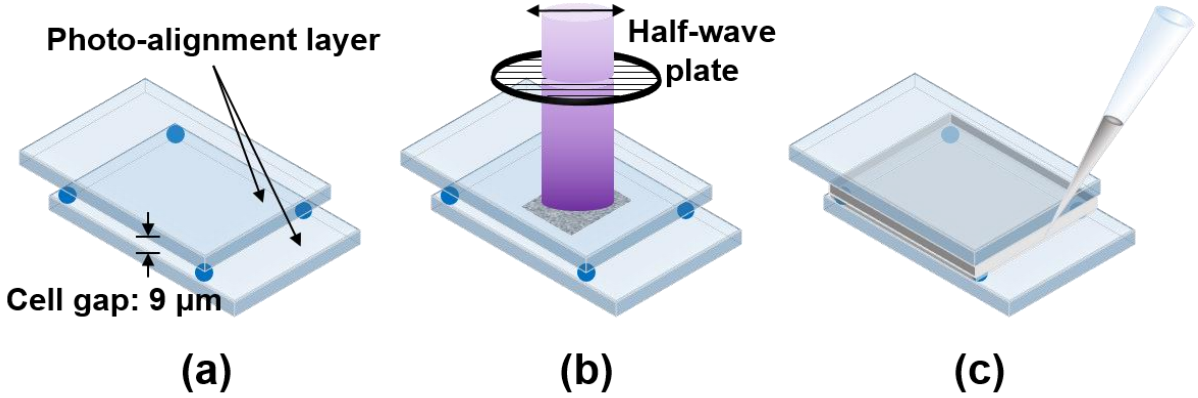


Figure 2.3 Sample fabrication process: (a) fabrication of the sandwiched cell, (b) photo-patterning process, and (c) material injection.

2.3.2 Spectral measurement

The reflection and transmission spectra were measured to demonstrate the transparency of the fabricated device. The measurement was performed using a home-made microscope equipped with a × 4 objective to illuminate IR light onto the device. The reflected light was collected by an optical fiber (diameter: ~1 mm) connected to a spectrometer (PMA-12, Hamamatsu), giving a diameter of the measurement spot of ~250 μm. The transmission spectrum was measured using a polarizing optical microscope (POM) (LV-100-POL, Nikon) to illuminate light on the sample. The transmitted light through the sample was collected through a × 10 objective and an optical fiber (diameter: ~ 1 mm) connected to another spectrometer (PMA-11, Hamamatsu). The photograph of the sample was taken using a commercially available camera (Canon, EOS Kiss X4).

As shown in Figure 2.4 (a), the ChLC reflects light with wavelengths falling between 1050 and 1200 nm. Therefore, no reflection band is observed in the visible light region due to the suppression of high-order reflections, as shown in Fig. 2.4 (b). The average transmittance of approximately 88% is obtained in the entire visible light region. The reduction in the transmittance is attributed to Fresnel reflection at the interface between the glass substrate and air. Thus, the transmittance can be further increased by employing an anti-reflection film on the device. Figure 2.4 (c) shows a photograph of the BB hologram, demonstrating the capability to see through the device under ambient lighting even though the patterning process has been performed.

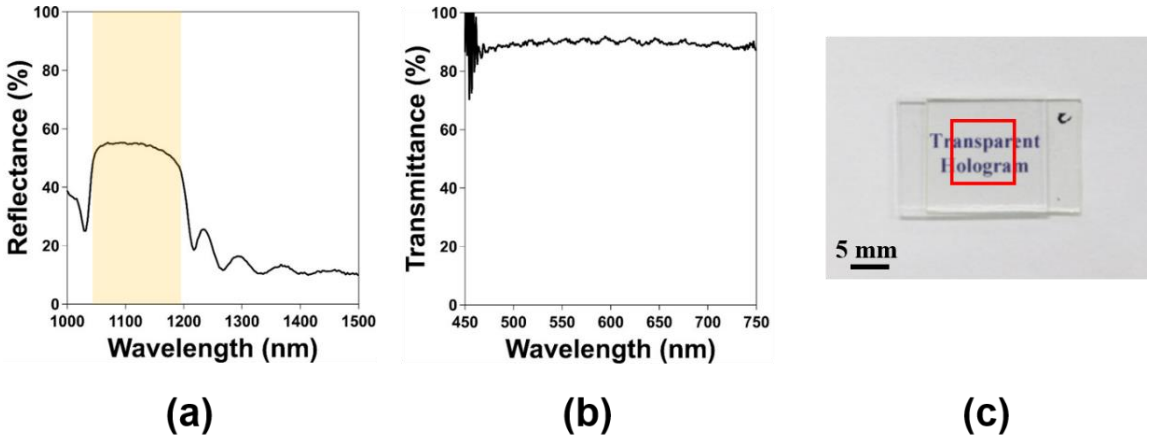


Figure 2.4 Optical characteristics of the fabricated hologram. (a) Bragg reflection spectrum of the uniformly aligned ChLC. (b) Transmission spectrum of the hologram. (c) A photograph of the hologram. The area inside the red square indicates where the helix phase distribution is imprinted.

2.3.3 Hologram playback

The encoded hologram was played back by illuminating a laser light on the device for normal incidence using a laser setup shown in Fig. 2.5 (a). A super-continuum laser (SuperK COMPACT, NKT Photonics) was illuminated on the sample after controlling its polarization through a polarizer and a Babinet-Soleil compensator. The wavelength of the light was selected by inserting a band-pass filter (central wavelength of 1100 nm with bandwidth of 10 nm) in the optical path. The reflected light spot from the BB hologram was focused on an image sensor (NIR-300GE, ALLIED Vision Technologies GmbH) through a lens (f = 10 cm). The device was tilted 10° with respect to the incident light to separate the reflected light from the incident light.

Figures 2.5 (b) and (c) show the playback of the BB hologram upon LCP and RCP illumination, respectively. Owing to the strong CP selectivity of ChLCs, the encoded hologram is played back only for LCP light. The conversion efficiency (η) of the hologram can be obtained through the following equation:

$$\eta = \frac{I_{\text{reflection}} - I_{\text{zero}}}{I_{\text{o}}}, \tag{2.3}$$

where I_{o} is the intensity of incident light, $I_{\text{reflection}}$ is the intensity of the reflected light from the BB hologram, and I_{zero} is the reflected zero-order intensity. The conversion efficiency of the BB hologram is 76% for LCP illumination. The optical loss is attributed to the Fresnel reflection at the interface between the device and air. In addition, as shown in Fig. 2.6, the continuous

nature of the LC orientation causes the LC alignment to deviate from the design near the interface between two adjacent pixels having different surface anchoring, resulting in a change in the Bragg reflected optical phase. Thus, a higher conversion efficiency can be achieved by using an antireflection coating on the substrate and an alignment layer with high surface anchoring.

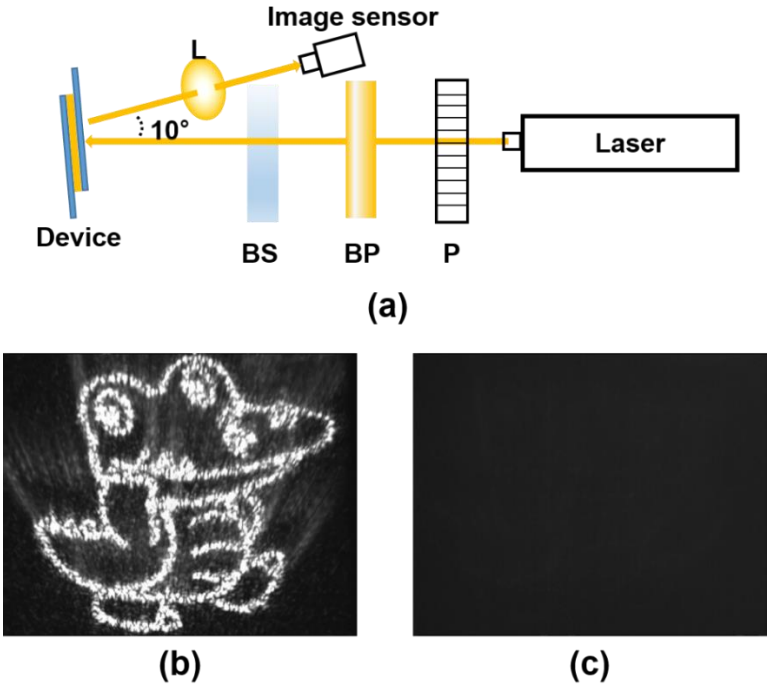


Figure 2.5 Playback of BB hologram. (a) Laser setup used to play back the hologram. P: polarizer; BP: band-pass filter (central wavelength of 1100 nm with bandwidth of 10 nm); BS: Babinet-Soleil compensator; L: focusing lens with focal length of 10 cm. (b, c) Playback of the BB hologram upon (b) LCP and (c) RCP illumination.

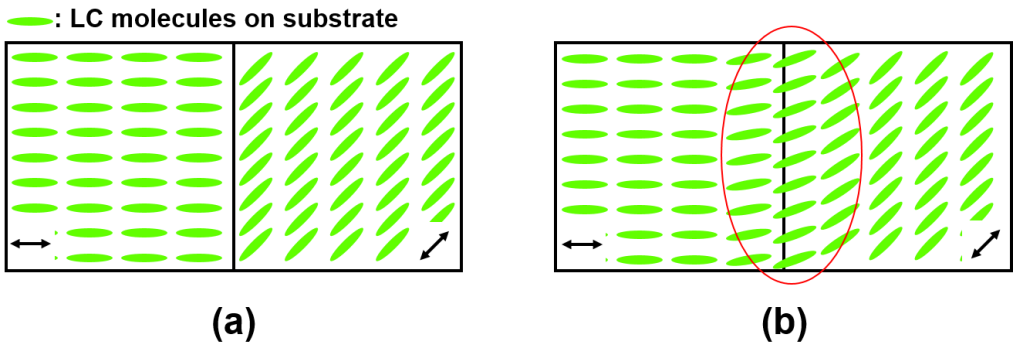


Figure 2.6 LC orientation in two adjacent pixels with different alignment directions. (a) Ideal and (b) real LC orientation between two adjacent pixels with different alignment axes. The double sided arrows indicate the orientational easy axis in the pixels.

2.4 Visible playback of BB hologram

A completely transparent BB hologram was demonstrated using a ChLC that reflects only IR light. In this section, it is demonstrated that the hologram encoded in the transparent device can be played back in the visible light region by increasing the incidence angle. First, to increase the incident angle, an index-matching triangle prism was attached to the BB hologram through an oil (IMMOIL-F30CC, Olympus), as illustrated in Fig. 2.7 (a). The refractive index of the prism (n_p = 1.5148) is measured using an Abbe refractometer (DR-M4, ATAGO) by illuminating a light with a wavelength of 580 nm. In the prism-coupled BB hologram, the incident angle on the BB hologram from the glass substrate (θ_3) can be obtained by following equation:

$$\theta_3 = \sin^{-1}\left[\frac{n_p}{n_g}\sin\left\{45° + \sin^{-1}\left(\frac{1}{n_p}\sin\theta_1\right)\right\}\right], \tag{2.4}$$

where θ_1 is the incident angle into the prism from air. Thus, the accessible angle to the BB hologram is widened from 3° to 81°, as shown in Fig. 2.7 (b).

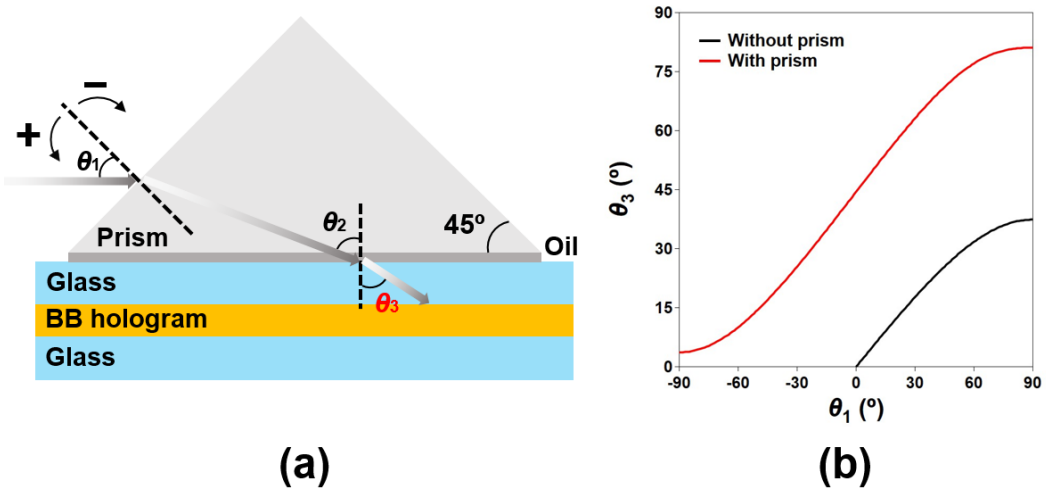


Figure 2.7 A design to increase the incident angle into the BB hologram. (a) A schematic of the prism-coupled BB hologram. (b) Effective incident angles into the BB hologram with/without the prism.

For visible playback of the BB hologram, a new source image in Fig. 2.8 (a) was used to obtain a large holographic image. The size of the source image (Dr. Wani) was enlarged by 3 times, and placed at the center of the image plane. Because the BB hologram is played back at

oblique incidence, the width of the source image is reduced by a factor of cosθ, where θ is the incident angle, to compensate the elongation of the hologram images. The source image was converted into the helical phase distribution shown in Fig. 2.8 (b) through the G-S algorithm.

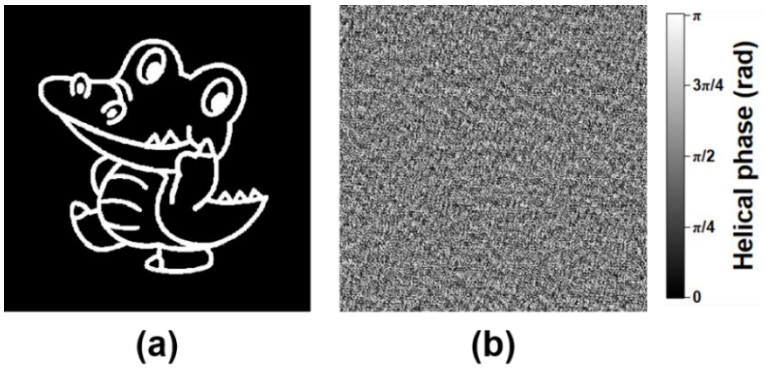


Figure 2.8 Design of the BB hologram for visible playback. (a) Source image. (b) Helical phase distribution corresponding to the source image.

For the playback of the BB hologram in the visible light region, the super continuum laser was incident to the prism at an angle of 27°, giving an incident angle to the BB hologram of 61° in the glass substrate. Figure 2.9 shows the Bragg reflection spectra of the BB hologram at 61° angle of incidence. Note that ChLCs have a total reflection band for a large angle of incidence, which reflects the light irrespective of the incident polarization. This is because the dielectric tensor distribution along direction of the light propagation is no longer a complete sinusoidal wave, resulting in the disappearance of CP selectivity. As shown in Fig. 2.9 (a), the BB hologram thus reflects both CP light around approximately 580 nm with a bandwidth of approximately 40 nm, which is well-matched with the simulations shown in Fig. 2.9 (b).

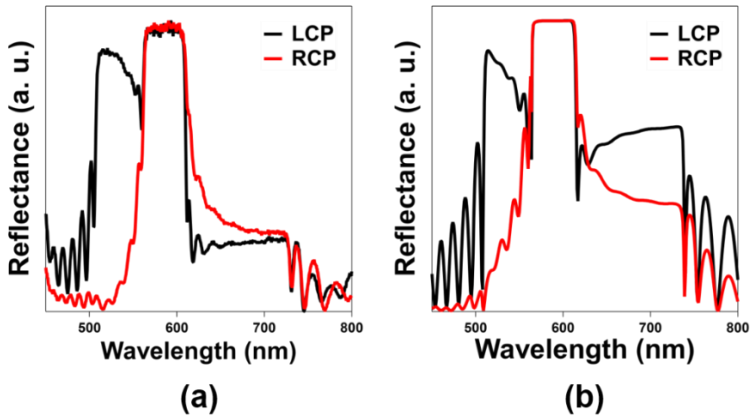


Figure 2.9 (a) Experimental and (b) simulated Bragg reflection spectra at an incident angle of 61° in the glass substrate.

The results of Fig. 2.9 imply that the BB hologram can be played back by visible light at an oblique angle of incidence. To demonstrate the capability of visible playback, a similar laser setup as shown in Fig. 2.5 (a) was used, but with a different band-pass filter (580 nm, bandwidth of 10 nm) in the optical path. The reflected light spot from the BB hologram was focused on a screen placed at a distance of 30 cm through a focusing lens (f = 15 cm), as shown in Fig. 2.10 (a). The hologram images were taken using a commercial DSLR camera. Figures 2.10 (b) and (c) show the reconstructed holographic images upon LCP and RCP illumination, demonstrating the capability of visible playback from the transparent BB hologram. The conversion efficiencies are 75% and 76% for LCP and RCP illumination, respectively.

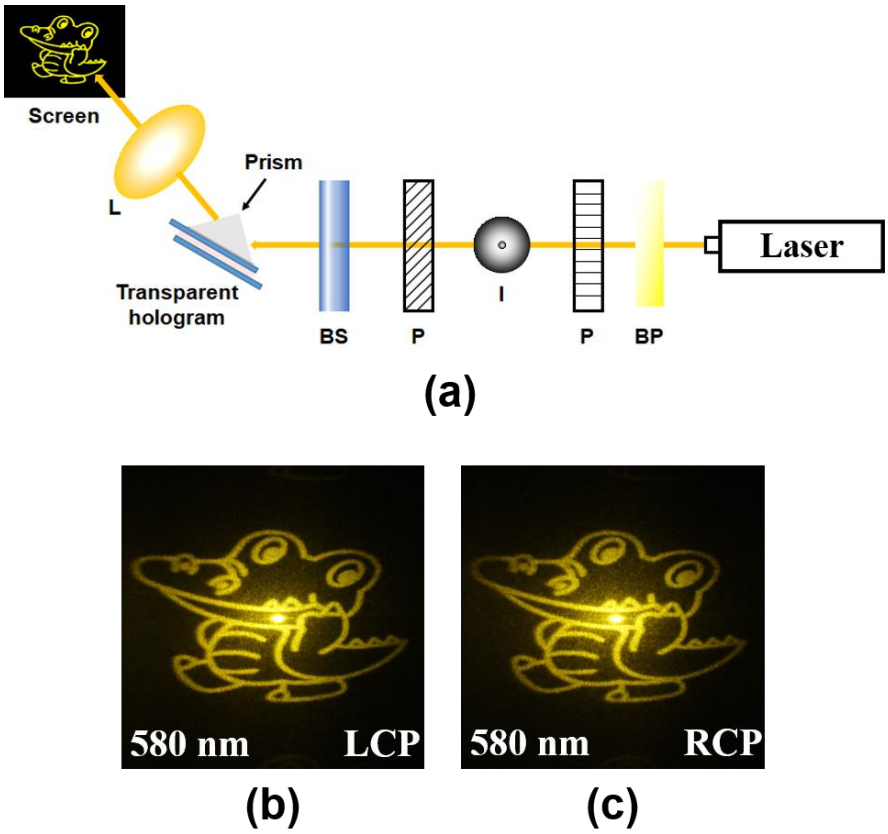


Figure 2.10 (a) Laser setup used to play back the hologram. BP: band-pass filter; P; polarizer; I; iris; BS; Barbinet-Soleil compensator; L: focusing lens (f = 15 cm). (b, c) Played back holograms for (b) LCP and (c) RCP illumination at incident angle of 61°.

2.5 Transparent computer-generated waveguide holography

As described in the previous section, the transparent BB hologram was reconstructed in the visible light region by attaching a prism onto the device. However, the prism makes the device

thick, and thus unsuitable for the realization of compact optical elements. In this section, the fabrication of a waveguide holography in which the BB hologram is coupled with a waveguide layer is described. This result provides new paradigms for realizing a compact and transparent optical system, which will be useful for various applications such as smart-glasses and head-up displays where the capability to see-through the device is required.

2.5.1 Device design and fabrication

Figure 2.11 shows the design of the waveguide holography. A glass substrate with thickness of 0.7 mm (n_g = 1.53) was used as a waveguide layer. A triangle prism was attached at the end of the waveguide layer, allowing the incident light to propagate through the layer. The light will be propagated when the propagation angle is below the critical angle given by $\sin^{-1}(1/n_g) = 41°$. In experiment, the propagation angle (θ_p) was set to 39°, giving an incident angle (θ_i) of 51° to the BB hologram coupled at another end of the waveguide layer. The BB hologram contains the optical phase information to deflect the holographic image, making the encoded hologram out-coupled from the waveguide layer and observed in free-space. The decoupled holograms were focused on a screen placed at a distance of 20 cm through a focusing lens (f = 15 cm).

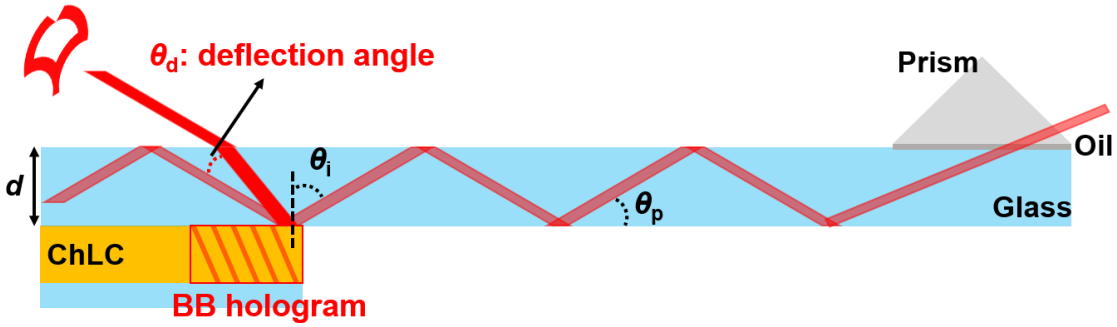


Figure 2.11 A schematic of waveguide holography. θ_p: light propagation angle in the waveguide layer. θ_i: incident angle to BB hologram. θ_d: deflection angle of light from the BB hologram. d: thickness of the waveguide layer.

To simultaneously achieve the capabilities to deflect light and generate a holographic image, a source image shown in Fig. 2.12 (a) was used in which the Osaka University logo is designed to be shown 190 pixels away from the center of the image plane in the horizontal direction. According to the diffraction theory, the deflection angle of the hologram (θ_d) is given by

$$\theta_d = \tan^{-1}\left(\frac{N_a \lambda}{nPN_x}\right), \tag{2.5}$$

where N_a is the number of pixels from the center of the image plane to the center of the holographic image, λ is the wavelength of light, n is the refractive index of the light-propagating medium, P is the pixel size, and N_x is the total number of pixels of CGH in the horizontal direction [80, 81]. In the experiment, the values were set to N_a = 190 pixels, λ = 632 nm, n = 1.0 (air), P = 0.66 μm, and N_x = 512 pixels, giving a deflection angle of the holographic image of 13.1°. This angle makes the light propagating through the waveguide layer no longer satisfy the total internal reflection condition, resulting in an out-coupling of the holographic image from the waveguide medium. The source image was converted into a helical phase distribution as shown in the Fig. 2.12 (b) through the G-S algorithm. The helix phase distribution was photo-patterned on the device with a phase step of 10°. In the patterned device, a transparent ChLC was injected at 100°C, and cooled down to room temperature (25°C). The ChLC was prepared by mixing the same nematic LC mixture and the chiral dopant, but at a different weight concentration of 98.7:1.3. The mixture shows the reflection band in a wavelength range between 1010 and 1160 nm.

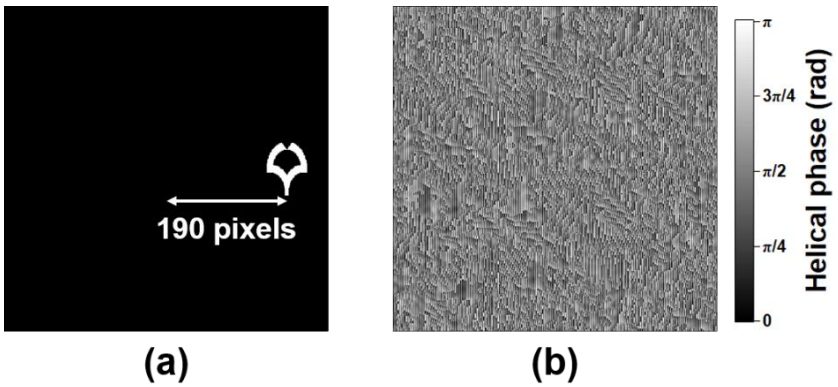


Figure 2.12 Design of the waveguide holography. (a) Source image (Osaka University logo). (b) Helical phase distribution corresponding to the source image.

2.5.2 Characterization of waveguide holography

Figure 2.13 (a) shows a photograph of the fabricated waveguide holography. The inside area of the white square indicates a region where the phase information is encoded. The average transmittance is over 88% in the entire visible light region, as shown in Fig. 2.13 (b). Because the propagating light is incident on the BB hologram at an angle of 51°, the Bragg reflection blue-shifts and is observed at a wavelength around approximately 630 nm with a bandwidth of approximately 30 nm, as shown in Fig. 2.14 (a). Figures 2.14 (b) and (c) show the out-coupled holographic images for LCP and RCP illumination observed on the screen. Holographic images are clearly reconstructed in free-space, demonstrating an ultra-compact and transparent HOEs

and the capability to display virtual information when required. The SNRs of the holographic images, defined as the maximum intensity ratio of the holographic image with respect to the standard deviation of the background noise, are evaluated as 25 for both CP lights. The SNR can be improved by employing a de-nosing algorithms in the hologram design [82] or the photo-patterning process with a higher resolution.

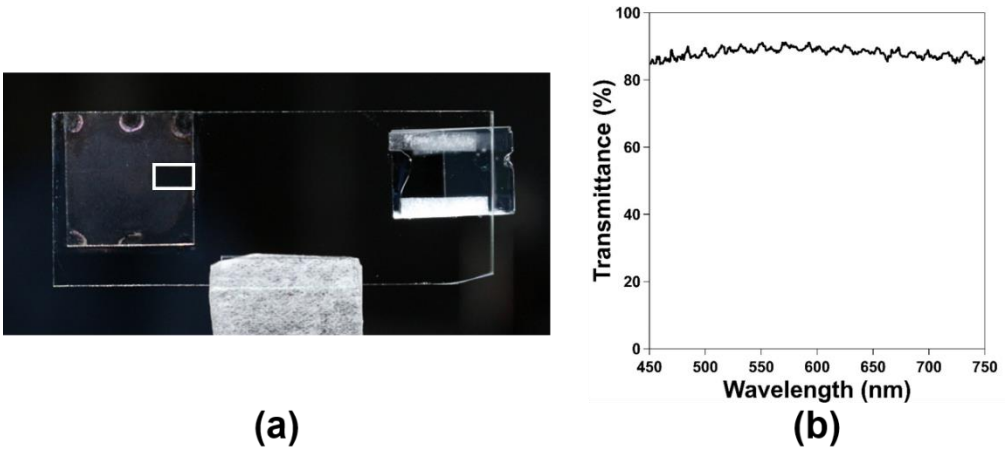


Figure 2.13 Fabricated waveguide holography. (a) A photograph of the fabricated device. The inside of the white square indicates where the phase information is encoded with a size of 8 × 4 mm^2. (b) Transmission spectrum of the waveguide holography in the visible light region.

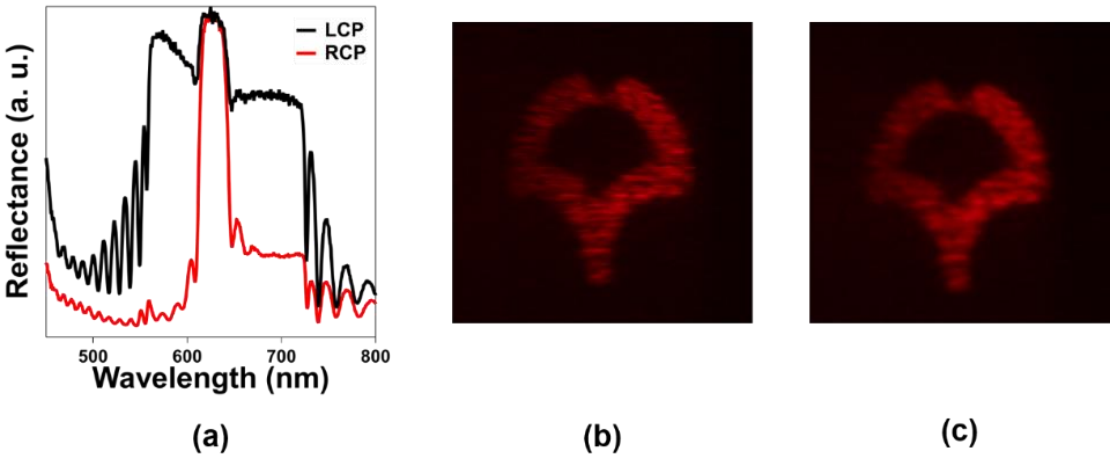


Figure 2.14 Visible playback of the waveguide BB hologram. (a) Bragg reflection spectra of the waveguide BB hologram at an incident angle of 51° upon LCP and RCP illumination. (b, c) Out-coupled holographic images by (b) LCP and (c) RCP light propagating through the waveguide layer

2.6 Discussion

In Figs. 2.8 and 2.10, the holograms were designed by the linear relationship between the reflected optical phase and the helix phase, that is, $\varphi(x, y) = \pm 0.5\Phi(x, y)$. However, the relationship is valid only for normal incidence, and generally not maintained for oblique incidence. Figure 2.15 (a) shows the phase difference between Bragg reflected *p*- and *s*-polarized components with respect to the helix phase. For normal incidence, the phase difference between two components is almost π/2 (the deviation of 0.04π is due to the Fresnel reflection at the glass substrate), meaning that the reflected light is almost circular-polarized. However, for oblique incidence, the phase difference deviates from π/2 by almost ±0.15 π as the helix phase is modulated. This implies that either the *p*- or *s*-polarized components of the Bragg reflected light do not hold the linear relationship with the helix phase, as shown in Figs. 2.15 (b) and (c). The *p*-polarized component is deviated from the linear relationship upon LCP illumination, whereas the *s*-polarized components is deviated upon RCP illumination, with a maximum deviation of 0.14 π in both cases. Thus, it is necessary to investigate how the offset affects the holograms.

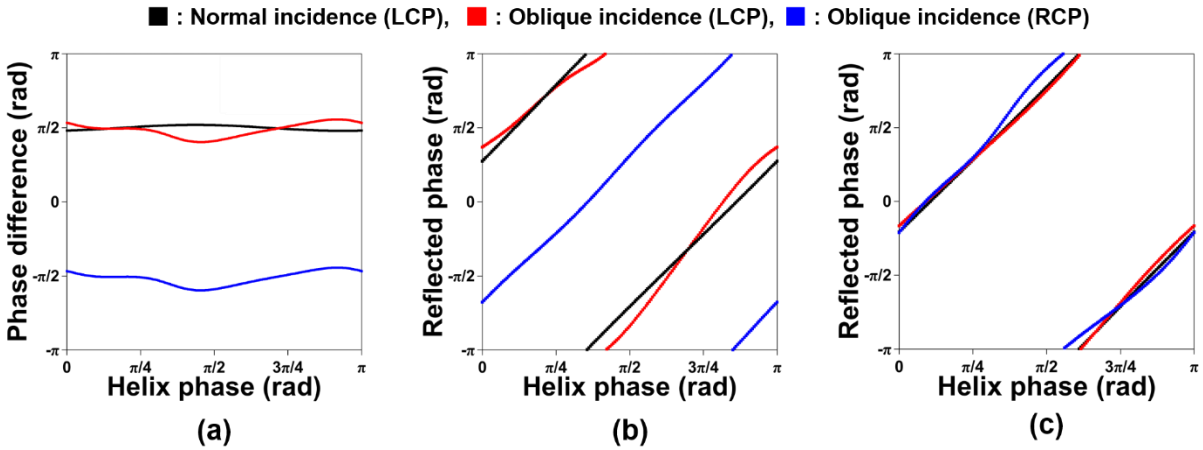


Figure 2.15 Relationship between the helix phase and reflected optical phase at normal (0°) and oblique (61°) incidence. (a) Phase difference between *p*- and *s*- polarized components. (b, c) Reflected optical phase of (b) *p*- and (c) *s*- polarized components.

The offset from linear relationship between the optical and helix phases affects the hologram efficiencies and SNRs because the holograms in Section 2.4 were designed based on the linear relationship. To investigate the effect of the offset on the hologram efficiencies, the hologram was numerically reconstructed using the Rayleigh-Sommerfeld diffraction method (see Appendix C for diffraction simulations) [80, 83]. First, as shown in Fig. 2.16, the designed

hologram used in the experiment (Fig. 2.8 (b)) was converted into the optical phase distribution using the relationship in Figs. 2.15 (b) and (c). The optical phase distributions were combined with a uniform amplitude to generate the light information on the device. The reflected light from the device was assumed to propagate a homogeneous medium (here, in air). The simulated diffraction patterns were reconstructed on a screen placed at a distance of 30 cm from the device.

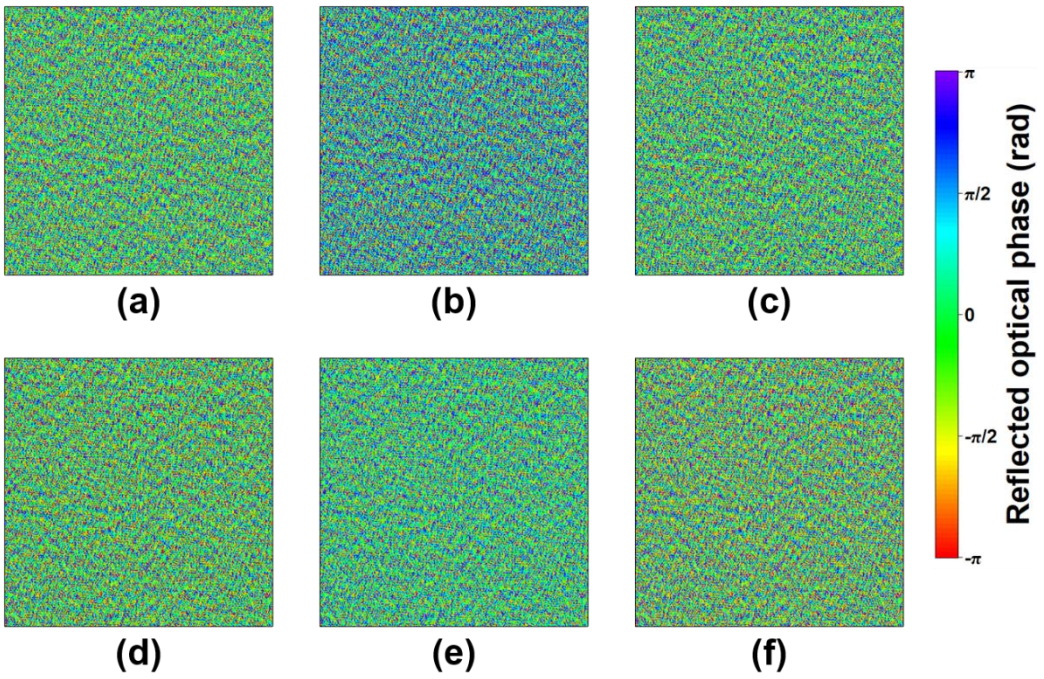


Figure 2.16 Bragg reflected optical phase distribution from the BB hologram. (a–c) Reflected *p*-polarized components. (d–f) Reflected *s*-polarized components. (a, d) For normal incidence upon LCP illumination. (b, c, e, f) For oblique incidence upon (b, e) LCP and (e, f) RCP incidence.

Figure 2.17 shows the simulated diffraction patterns that reconstruct the designed hologram in all cases. The zero-order intensities of the holograms are increased in Figs. 2.17 (b) and (f), corresponding to the *p*-polarized component for LCP illumination and *s*-polarized component for RCP illumination, respectively. However, the zero-order intensities are significantly low, which are ~0.5 % for Figs. 2.17 (a), (c), (d), and (e), and ~1.7% for Figs. 2.17 (b) and (f). Thus, this implies that the offset does not have much effect on the hologram efficiency. Although the non-linearity is increased as the angle of incidence increases, the offset in the reflected phase can be pre-compensated in the helix phase design by considering the wavelength and angle of the incident light.

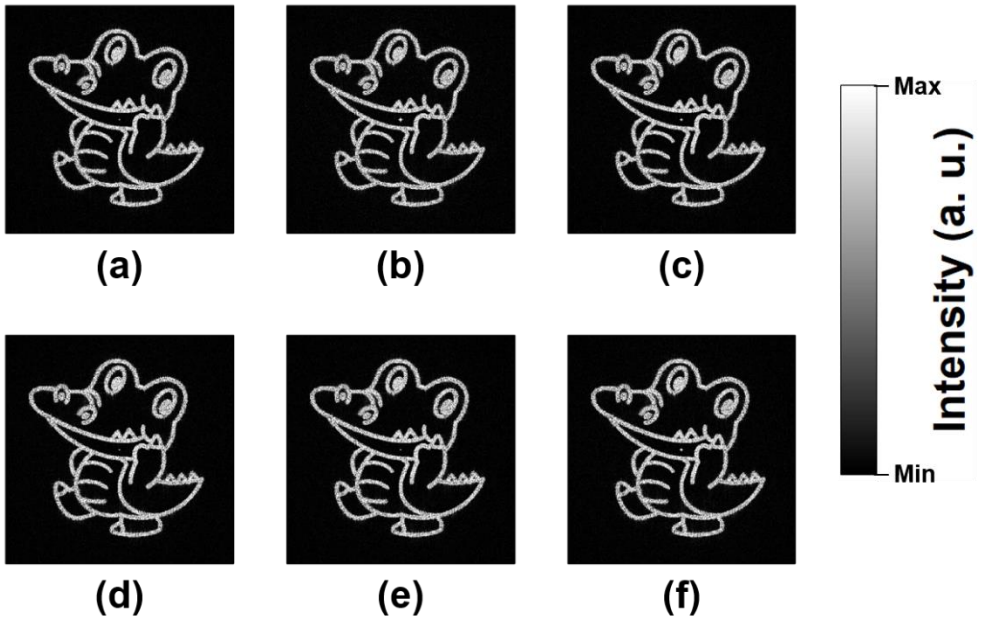


Figure 2.17 Simulated diffraction patterns from the BB hologram. (a–c) Simulated patterns with reflected *p*-polarized components upon (a) normal and (b, c) oblique (b for LCP light, c for RCP light) incidence. (d–f) Simulated patterns with reflected *s*-polarized components upon (d) normal and (e, f) oblique (e for LCP light, f for RCP light) incidence.

2.7 Conclusion

In this chapter, completely transparent HOEs are demonstrated using a ChLC that reflects only IR light. The key to achieving the optical transparency is the helical modulation of the dielectric tensor distribution, suppressing all higher-order reflections for all angles of incidence accessible from air. Based on the ChLC, BB holograms with an average transmittance of 88% in the entire visible light region were fabricated. It is also demonstrated that the encoded phase information can be played back by visible light using two optical designs: attaching an index-matching prism, and combining with the waveguide structure. In both types of devices, the holographic images are clearly visible in free-space, confirming the capability of the see-through optics. The device proposed here can be used for various applications such as augmented reality (AR) applications where transparency is required with virtual information to be displayed on the user's field of view. In addition, the device can be used as holographic security elements because the encoded phase information is completely invisible.

Chapter 3 Orientation control of 3D self-organized cubic blue phases for omnidirectional circular polarization-selective holograms

3.1 Introduction

Recent advances in HOE technology are directed toward the functionality integration, where a single device is designed to possess multiple functions. One of the intensively pursued functionalities is polarization selectivity, which allows different optical performances to be shown depending on the incident polarization. The polarization-selective devices are widely fabricated by introducing a birefringence in the sub-wavelength structures on a substrate [84, 85], which are mainly obtained by artificially controlling the nanostructures to induce a birefringence or by etching a birefringence substrate. However, extreme anisotropy requires a high aspect ratio of the nanostructures, resulting in a complexity of the fabrication processes. An alternative approach is the use of PB phase optical elements. By illuminating a CP light on an anisotropic medium with half-wave retardation, the handedness of the CP light is converted into the orthogonal CP light with an additional optical phase proportional to twice the orientation of the optic axis [65, 66]. Because the acquired optical phase is different for the handedness of the incident CP light, various CP-selective HOEs have been realized by appropriately designing the optic axis of the anisotropic medium [4, 86–88]. However, a high diffraction efficiency and polarization selectivity are enabled in only the designed wavelength and incidence angle. For example, a CP-selective HOE using NLC shows a high efficiency only when the half-retardation condition is satisfied. Metasurfaces with PB phase allow the functionality to operate in a broad range of wavelength [89, 90] and angles, but they require complex fabrication procedures such as electron and focused-ion beam lithography.

In Chapter 2, a CP-selective volume HOE was demonstrated using ChLCs that have a sinusoidal dielectric tensor distribution along the helical axis. However, the CP selectivity disappears at a large angle of incidence because the dielectric tensor distribution in a direction along the light propagation is deviated from the sinusoidal form at large incident angles. In Fig. 2.1, the total reflection band is observed at an angle of 30°, which appears at smaller angles as the refractive index of the LCs or the device thickness increases. Thus, it is not a trivial task to realize omnidirectional CP-selective HOEs because complex designs and fabrication processes of the 3D structures are required.

BPs are fantastic candidates for CP-selective devices owing to their self-organized 3D helical structures. The cubic structure enables the CP selectivity to be preserved even for large angles of incidence, which should lead to volume HOEs with acceptance angles for CP-selectivity that are wider than ChLC-based devices. However, to achieve the HOEs through BB effect [33], it is necessary to simultaneously control the crystal planes and azimuthal orientation of the BPs. A uniform crystal plane is responsible for the high light-conversion efficiency, while the azimuthal orientation enables control of the Bragg reflected optical phase. Various approaches have been proposed to control the orientation of the BP lattices such as the thermal control [91], application of an electric field [92, 93], alignment technology [94, 95], and the use of nano-patterned substrates [96]. However, they only enable control of the crystal plane orientation of the BPs on a substrate. Thus, the experimental study on BP-based HOEs are extremely rare due to the non-existence of the techniques to arbitrary control the azimuthal orientation.

In this chapter, a facile method is first proposed to independently control two crystal axes of the BPs (specifically [110] and [001] crystal axes) on a substrate through a field-reorientation process. A possible mechanism is suggested by investigating two intermediate field-induced phases: field-induced chiral nematic (N*) and BP X. The method is applied to the fabrication of an omnidirectional CP-selective hologram by appropriately controlling the azimuthal orientation of the BP lattices ([001] crystal axis) on a substrate. The omnidirectional CP selectivity is theoretically described by solving a Maxwell's equation, and experimentally supported by measuring the Bragg reflection spectrum at various angles of incidence. Because the holograms are based on the BB effect, they show a higher light-conversion efficiency (~62%) than the binary amplitude holograms using BPs [97, 98], enabling them to be applied to various applications such as see-through optics.

Second, a reflective volume deflector was demonstrated based on a simple cubic BP II. Contrast to BP I, it is well-known that the crystal orientation of a simple cubic BP II can be controlled using conventional technologies such as rubbing [94, 99] and photo-alignment [99]. By introducing a periodic modulation in the LC director on a substrate, a defect-free, large-angle (41.7°), and reflective volume deflector is achieved. A possible orientation behavior in which the [100] axis of the cubic structure becomes off-axis from device normal is suggested through the analysis of optical characteristics of the device. In addition, the ability to tune and switch the deflection is verified by examining the electro-optical characteristics of the proposed device.

3.2 Field-induced reorientation of blue phase I

As discussed in the previous section, it is necessary to control two independent crystal axes of the BP lattices to achieve the desired optical effects. In this section, a robust and facile method to manipulate two crystal axes of BPs on a substrate is presented, which is called a field-induced reorientation process. Specifically, the [110] and [001] crystal axes are independently oriented parallel to the substrate normal and the surface anchoring on a substrate, respectively. Hereafter, the BP I with (*k h l*) Miller plane oriented parallel to a substrate is referred to as BP $I_{(khl)}$.

3.2.1 Sample fabrication and materials

The BP mixture used to investigate the field-induced reorientation process was prepared by mixing two types of host nematic LCs (MLC-6849-100 and 5CB, both from Merck), a chiral dopant (S-5011, HCCH), two types of acrylate monomers (RM257 from Merck and 12CA from Tokyo chemical industry Co. Ltd.), and a photo-initiator (IrgacureOxe04, BASF). The concentration ratio by weight is summarized in Table 3.1. The two monomers and the photo-initiator were blended to *in-situ* polymer-stabilize the BP, allowing the devices to be characterized at room temperature. The chemical structures of the chiral dopant and two monomers are illustrated in Fig. 3.1. The BP mixture was dissolved in chloroform to homogeneously blend, and heated at 30°C for 2 days to evaporate the solvent.

A sandwiched cell with a gap of 9 μm was prepared using two ITO-coated glass substrates covered by the photoalignment agent. A stripe pattern of which the orientational easy axis is rotated at a step of 45° imprinted on the sandwiched cell (Fig. 3.2). Each region has a width of ~106 μm. After the patterning process, the BP mixture was filled in the patterned cell at isotropic phase and cooled to a temperature at which BP I appears (45.8°C). The temperature was modulated through a commercial hot stage (Linkam, LTS-350).

Table 3. 1 Weight concentration of the materials used to prepare the BP mixture.

	Host nematic LC mixtures (100%)		Chiral dopant	Monomers		Initiator
	MLC-6849-100 (70%)	5CB (30%)	S-5011	RM257	12CA	IrgacureOxe04
Weight ratio	61.4wt%	26.3wt%	3wt%	4.5wt%	4.5wt%	0.3wt%

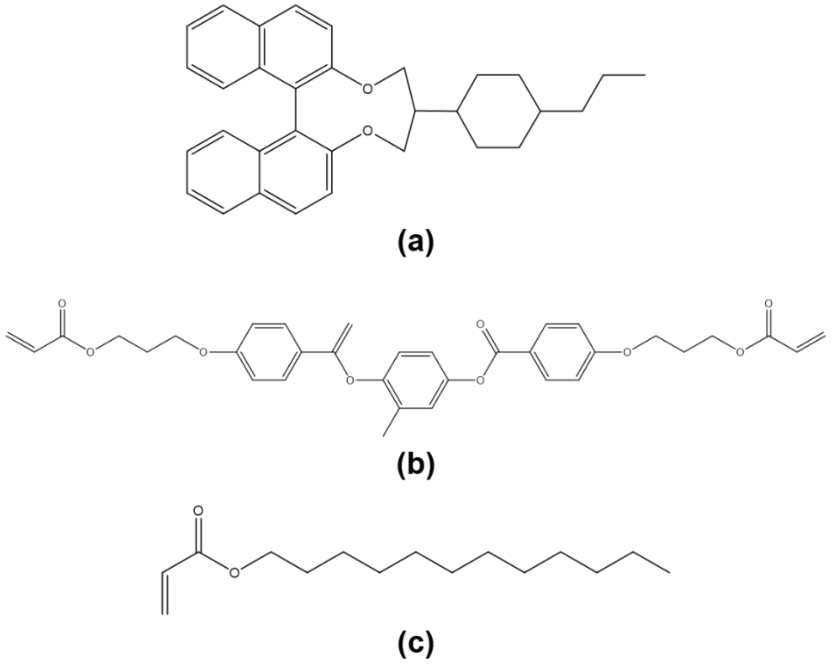


Figure 3.1 Chemical structure of the materials used for the BP mixture. (a) The chiral dopant of S-5011. (b) The reactive mesogen of RM257. (c) The isotropic monomer of 12CA.

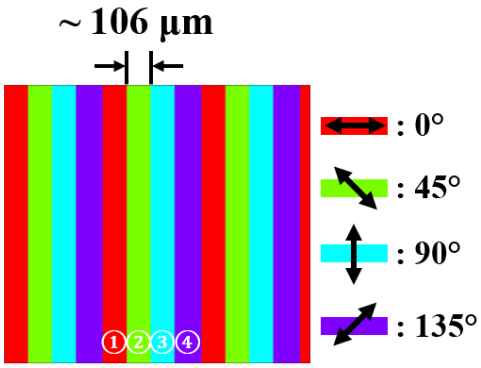


Figure 3.2 A stripe pattern used to investigate the field-reorientation process of BP I. The double-sided arrows indicate the orientational easy axis in each region.

3.2.2 Field-induced reorientation mechanism

Figure 3.3 (a) shows the POM image of the BP I obtained from isotropic state by thermal control, observed in reflection mode. The Kossel diagram in Fig. 3.3 (b) indicates that BP I has a (211) crystal plane orientated parallel to the substrate. Note that the observation of the Kossel diagram in this chapter was conducted by illuminating a light with a wavelength of 460 nm (bandwidth of 10 nm), and the diffraction light from the samples was focused at the back focal plane of a × 100 objective with numerical aperture of 0.85. The Bragg reflection of the BP $I_{(211)}$

appears at a shorter wavelength than 450 nm (the lattice constant of BP I obtained in the next section is 267 nm, giving a theoretical central reflection wavelength of BP $I_{(211)}$ at approximately 410 nm), and thus does not observed in the visible light region as shown in Fig. 3.3 (c). Because the non-uniformity and grain boundaries are observed in the BP $I_{(211)}$, it is necessary to control the crystal axes to obtain the desired optical effects from BP I.

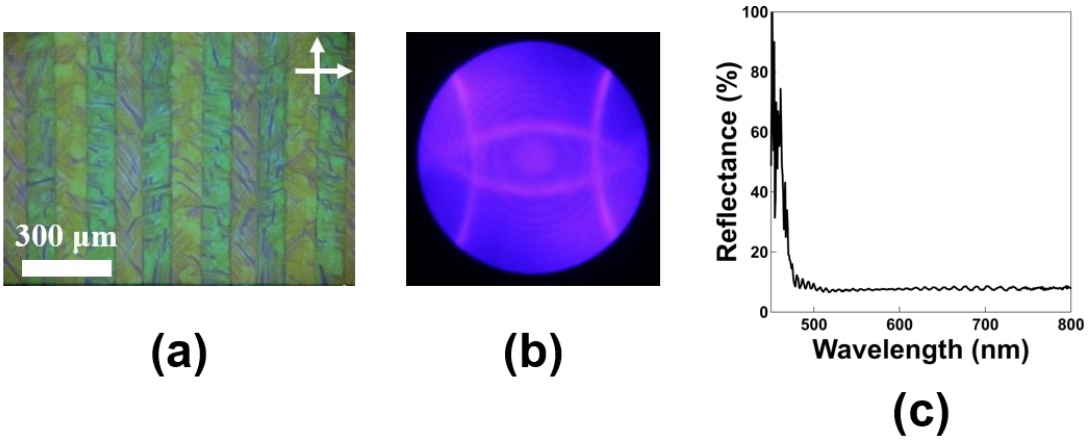


Figure 3.3 Optical characterization of the BP $I_{(211)}$ before applying an electric field. (a) POM image of BP I taken in reflection mode. (b) Kossel diagram corresponding to BP I. (c) Bragg reflection spectrum of BP $I_{(211)}$.

To reorient the crystal orientation of BP $I_{(211)}$, an electric field was applied using a function generator (Agilent 33220A Waveform Generator, Agilent Technologies) and a × 30 voltage amplifier (4010, NF Electronic Instruments). First, an AC electric field with a frequency of 1 kHz and an amplitude of 7.3 V/μm was applied between two glass substrates. Figure 3.4 shows the evolution of the POM images as the electric field is gradually decreased from 7.3 V/μm to 0 V at a rate of 0.05V/μm per min, along with the schematics of the possible orientation of the LC molecules in each field-induced phase. When 7.3 V/μm is applied to the device, a dark POM image is observed. This state corresponds to the homeotropic (H) phase in which the double-twist structure is completely unwound and the LC director is oriented along the electric field owing to the positive dielectric anisotropy of the host nematic LC. A phase-transition to the chiral nematic phase (N*) is observed at an electric field of 7.0 V/μm. In the N* phase, the LC molecules tend to align into a single twisted structure with the helical axis directed in a direction perpendicular to the surface anchoring. This result will be further discussed in detail in Sec. 3.2.2.1. At 2.7 V/μm, a phase transition occurs and a red texture is observed in the POM image. The four-fold Kossel pattern indicate the field-induced phase is the centered tetragonal BP X phase. Finally, the phase reaches an orthorhombic BP I (at 1.5 V/μm) and a body-centered BP

I (at 0 V). The POM texture of the field-induced BP I shows a different reflection color compared to the initial BP I in Fig. 3.3 (a), implying that the crystal plane of the BP I is changed. In addition, it is clearly confirmed that the distinct boundaries are observed at the interface between areas with a different orientational easy axis.

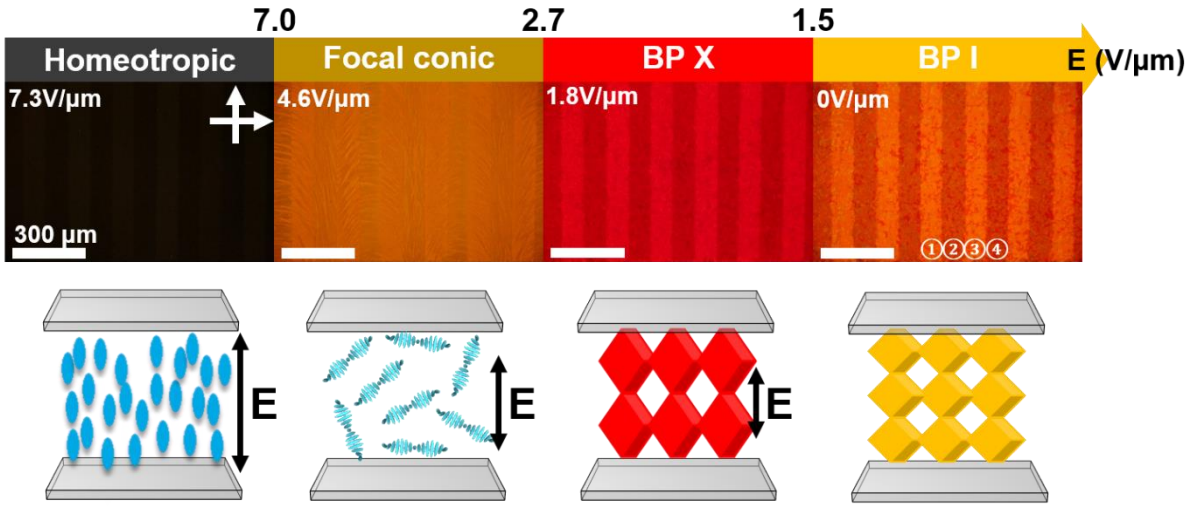


Figure 3.4 The evolution of POM images as the electric field is gradually reduced from the electrically unwound homeotropic phase, with the schematics of the LC orientation in each field-induced phase.

The orientation of the field-induced BP I was characterized through an observation of Kossel diagrams at the four regions marked by the number in the POM texture of BP I shown in Fig. 3.4. Figure 3.5 shows observed Kossel diagrams with two-fold symmetry of the diffraction patterns. The figure indicates that the field-reoriented BP I has a (110) crystal plane oriented parallel to the substrate regardless of the orientational easy axis. In addition, the Kossel patterns also shows that the [001] crystal axis is oriented along the orientational easy axis. Specifically, the [001] crystal axis is oriented along the easy axis, demonstrating that the crystal plane and the azimuthal orientation can be independently controlled on a substrate. Because of the well-aligned (110) crystal plane in the device, the corresponding Bragg reflection is also observed in the visible light region with a significantly high reflection intensity, as shown in Fig. 3.6. Thus, this process enables to uniquely define the 3D orientations of cubic BP I, allowing the BP I to be used for various optical applications such as phase-only HOEs. In the next sections, a possible mechanism of the field-reoriented BP I is investigated by controlling the electric field intensity.

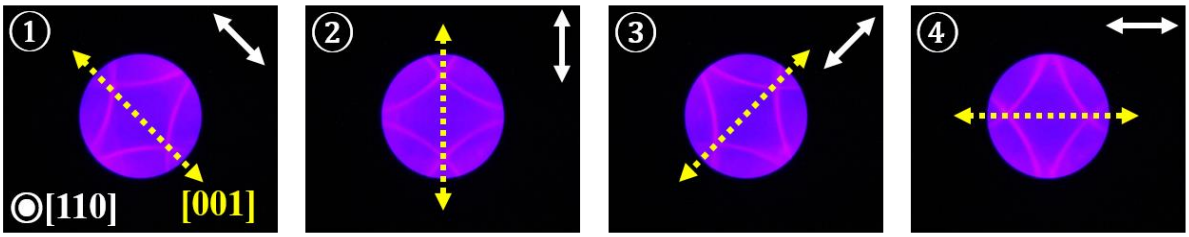


Figure 3.5 Kossel diagrams of field-induced BP $I_{(110)}$ in areas with different easy axis. The double-sided white and yellow arrows show the orientational easy axis and the [001] crystal axes of the field-reoriented BP $I_{(110)}$, respectively.

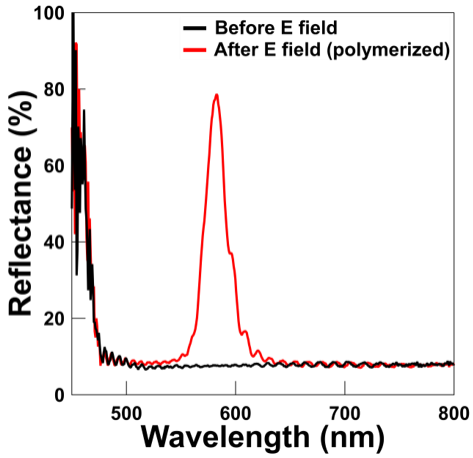


Figure 3.6 Bragg reflection spectrum of initial BP $I_{(211)}$ and field-induced BP $I_{(110)}$.

3.2.2.1 Effect on field-induced focal conic state

A uniformly aligned sandwiched cell was used to understand the field-reorientation mechanism. First, the electric field was controlled as shown in Figure 3.7 (a) to understand the effect of the N* phase at the field-reoriented BP I. At the initial BP $I_{(211)}$ (Fig. 3.7 (b)), an electric field of 7.3 V/μm was applied to induce the H phase, and reduced instantaneously to 4.5 V/μm. At this field, a phase transition to N* phase is observed, as shown in Fig. 3.7 (c), with a clear indication of the LC director orientation. The N* phase has a uniformly lying helix (ULH), which the helical axis lies in a direction parallel to the substrate. When the electric field was completely removed from the field-induced N* phase, a BP I showing two different reflection colors was obtained. The Kossel diagrams in two domains indicate that the dark and yellow domains correspond to the crystal planes of (200) and (110), respectively. Whereas the crystal planes have different orientations, the [001] crystal axes were oriented along the easy axis in both domains. Thus, the result implies that the N* phase is responsible for control of the azimuthal orientation of the succeeding BP lattice without control of the crystal plane. Thus,

the BP induced directly from the N* phase has a low reflection intensity, as shown in Fig. 3.7 (e).

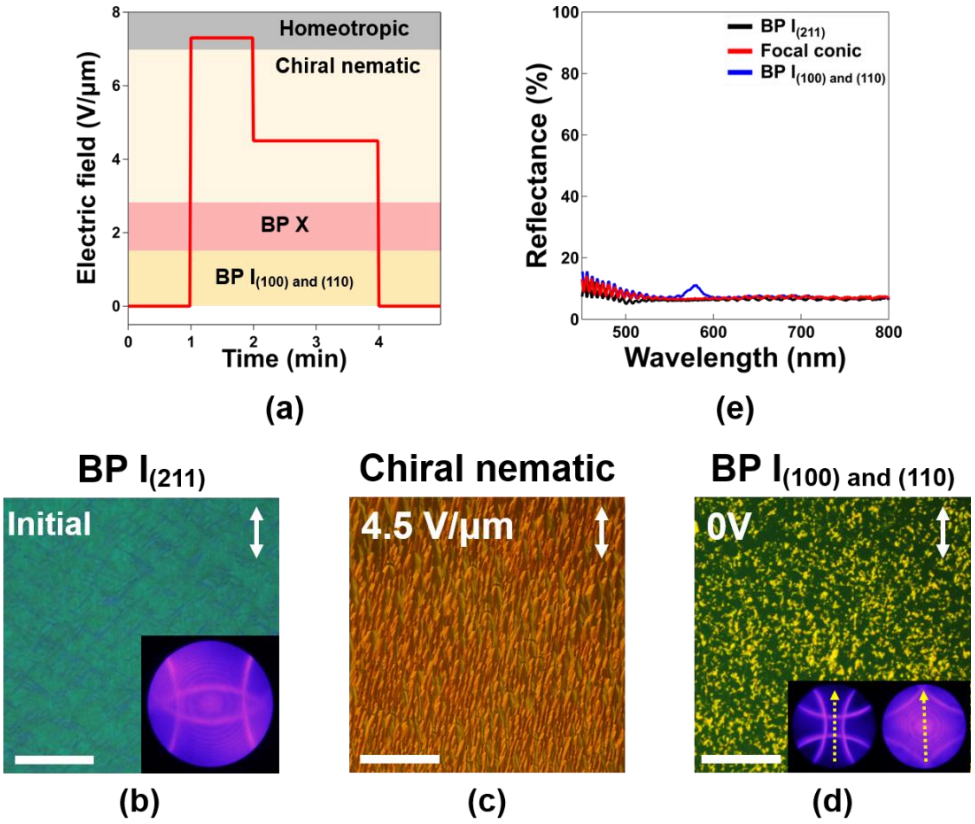


Figure 3.7 Effect of field-induced N* on the field-reorientation process. (a) Time-dependent electric field for phase transition of H–N*–BP I. (b–d) POM images of (b) initial BP $I_{(211)}$, (c) N* phase, and (d) field-reoriented BP I, with the corresponding Kossel diagrams. (e) Bragg reflection spectrum in each phase.

To confirm the effect of the field-induced N* on the orientation of the succeeding BP lattice, the helical axis of the field-induced N* was investigated using an optical setup shown in Fig. 3.8 (a). The ULH is a uniaxial birefringent medium with the refractive index parallel and perpendicular to the helical axis given by n_o and $(n_e + n_o)/2$, respectively [100]. Thus, the direction of the helical axis of the ULH can be confirmed by inserting an additional retardation plate in the optical path. In the experiment, the device was placed in the optical path such that the orientational easy axis was rotated to 45° with respect to the incident LP light. The investigation was conducted by measuring the transmission spectrum of the device with or without the retardation plate that is rotated such that the slow axis was oriented parallel to the orientational easy axis of the device. Figure 3.8 (b) shows the transmission spectrum of the

ULH with and without the retardation plate. The transmission spectrum red-shifts by inserting the retardation plate, meaning that the total birefringence of the system is increased [30]. This implies that the ULH has a higher refractive index along the orientational easy axis, and therefore, the helical axis is perpendicular to the easy axis, as shown in Fig. 3.9 (c). This is because the LC director has a planar alignment on a substrate with its orientation along the surface anchoring, but the electric field causes the LC director lying on the substrate to be rotated towards the field direction.

While the helical axis of the ULH is aligned in a direction perpendicular to the easy axis, the LC molecules on the substrate are uniformly oriented along the easy axis owing to the surface anchoring. This structure is similar to the structure of the DTCs in which the LC molecules at the center of the DTC have a uniform LC orientation and the double-twist structure is formed in a direction perpendicular to the axis of DTCs. When the electric field is removed from the field-induced N*, the twist structure is thus expanded in a direction perpendicular to those directions (parallel to the device normal), resulting in a DTC oriented in a direction along the easy axis. Therefore, the [001] crystal axis is oriented along the easy axis on a substrate.

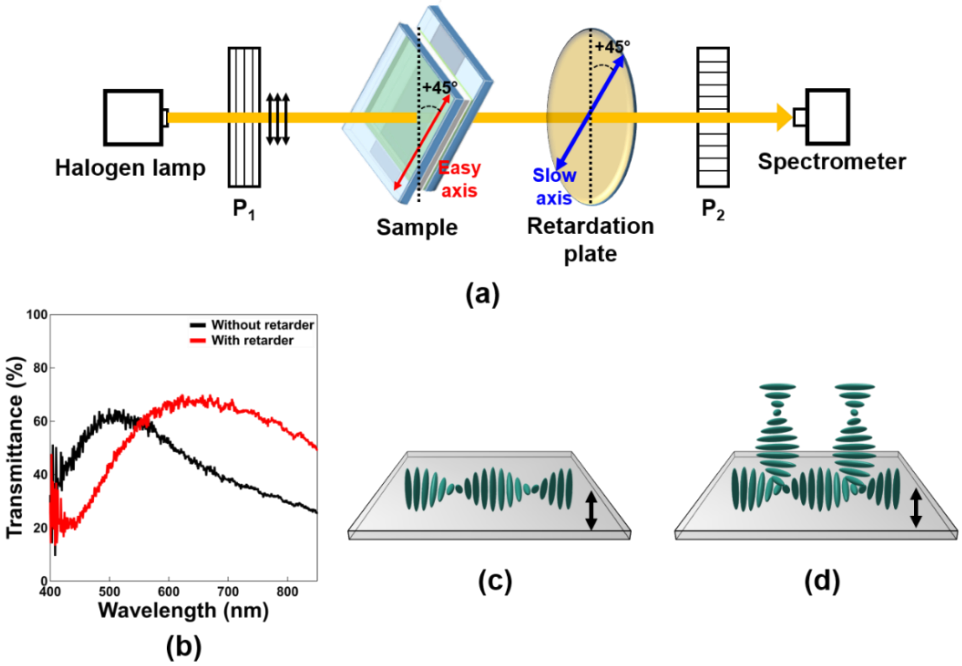


Figure 3.8 Investigation of the helical axis of N* and its orientation on a substrate. (a) An optical setup to find the helical axis of N*. (b) Transmission spectrum of N* with or without a retardation plate. (c, d) LC orientation of the (c) field-induced N* and field-induced (d) BP I on a substrate.

3.2.2.2 Effect on field-induced tetragonal blue phase X

The second experiment was conducted to confirm how the BP X affects the orientation of the succeeding field-induced BP I. The electric field was controlled, as shown in Fig. 3.9 (a), for the phase transition of H-BP X-BP I. When the electric field was directly reduced from 7.3 to 2.5 V/μm, a red texture shown in Fig. 3.9 (c) is observed. The Kossel pattern of four-fold symmetry indicates that the field-induced phase is tetragonal BP X. When the electric field is completely removed, BP I with a uniform reflection color is obtained, as shown in Fig. 3.9 (d). The observation of the Kossel diagrams reveals that the field-induced BP I shows a (110) crystal plane parallel to the substrate, but has a randomly oriented [001] crystal axis. Thus, this result implies that the BP X is responsible for the (110) crystal plane orientation, without control of the azimuthal orientation. Because of the uniform crystal plane, the field-induced BP I shows high reflection intensity as shown in Fig. 3.9 (e).

The orientation of (110) crystal plane orientation from tetragonal BP X can be explained through a continuous reorganization of the BP structure, as shown in Fig. 3.10. The [001] crystal axis of BP X is stabilized under the application of the electric field along the [110] axis of BP I. When the electric field is gradually removed, the tetragonal structure shrinks, and is transformed into an orthorhombic and body-centered BP I. From the tetragonal BP X, the transition to body-centered cubic structure with a (110) crystal plane is continuous, resulting in the (110) crystal plane to become dominant than other crystal planes that require a large amount of lattice rotation [101]. In addition, this result has been supported by numerical simulations on the BP I – BP X transition [102, 103].

In general, it is well-known that the BPs show an alignment hysteresis of which the crystal orientations are determined by the preceding structures [99]. The alignment method proposed in this chapter is a powerful approach to overcome the hysteresis because the crystal orientation of the field-induced BP I is not affected by the initial crystal orientation. Figure 3.11 shows the robustness of the field-reorientation process applied in the initial BP $I_{(211)}$ and BP $I_{(100) \text{ and } (110)}$. In all cases, only BP $I_{(110)}$ with a [001] crystal axis aligned along the easy axis is obtained, demonstrating that the field-reorientation process can be applied regardless of the initial crystal plane. This is because the double-twisted structures are erased by the electric field and the lattice orientation of the field-reoriented BP I is only affected by the field-induced N* and BP X.

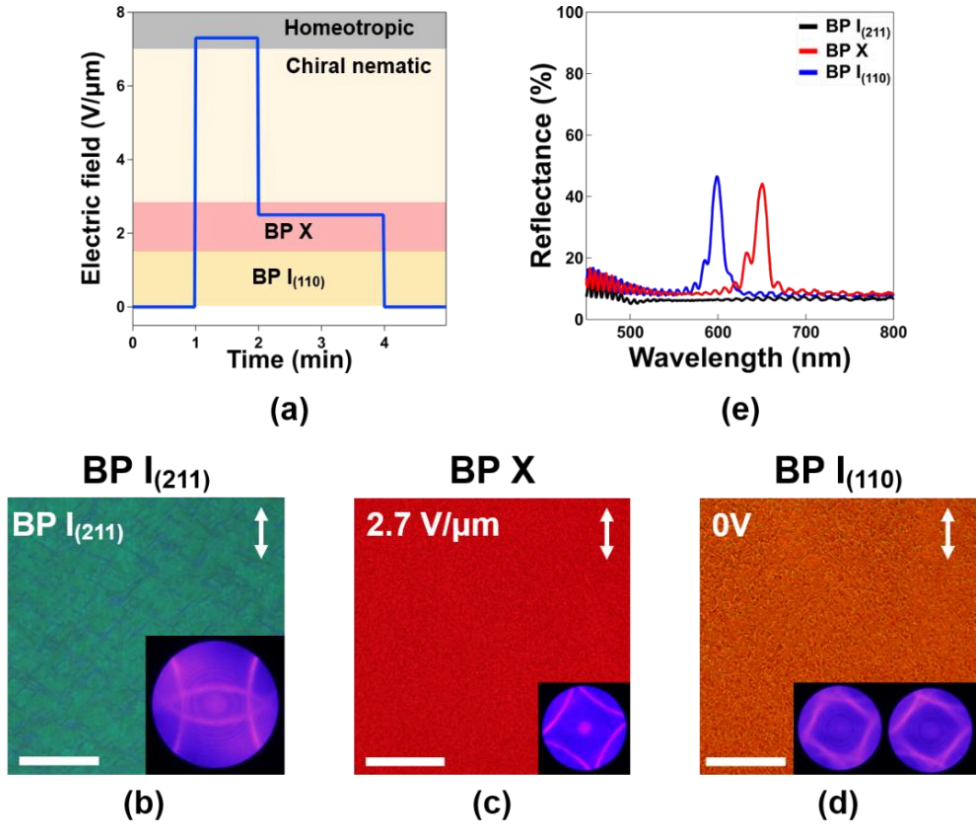


Figure 3.9 Effect of the field-induced BP X on the field-reorientation process. (a) Time-dependent electric field for phase transition of H–BP X–BP I. (b–d) POM images of (b) initial BP $I_{(211)}$, (c) BP X phase, and (d) field-reoriented BP I, with corresponding Kossel diagrams. (e) Bragg reflection spectrum in each phase.

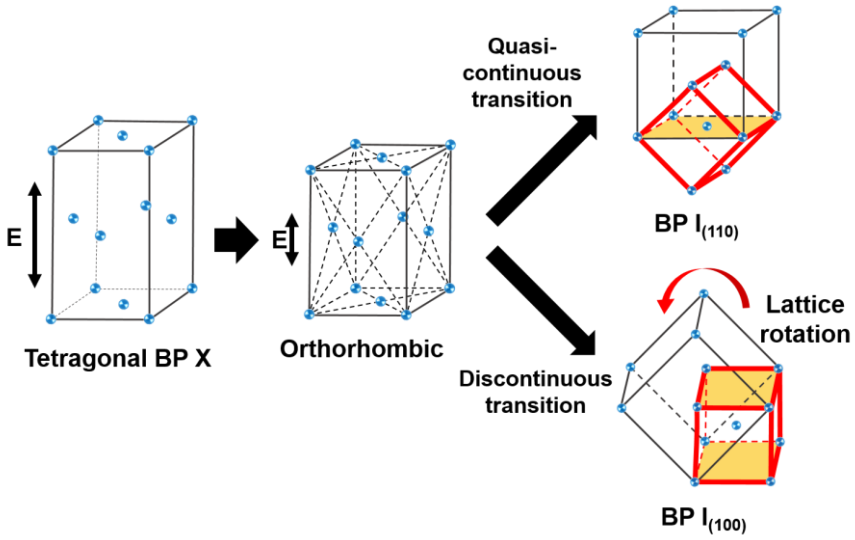


Figure 3.10 A schematic of the lattice structure during the phase transition from BP X to BP $I_{(110)}$ [101]. The cubic structures indicated by red color show the unit cell of the body-centered BP I.

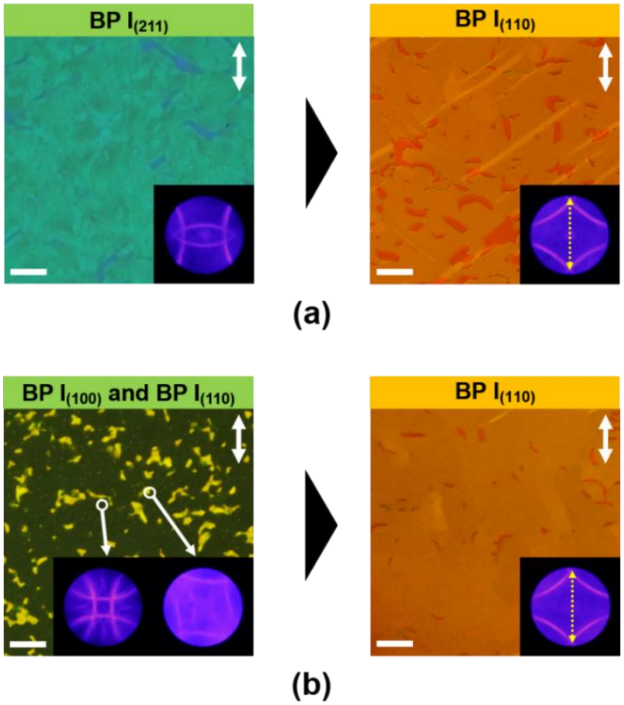


Figure 3.11 Field-induced BP $I_{(100)}$ from different initial crystal planes. POM images of field-reoriented BP $I_{(110)}$ from (a) BP $I_{(211)}$ and (b) BP $I_{(100)}$ and BP $I_{(110)}$. Scale bar: 200 μm. White double-sided arrows indicate the orientational easy axis. Yellow dotted arrows indicate the [001] direction of BP $I_{(110)}$. All images were taken in reflection mode.

3.3 Omnidirectional circular polarization-selective hologram

BPs have a tremendous potential as optical devices owing to the CP selectivity originating from its 3D helical cubic structure. However, because of the difficulty in controlling the 3D crystal orientation, the investigations on the CP selectivity for a wide range of directions are extremely rare. Although investigation of the angular dependence on the Bragg reflection of BP $I_{(110)}$ has been conducted [104], this study shows the CP-selectivity for only a limited range of incident angle (up to 37°), and does not reflect the two-fold symmetry of BP $I_{(110)}$. In this section, theoretical predictions regarding the omnidirectional CP selectivity of BP $I_{(110)}$ are provided by directly solving Maxwell's equation for the light propagation. The simulation results are supported by experimentally measuring the angular dependent Bragg reflection using a uniformly aligned BP $I_{(110)}$ obtained through the field-reorientation process. Finally, an omnidirectional CP-selective CGH is demonstrated by spatially controlling the azimuthal orientation of the BPs on a substrate.

Note that some of the contents described in this section were from a collaboration with Prof. Jun-ichi Fukuda at Kyushu University, who performed the calculations of the photonic band

structures and angular dependent Bragg reflection spectrum of BP $I_{(110)}$. Below, I describe the methods and results of the simulation, and compare the predictions with the experimental results.

3.3.1 Background

First, a theoretical analysis of the photonic band structure of BP $I_{(110)}$ is described. The dielectric tensor distribution of the BP can be obtained from the Landau-de Gennes theory, as described in Sec. 1.3. In this simulation, the rescaled material parameters were set as τ = -1, κ = 0.7, and η = 1. The BP was assumed as having a right-helix (σ = +1) with refractive indices of n_o = 1.50 and n_e = 1.64. The periodic dielectric tensor can be expressed using a Fourier series applying the inverse lattice vector **G** as

$$\varepsilon(\mathbf{r}) = \sum_{\mathbf{G}} \varepsilon(\mathbf{G}) \exp(i\,\mathbf{G}\cdot\mathbf{r}). \tag{3.1}$$

The photonic band structures can be calculated by solving the Maxwell's equation without free-charge in the frequency domain as follows:

$$\nabla \times \left(\overleftrightarrow{\varepsilon^{-1}(\mathbf{r})} \nabla \times \boldsymbol{H}(\mathbf{r}) \right) = \left(\frac{\omega}{c} \right)^2 \boldsymbol{H}(\mathbf{r}), \tag{3.2}$$

where ω is the eigen frequency, c is the speed of light in vacuum, and $\overleftrightarrow{\varepsilon^{-1}(\mathbf{r})}$ is the inverse dielectric tensor distribution. Eq. (3.2) can describe the behavior of light within a periodic structure. Thus, by solving Eq. (3.2) in various directions of light propagation (expressed as wavevectors in the calculation results), the frequency at which the light traveling through the periodic media is allowed or forbidden can be determined. Block vector $\boldsymbol{k}$ can be expanded into a Fourier series as follows:

$$\boldsymbol{H}_{\boldsymbol{k}}(\mathbf{r}) = \sum_{\boldsymbol{G}} \boldsymbol{H}_{\boldsymbol{k}}(\boldsymbol{G}) \boldsymbol{e}^{\boldsymbol{i}(\boldsymbol{k}+\boldsymbol{G})\cdot\mathbf{r}}, \tag{3.3}$$

where $\boldsymbol{G}$ is the reciprocal lattice vector. In this section, I describe the calculation results obtained by solving the eigen-frequency of $\boldsymbol{H}_{\boldsymbol{k}}(\boldsymbol{G})$ within the time domain through the plane-wave expansion method [105].

Figure 3.12 shows the calculation results of the photonic band structures and their propagating eigen-polarizations. Because of the two-fold symmetry of the BP $I_{(110)}$, the Bloch vector $\boldsymbol{k}$ is rotated around the [001] and $[\bar{1}10]$ crystal axes from the [110] crystal axis as shown in Fig. 3.12 (a). In Fig. 3.12 (b), when the incident angle is rotated around the [001] crystal axis, the 1st to 4th bands related to the Bragg reflection from the (110) crystal plane blue-shifts as the incident angle increases. In addition, the presence of 5th to 8th confirms the existence of another reflection band. The bands appear at 30°, and red-shift as the incident angle is increased.

These bands originate from the Bragg reflection from the (101) and $(10\bar{1})$ crystal planes, which will be described in Fig. 3.16. On the other hand, as shown in Fig. 3.12 (c), when the incident angle is rotated around the $[\bar{1}10]$ crystal axis, the band structures are slightly complex because each band responsible for the Bragg reflection is different depending on the angle of incidence. The Bragg reflection from the (110) crystal plane originates from the 1st to 4th bands for less than 36° incidence, and the 5th to 8th for more than 36° incidence. Moreover, an additional Bragg reflection appears at the incident angle of 20°, which originates from the (101) and (011) crystal planes. This reflection causes the 5th to 8th bands for an angle less than 36° and crossed with the 1st to 4th bands at 36°. The reason for the complex band structure can be explained by examining the effective incident angles on each crystal plane, which will be also described in Fig. 3.16. Figures 3.12 (d) and (e) show the polarization state of the propagating electromagnetic wave in BP $I_{(110)}$ for each band. In Fig. 3.12 (d), the polarization state of the 1st and 4th bands are left-circular polarized and 2nd and 3rd bands are right-circular polarized. On the other band, in Fig. 3.12 (e), the polarization of the 1st and 4th band (below 36°) and 5th and 8th bands (above 36°) is left-circular polarized. This result implies that the reflected light from BP $I_{(110)}$ is almost circularly polarized for all angles of incidence.

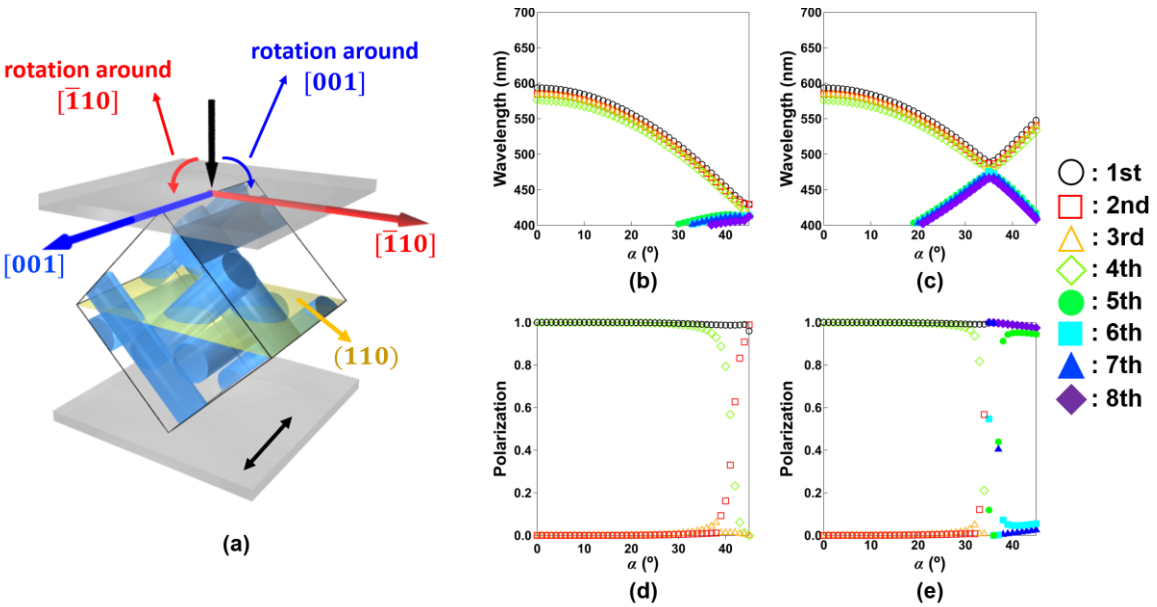


Figure 3.12 (a) Schematic of uniformly aligned BP $I_{(110)}$ indicating two rotation modes. (b, c) Simulated photonic band structures and (d, e) propagating eigen-polarization when the incident angle is rotated around the (b, d) [001] and (c, e) [$\bar{1}$10] crystal axes from the [110] axis.

Because the calculation of the photonic band structures was obtained by assuming that the thickness of the BP structure is infinite, it cannot fully explain the CP-selectivity of the BP $I_{(110)}$ with finite thickness. Therefore, the angular dependent Bragg reflection spectra of the BP $I_{(110)}$ was also analyzed to support the omnidirectional CP-selectivity. For the calculation, the BP $I_{(110)}$ with a thickness of 6.04 μm was assumed to be sandwiched between homogeneous infinite media with a refractive index of 1.53 (glass substrate in experiment). The lattice constant of the BP $I_{(110)}$ was set to 267 nm. The calculation results were obtained by solving the Maxwell's equation with the combination of plane-wave expansion method (along *x*-*y* plane) and finite-difference discretization (along *z*-axis) [106, 107].

Figure 3.13 shows the simulation results when the incident angle is rotated along the [001] and $[\bar{1}10]$ crystal axes from the [110] axis. In both results, it is clearly confirmed that the Bragg reflection spectrum from the (110) crystal planes appears in only the LCP illumination and blue-shifts as the incident angle increases. On the other hand, no reflection bands are observed for the RCL illumination, confirming the omnidirectional CP selectivity of the BP $I_{(110)}$ irrespective of the rotation modes. In addition, similar to the photonic band structure, the additional reflection band is observed when the incident angle is rotated around the $[\bar{1}10]$ crystal axis. The reflection band red-shifts as the incident angle increases. This is the reflection band originating from the (101) and (011) crystal planes, which will be described in Fig. 3.16.

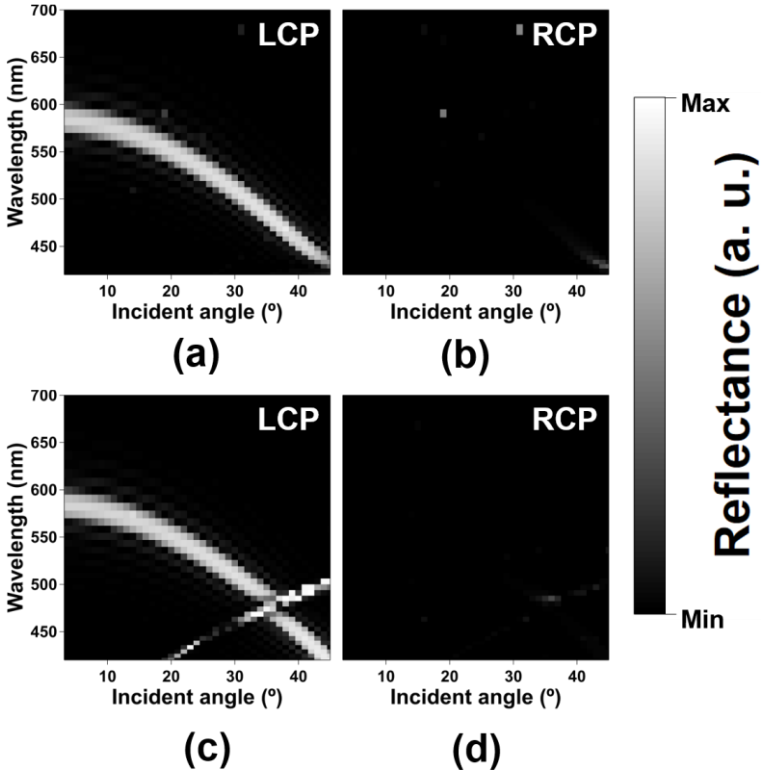


Figure 3.13 Simulated angular dependent Bragg reflection of BP $I_{(110)}$ as the incident angle is rotated around the (a, b) [001] and (c, d) [$\bar{1}$10] crystal axes from the [110] directions. The polarization of incident light is (a, c) LCP and (b, d) RCP illumination.

Now, the simulation results are supported by experimentally investigating the angular dependent Bragg reflection spectrum. For the experiment, BP $I_{(110)}$ with its [001] crystal axis homogeneously aligned on a substrate was prepared. The field-induced BP $I_{(110)}$ was *in-situ* photo-polymerized by illuminating a ultraviolet (UV) light (10 mW/cm^2) for 30 min such that the measurement can be possible in room temperature. An optical setup with a Xenon lamp was used to illuminate a white light on the sample, as illustrated in Fig. 3.14. The polarization of incident light was controlled by placing a polarizer and a QWP in the optical path. The reflected light was detected by an optical fiber (diameter is 1mm) connected to a spectrometer (PMA-11, Hamamatsu). In common with the simulations, the sample was placed on a rotatable stage, and rotated around the [001] and [$\bar{1}$10] crystal axis from the [110] axis. To minimize the Fresnel reflection from the glass substrate, a triangle prism was attached through an index-matching oil when the incident angle is over 30°. Figure 3.15 shows the experimental angular dependent Bragg reflection from the BP $I_{(110)}$. The CP-selectivity is preserved up to 45° regardless of the rotation modes. When the device is placed in air, the incident angle is limited up to 41° owing

to the refraction, and thus, the BP $I_{(110)}$ possesses the CP selectivity for all angles of incidence accessible from air.

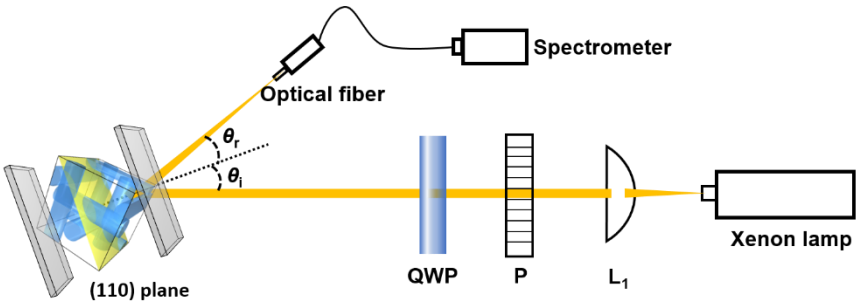


Figure 3.14 A laser setup used to measure the angular dependent Bragg reflection spectrum of the field-induced BP $I_{(110)}$.

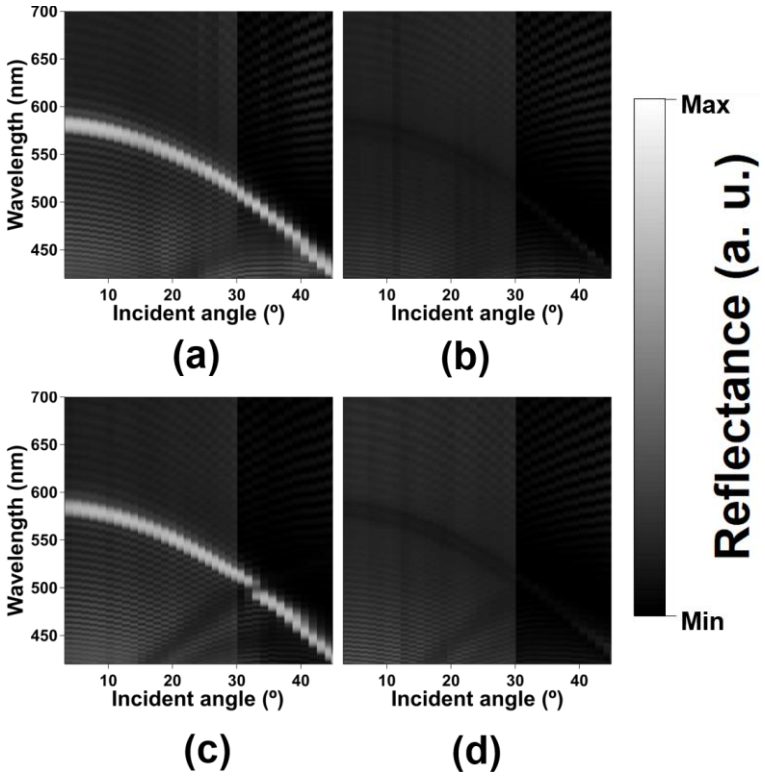


Figure 3.15 Experimental angular dependent Bragg reflection of BP $I_{(110)}$ as the incident angle is rotated around the (a, b) [001] and (c, d) [$\bar{1}$10] crystal axes from the [110] axis. The polarization of incident light is (a, c) LCP and (b, d) RCP illumination.

Now, the description of the additional reflection band observed at incident angles above 20° when the incident angle is rotated around the [$\bar{1}$10] crystal axis is provided. For the investigation, the effective incident angles (θ_{eff}) on six {110} crystal planes were calculated

depending on the rotation modes. The values of θ_{eff} were obtained through the inner product of the vectors between the propagation direction of light and the normal direction and each crystal plane. The central wavelength of the Bragg reflection band (λ_{center}) can be obtained as follows:

$$\lambda_{\text{center}} = \frac{2na\cos\theta_{\text{eff}}}{\sqrt{h^2+k^2+l^2}} \tag{1.6}$$

Thus, λ_{center} are consistent when light is incident at the same angle in the six {110} crystal planes of BP I. In Fig. 3.16 (a), θ_{eff} is always above 45° except for the incident light to the (110) crystal plane when the incident angle is rotated around the [001] crystal axis, and thus only the reflection from the (110) crystal plane is observed in the visible light region, and all reflections from the other crystal planes appear in a shorter wavelength than 400 nm (because the incident angle is large). On the other hand, when the incident angle is rotated around the $[\bar{1}10]$ crystal axis as shown in Fig. 3.16 (b), the values of θ_{eff} at the (101) and (011) crystal planes are decreased from 60° to 31°, causing a red-shift of the Bragg reflection spectrum. This is consistent with the results in Figs. 3.13 (c) and 3.15 (c), where the Bragg reflection starts to be observed at an incident angle of 20° (corresponding to θ_{eff} of 45° at the (101) and (011) crystal planes) and red-shifts. However, the bright reflection band from the (101) and (011) crystal planes (Fig. 3.13 (c)) is observed as a dark band in the experiment (Fig. 3.15 (c)). This is because, in the simulation, the BP is assumed to be sandwiched by two glass substrates with infinite thickness. By contrast, the sample for the experiment are composed by two glass substrates with a thickness of 0.7 mm, and the reflected light is detected in free-space. When the reflection angles from the (101) and (011) crystal planes are larger than the total reflection condition, the light cannot be out-coupled from the glass substrate, and guided through the substrate. The reflections are thus not observed in free-space for the experiment, but are observed as dark bands because they reduce Fresnel reflections.

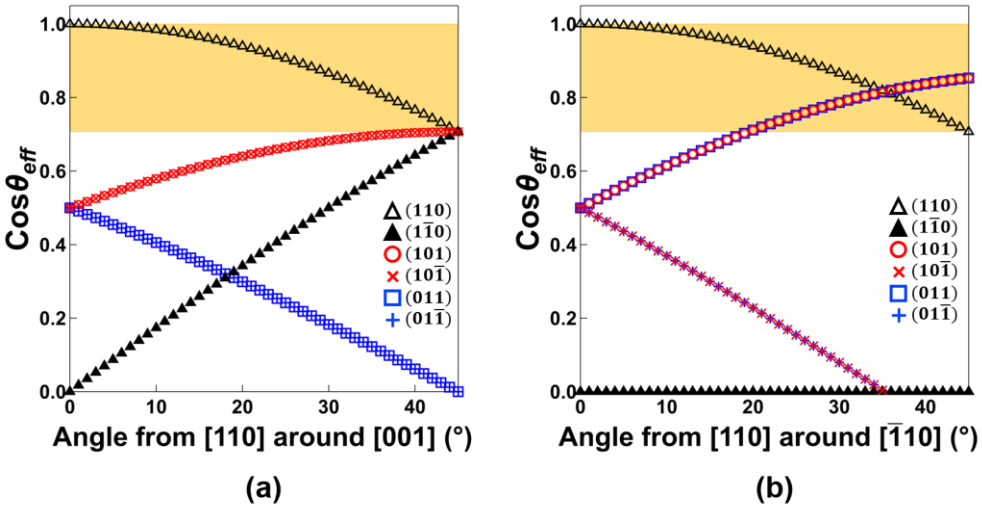


Figure 3.16 Effective incident angle depending on the Miller indices when the incident angle is rotated around the (a) [001] and (b) [$\bar{1}$10] crystal axes from the [110] crystal axis.

3.3.2 Device design and fabrication

The source image shown in Fig. 3.17 (a) was prepared for the fabrication of the omnidirectional CP-selective hologram. The source image was converted into an azimuthal orientation distribution using the G-S algorithm [11, 12], as shown in Fig. 3.17 (b). The azimuthal orientation distribution was imprinted on a sandwiched cell with a gap of 9 μm using the maskless photo-patterning process described in Section 1.4 with a phase step of 10° (18 phase levels). The pixel size of the patterning process was 2.7 × 2.7 μm^2 with the total pixel resolution of 512 × 384, giving a patterned area of 1.3 × 1.0 mm^2. The patterns with a 2 × 2 array was fabricated, giving a total size of the hologram device of 2.6 × 2.0 mm^2. The BP mixture shown in Table 3.1 was injected in the photo-patterned cell, and the crystal orientation was controlled using the field-reorientation process. After controlling the crystal orientation, the device was illuminated by UV light (10 mW/cm^2) for 30 min to *in-situ* polymerize the device.

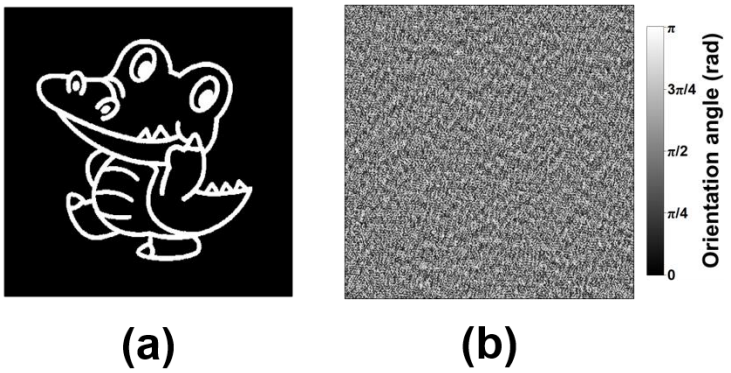


Figure 3.17 Hologram design. (a) Source image. (b) Azimuthal orientation distribution for BP-based hologram.

The fabricated BP-based hologram was characterized by the observation of the POM texture and Bragg reflection spectrum, as shown in Fig. 3.18. Despite the spatial patterning on the alignment easy axis, it was confirmed that the crystal planes of the (211) and (110) of the initial BP I was obviously tuned to only the (110) crystal orientation with orange reflection color, as shown in Figs. 3.18 (a) and (b). The corresponding Kossel diagram overlapping several two-fold symmetry lines indicate that the azimuthal orientation is varied on a substrate owing to the patterning. Because of the (110) crystal plane orientation, the reflection band appears in the visible light region (Fig. 3.18 (c)) with the peak wavelength of 585 nm. In addition, due to the 3D helical structure of the BPs, the CP selectivity in the Bragg reflection is observed for normal incidence, as shown in Fig. 3.18 (d).

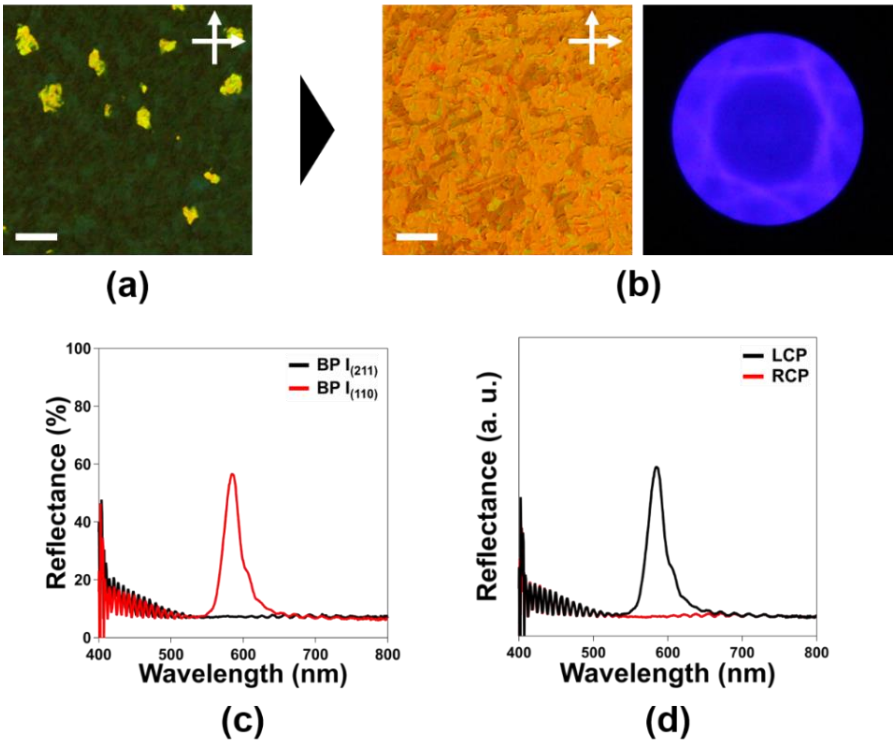


Figure 3.18 Optical characteristics of BP-based hologram. (a) POM texture before field-reorientation process. (b) POM texture after field-reorientation process, along with the corresponding Kossel diagram. Scale bar: 200 μm. (c) Bragg reflection spectrum before and after field-reorientation process. (d) Bragg reflection spectrum of the field-reoriented BP I upon LCP and RCP illumination.

3.3.3 Hologram generation at various incident angles

The omnidirectional CP-selective hologram was observed using the same laser setup in Fig. 2.10 (a), but with different band-pass filters. The hologram was played back at three different angles of 7°, 29°, and 40° by inserting band-pass filters with a central wavelength of 580, 520, and 460 nm, respectively, with bandwidth of 10 nm. The reflected light spot was focused on the screen placed at a distance of 30 cm from the sample. Figure 3.19 shows hologram images reconstructed at the three different angles upon LCP and RCP illumination. For all angles of incidence, the holograms are reconstructed only by LCP light illumination, whereas only Fresnel reflections are observed upon RCP illumination, demonstrating the capability of omnidirectional CP-selective HOEs. The dichroic ratio (***R***) of the hologram is defined by the following equation:

$$\boldsymbol{R} = \frac{I_{LCP} - I_{0_LCP}}{I_{RCP} - I_{0_RCP}} \tag{3.4}$$

where I_{LCP} and I_{RCP} is the intensity of total reflected light, and I_{0_LCP} and I_{0_RCP} are the zero-order intensity upon LCP and RCP illumination, respectively. The measured dichroic ratio is 84 for the yellow hologram and 86 for the green and blue holograms.

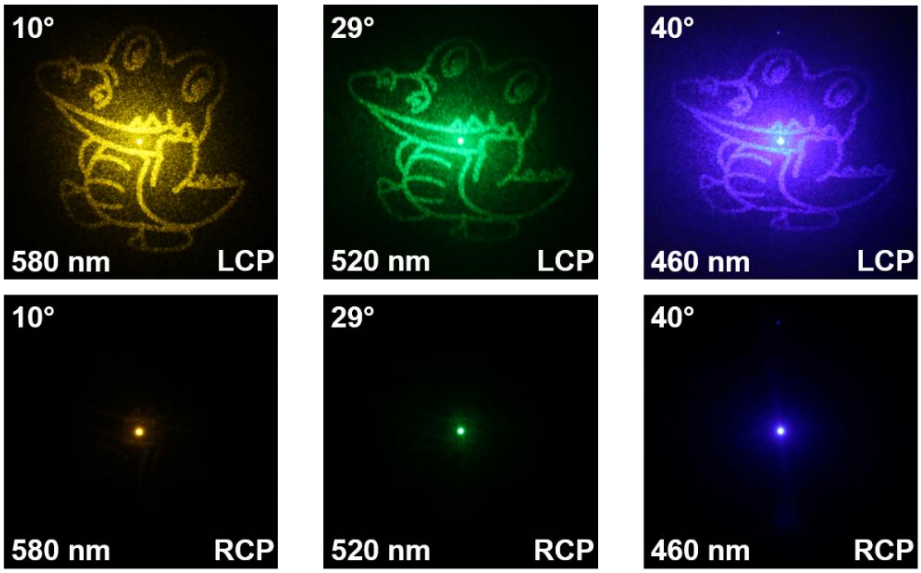


Figure 3.19 Demonstration of omnidirectional CP-selective hologram fabricated using field-reoriented BP $I_{(110)}$.

3.4 Circular-polarized, large-angle, and reflective volume grating based on simple cubic BP II

In the previous section, the field-reorientation process was proposed for controlling the 3D orientation of BP I on a photo-patterned substrate. In contrast to the BP I, it is well-known that a simple cubic BP II enables control of the 3D crystal orientation on a substrate using conventional alignment methods such as a rubbing process [94] and photo-alignment [99]. In this section, a circular-polarized, large-angle, and reflective HOEs is demonstrated using simple cubic BP II by spatially patterning the LC orientation on a substrate.

3.4.1 Sample fabrication

A sandwiched cell with a gap of 8 μm was prepared, as described in Sec. 3.2.1. For the patterning process, a polarization holography method [34, 78] was used to spatially modulate the azimuthal orientation of the BP crystals on a substrate. This method enables the formation of an interference pattern with periodically rotating LP light in a sub-wavelength scale. During

the patterning process, the sandwiched cell was rotated to an angle of 20°, giving a theoretical period of 713 nm. The detail of the patterning process will be described in Sec. 4.3.1.

A BP mixture was prepared by mixing the two types of nematic LCs and a left-handed chiral dopant at a weight concentration described in Table 3.2. The mixture shows a phase sequence of isotropic phase – BP II (47.5°C) – BP I (45.9°C) – cholesteric phase (43.5°C) during the cooling process. The BP mixture was injected in the photo-patterned cell at an isotropic state (50°C), and cooled down to a temperature where BP II appears (46.1°C).

Table 3. 2 Weight concentration of the materials used to prepare the BP mixture for a BP-based BB deflector.

	Host nematic LC mixtures (100%)		Chiral dopant
	MLC-6849-100 (50%)	5CB (50%)	S-5011
Weight ratio	48.45wt%	48.45wt%	3.1wt%

3.4.2 Lattice structure in photo-patterned BP II

First, a possible lattice structure in the photo-patterned BP II is suggested. The Kossel diagrams, transmission spectra, and observation of diffracted light spots, which are discussed below, suggest the device to have a simple cubic symmetry with its [100] crystal axis slanted at an angle of $\alpha = \sin^{-1}(a/\alpha)$ from the device normal, as shown in Fig. 3.20. Compared to a conventional BP II with its [100] crystal axis oriented along the device normal, the slant structure makes the periodicity along the device normal to be shifted by a factor of cos(α). Thus, λ_c for normal incidence can be expressed as follows:

$$\lambda_c = \frac{2 n_a a}{\sqrt{h^2 + k^2 + l^2}} \cos(\alpha), \tag{3.5}$$

where n_a is the average refractive index of BP II, which is obtained by $n_a = \sqrt{(2 n_o^{\,2} + n_e^{\,2})/3}$. For a normal incidence, the light is reflected by an angle of 2α in the device, and refracted at the interface between the device and air according to Snell's law. Thus, the deflection of light in free-space (θ_d) when illuminated by light with wavelength of λ_c is expressed as follows:

$$\theta_d = \sin^{-1}\left(\frac{\lambda_c}{\Lambda}\right). \tag{3.6}$$

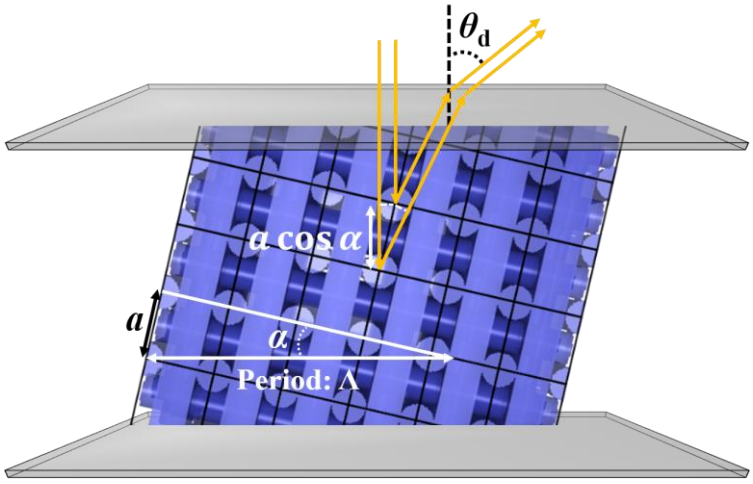


Figure 3.20 Proposed lattice structure of BP II in the patterned cell. The [100] crystal axis of simple cubic BP II is tilted at an angle of α with respect to the device normal.

Figure 3.21 (a) shows the POM image of the BP observed in reflection mode by illuminating a LCP light. A macroscopic defect-free alignment in the BP crystal is observed within the entire patterned area. Additionally, an intensity modulation in the reflectivity is observed, which is attributed to the modulation of the Bragg reflected optical phase. Thus, the period of modulation in the reflectivity is consistent with the grating period, which is measured as 690 nm. This value is slightly different with the theoretical period of 713 nm because the rotation angle of the sandwiched cell was mismatched with the design by approximately 0.5°. Figure 3.21 (b) shows the transmission spectrum of the BP for normal incidence of LCP and RCP light. Because of the helical structure of the BP II, only LCP light is reflected by the device, and RCP light is totally transmitted. The λ_c appears at 465 nm, giving a lattice constant of the device as 154 nm. Thus, the slant angle of the fabricated device is obtained as 12.9° according to Eq. (3.6).

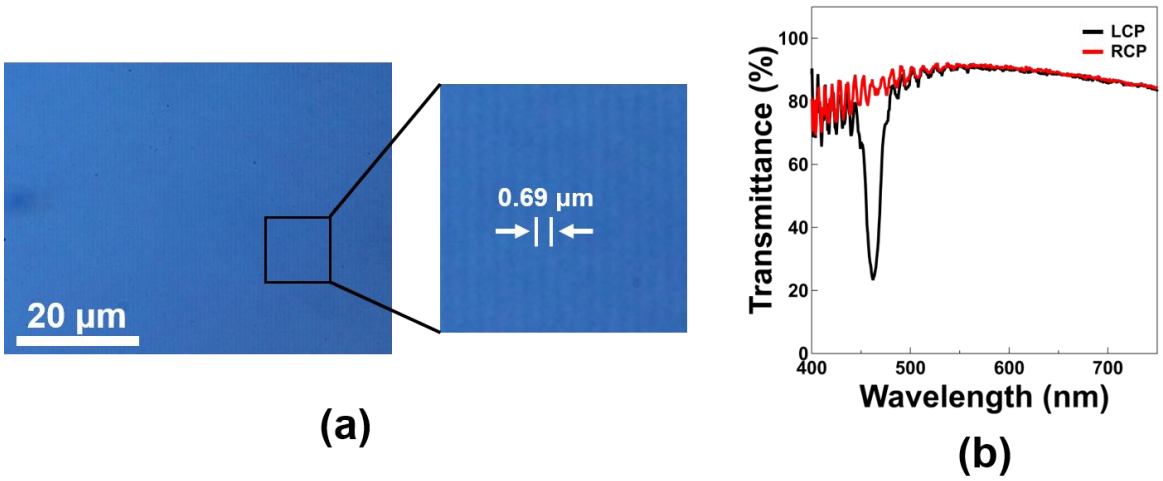


Figure 3.21 (a) POM image of the slanted BP, and its magnified image. (b) Transmission spectrum for normal incidence by LCP and RCP lights.

Kossel diagram is a diffraction pattern obtained by illuminating a converging monochromatic light on the BP crystals, providing information of bulk BP crystals such as its symmetry and orientation. The light satisfying the Bragg reflection condition forms a circular diffraction pattern, but is observed as shapes of circles, ellipses, and linear lines at a back focal plane depending on the orientation of the plane set. Despite the various shapes of the Kossel lines, the center of the diffraction pattern from a plane set of BPs represents the normal vector direction of the plane set. Figure 3.22 shows the observed and simulated Kossel diagram patterns of the device. For the simulation, BP $II_{(100)}$ with physical parameters of a = 154 nm was assumed to be slanted at an angle of 12.9°, and illuminated by a monochromatic light with a wavelength of 460 nm through an × 100 objective with a numerical aperture of 0.85. The observed Kossel diagram shows a circular pattern that is consistent with a conventional BP $II_{(100)}$, but the center of the pattern is moved to the edge of the back focal plane. The shift angle of the Kossel pattern is evaluated as 19.4° at the back focal plane, which is well-matched with that obtained through the simulation shown in Fig. 3.22 (b). Because the circular Kossel pattern is attributed from a (100) crystal plane set of BP II, the result implies that the normal vector of the (110) crystal plane set ([100] crystal axis) is tilted from the device normal.

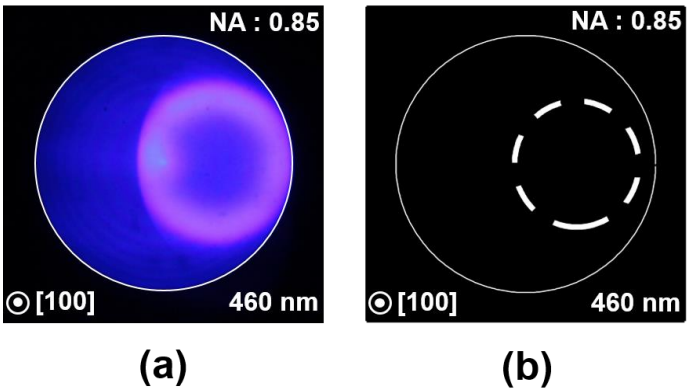


Figure 3.22 (a) Observed and (b) simulated Kossel diagrams of the proposed device. The white circles indicate the maximum collection angle of the objective.

3.4.3 Electro-optic response of slanted BP II

In this section, a possible mechanism for the structural modulation of the proposed device upon application of an electric field is described. The investigation was performed by analyzing the POM images, Kossel diagrams, and transmission spectra of the proposed device as the electric field is gradually increased at a rate of 0.19 V/μm per min. As shown in Fig. 3.23, a periodic modulation in the reflectivity is observed with the red-shifted reflection color in the POM image until the field is increased to 2.1 V/μm. In Kossel diagram, the circular pattern does not shift, but is enlarged as the field is increased. It implies that the lattice structure is elongated along the applied field, but still tilted from the device normal. The intensity modulation in POM image disappears at a field of 3.0 V/μm, and the circular Kossel pattern is shifted to the center of the back focal plane. In general, it is well-known that the BP II phase-transited to body-centered tetragonal BP X upon electric field. However, the Kossel pattern still shows a circular line, indicating a uniformly aligned BP II with its [110] crystal axis oriented along the device normal. This implies that an anchoring breaking of which the crystal orientation does not follow the imprinted orientational easy axis occurs in this field. When the electric field is further increased to 5.3 V/μm, a phase transition to the H phase with the dark POM image is observed.

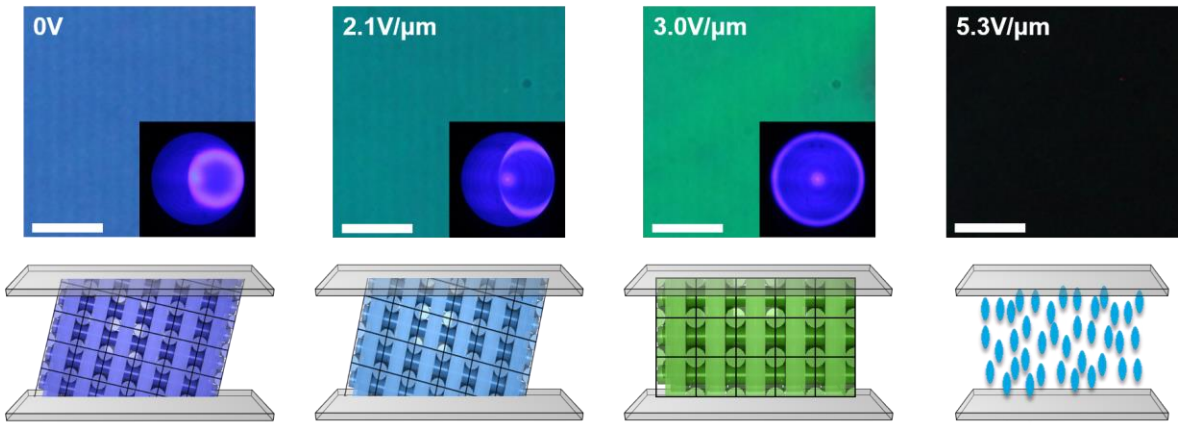


Figure 3.23 Field-dependent POM images, Kossel diagrams, and schematics of the device. The electric field is increased at a rate of 0.19 V/μm per min.

The modulation of the lattice structure is also investigated as the electric field is decreased from the H phase. When the electric field is gradually removed at a rate of 0.19 V/μm, the BP II starts to appear at 3.0 V/μm with its [100] crystal axis along the device normal. The Kossel diagrams indicate that the lattice structure shrinks continuously as the field intensity is decreased, but Kossel patterns do not shift to the initial state (Fig. 3.24 (a)). By contrast, a BP II obtained by immediately removing the electric field from the H phase shows that the original structure with a shifted Kossel pattern reappears. This result indicates that the direction of the [001] can be switched by appropriately adjusting the electric field.

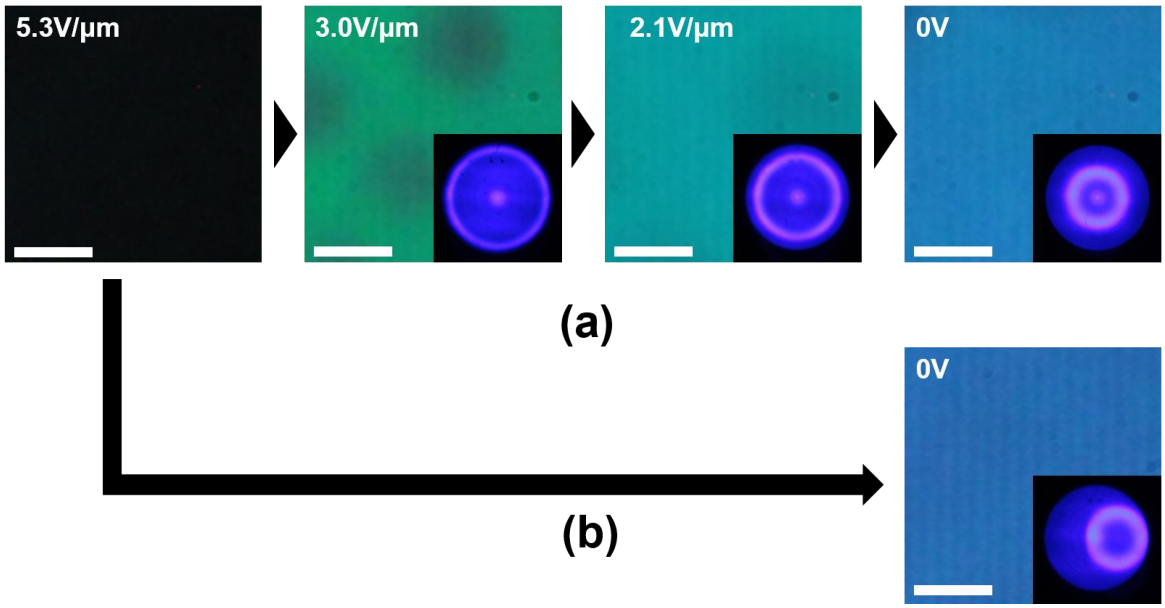


Figure 3.24 Field-dependent POM images and Kossel diagrams as the applied field is (a) gradually reduced at a rate of 0.19 V/μm and (b) directly removed from the H phase.

Figure 3.25 (a) shows the field-dependence on the λ_c of the device when the field intensity increases and decreases at a rate of 0.19 V/μm per min. For the forward process, λ_c increases gradually as the field is increased, but a discontinuous change is observed at 2.3 V/μm. This is due to the anchoring breaking of the lattice structure, as discussed in Fig. 3.23. On the other hand, λ_c decreases monotonically when the field intensity is gradually reduced because the lattice structure does not return to the initial tilted structure, as observed in Fig. 3.24. Thus, λ_c at 0 V for backward processes differs by a factor of 1/cos(α) compared to the initial BP II. Figure 3.25 (b) shows the transmission spectra of the device before and after application, and after removing the electric field. Because BP II obtained directly from the H phase has a slanted [001] axis, the transmission spectrum also appears at the same wavelength as the initial BP II. These investigations support the observation of the POM images and Kossel diagrams above.

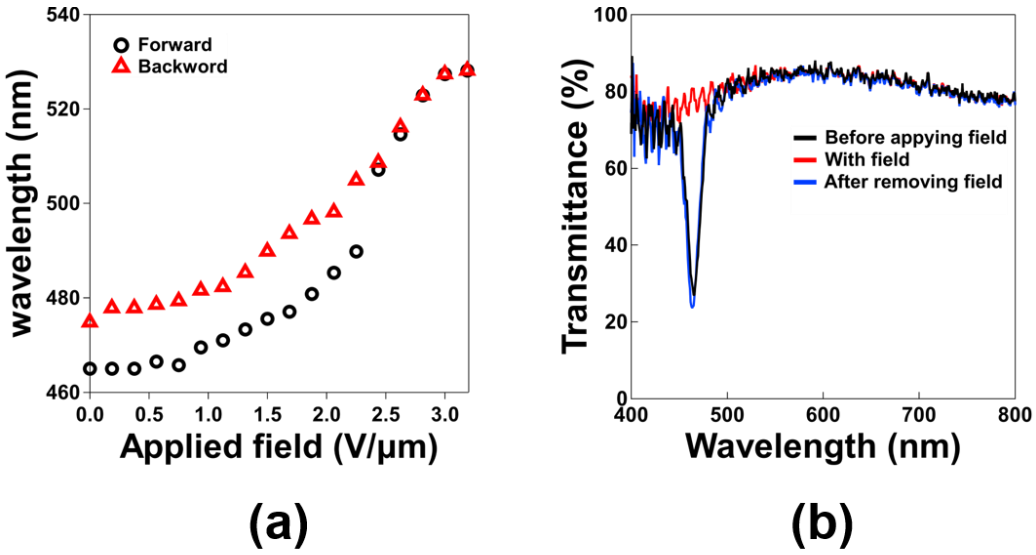


Figure 3.25 (a) Field-dependent Bragg reflection properties of the proposed device measured λ_c with respect to the field intensity, and (b) Transmission spectrum of the device before and after applying the electric field

3.4.4 Switchable deflection behavior from the proposed device

In this section, the deflection light characteristics from the proposed device are investigated. Moreover, the ability to switch the deflection by appropriately controlling the electric field is demonstrated. Figure 3.26 shows the laser setup used to observe the deflection light spot from the device. The super-continuum laser was used as a light source. The laser was divided by a prism. The wavelengths of the two beam was selected by passing through two different band-

pass filters (the central wavelengths of the filters are 460 and 480 nm, respectively, with a bandwidth of 10 nm for both). The two beams are illuminated on the device along the device normal after passing through a polarizer and a quarter-wave plate to control its polarization. The reflected light from the device is observed at a white screen placed at a distance of 13 cm from the device. The intensity of the reflected light was measured using an optical power meter (NOVA II, VEGA).

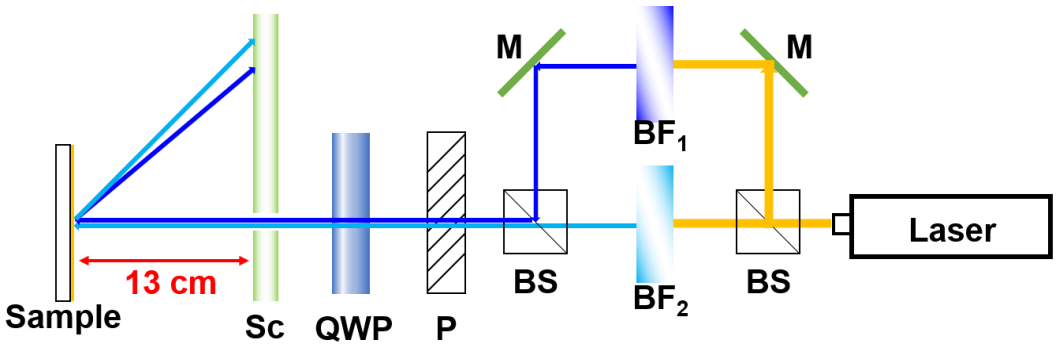


Figure 3.26 A laser setup for the observation of deflection spots from the device. BS: beam splitters; BF: band-pass filters with central wavelength of 460 (BF_1) and 480 nm (BF_2); P: polarizer; QWP: quarter-wave plate; Sc: screen; M: dielectric mirrors.

Figure 3.27 shows the reflected light spot from the device upon LCP and RCP illumination at 0 V. For this experiment, only a light with a wavelength of 460 (± 5) nm was illuminated on the device. Due to the helical structure of the BPs, only LCP light is diffracted and observed at a distance of 11.6 cm from the zero-order spot. The deflection angle is evaluated as 41.7°, which is in agreement with the theoretical value of 41.9° obtained from Eq. (3.6). The conversion efficiency is defined as the intensity ratio of reflected light with respect to the incident light, and is measured as 54.7%. For RCP illumination, by contrast, the incident light is transmitted through the device, and any diffraction spot is not observed on a screen. The ***R*** of the diffracted light was approximately 103:1.

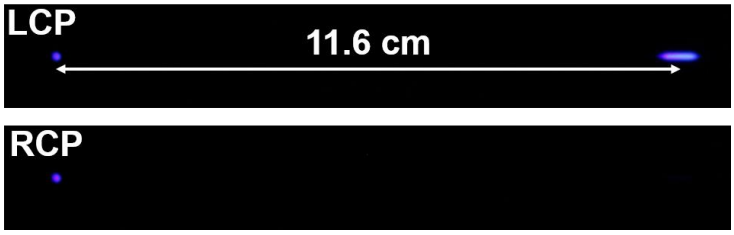


Figure 3.27 Reflected light spots for LCP and RCP illumination observed on a screen placed at a distance of 13 cm from the device.

The diffracted light spot was also observed by varying the intensity of applied field. Figure 3.28 (a) is the diffraction spot when the field is increased from 0 V to 2.1 V/μm. Under this observation, LCP light with a wavelength of both 460 and 480 nm (± 5 nm for both) was incident on the device, which correspond to the wavelength falling in the Bragg reflection spectrum of the device at 0 V and 2.1 V/μm, respectively. When the field turns on, the reflection color is changed, and hence the deflection spot is moved away from the zero-order spot according to Eq. (3.6). In addition, the deflection spot can be switched by inducing a phase transition to the H phase, as shown in Fig. 3.28 (b). These results show the capability to tune and switch the diffracted light by modulating the electric field intensity.

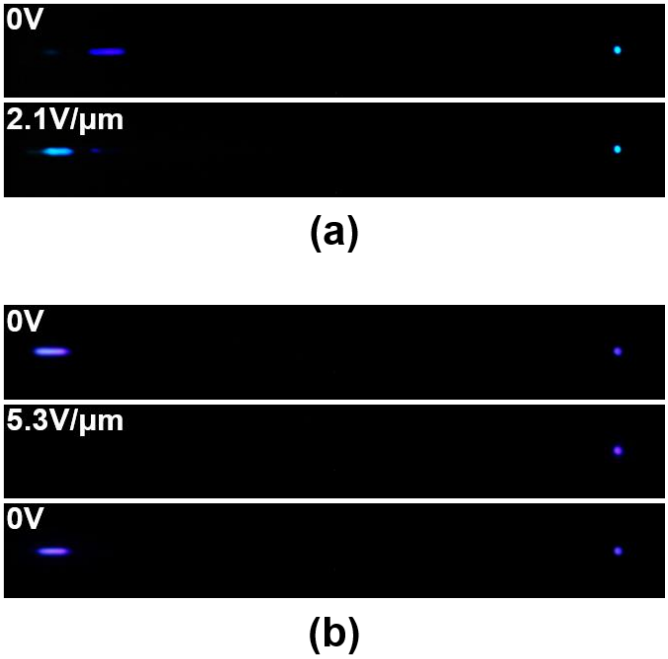


Figure 3.28 Observed diffraction spots at various field intensity. (a) Diffraction spots as the field is increased from 0 V to 2.1 V/μm. The wavelengths of incident light are 460 and 480 nm (± 5 nm). (b) Diffraction spots as a field sequence of 0 V – 5.3 V/μm – 0 V. The wavelength of incident light is 460 (± 5) nm.

3.5 Discussion

The omnidirectional CP-selective hologram shows conversion efficiencies of 54% for all angles of incidence. This efficiency is significantly higher than those of binary amplitude holograms that were fabricated by spatially modulating the intensity of Bragg reflection through control of only the crystal plane orientation [97, 98]. The main loss in the conversion efficiency

is due to the low reflectance of 62%. Thus, it is expected that the conversion efficiency can be improved by simply employing a thick sandwiched device for a higher reflection intensity.

Several questions remain to be investigated in this study. For example, it is necessary to investigate how LC molecules are aligned between two adjacent pixels with different orientation easy axes because the cubic structure cannot be continuous at different azimuthal angles. Therefore, a study of the LC orientation is expected to provide a more efficient way to control the optical phase. In addition, an important factor for CGHs is the resolution in the patterning of the BP crystals on the substrate. For pixelated holograms, the efficiency and quality of the holograms increase when the pixel size is reduced. However, it is expected that the patterning resolution cannot be decreased to a level as small as ChLCs or NLCs because of the cubic structures. Although an investigation into the resolution was not conducted due to the limited resolution of our maskless photo-patterning system, it has to be examined to investigate the minimum resolution of the BP alignment required along with an understanding of how they can be improved.

3.6 Conclusion

In this chapter, a facile and robust method to simultaneously control two crystal axes of the BP I was proposed through the field-reorientation process. It was determined that the field-induced intermediate phases, N* and BP X, are responsible for the [001] crystal axis aligned along the surface anchoring and [110] crystal axis oriented perpendicular to the substrate, respectively. This process enables to uniquely define the crystal orientation in a 3D space, enabling a number of optical applications with tailored optical properties. In addition the omnidirectional CP selectivity was theoretically described by directly solving the Maxwell's equation for light propagating in BP $I_{(110)}$, and was experimentally demonstrated by measuring the angular dependent Bragg reflection spectrum of the field-reoriented BP $I_{(110)}$. Based on the findings, an omnidirectional CP-selective hologram was fabricated by spatially pattering the azimuthal orientation of the BPs on a substrate.

A large-angle (41.7°), defect-free, and reflective deflector was also demonstrated by introducing a periodic modulation in the LC director of a simple cubic BP II on a substrate through a photo-alignment. A possible lattice orientation in which a [100] axis of simple cubic BP II is tilted from the device normal was suggested by investigating the Kossel patterns and transmission spectra of the proposed device. The electro-optical characteristics of the proposed device were investigated, and through such investigation, a tunable and switchable deflector was demonstrated by appropriately controlling the intensity of the applied electric field.

The theoretical and experimental results described in this chapter will be applicable to various areas such as the investigations on the fundamental optical properties depending on the 3D crystal orientation and the realization of advanced photonic applications with tailored optical properties.

Chapter 4 Emission direction-controllable photonic crystal laser based on slanted cholesteric liquid crystals

4.1 Introduction

Photonic crystals (PCs) that possess the multi-dimensional periodic modulation in the dielectric tensor have been utilized in various applications due to the ability to control light. The periodic modulation of the dielectric constant gives a photonic band gap (PBG), where the propagation of electromagnetic waves within certain frequency ranges is forbidden [108, 109]. One of the intensively investigated topics is the gain enhancement observed at the photonic band-edge, where the group velocity of photons approaches zero. Thus, various compact PC band-edge lasers have been realized with engineered functionalities such as a tunable emission wavelength [110], direction-controllable emission [111], and the manipulation of emission polarization [112] and patterns [113].

Volume HOEs are one of the candidates for the PC band-edge lasers because they are made through a refractive index modulation. When the refractive index is periodically modulated in a specific direction, the volume HOEs can be used for a cavity responsible for distributed feedback when doped by gain mediums. Figure 4.1 shows the typical fabrication process of the volume HOEs for the laser device. Two LP lights illuminated on the holographic plate with an angle of θ create an interference pattern that has a sinusoidal intensity modulation. When the interfered light is exposed on a holographic plate composed of photo-reactive materials such as photo-polymers [114] and polymer-dispersed LCs [17,18], the periodic modulation in the refractive index is realized with a periodicity given by $\Lambda = \lambda/2\sin(\theta/2)$, where λ is the wavelength of the recoding beam, and θ is the angle between two beams. Thus, the volume HOEs are regarded as a 1D photonic crystal structure and used for a laser cavity when the gain medium is doped in the recoding materials [115] or coated on the substrate [114]. The wavelength of the laser emission is determined for the Bragg condition given by $\lambda_{emission} = 2n_{eff}\Lambda/m$, where n_{eff} is the effective refractive index of the cavity, and m is the Bragg order. Because of the narrow emission bandwidth and their capability of mass-production, they are widely used for organic semiconductor lasers. Various wavelength-tunable lasers have been proposed [116], but it remains a challenge to control the emission direction because the cavity is always created in a direction along the grating vector.

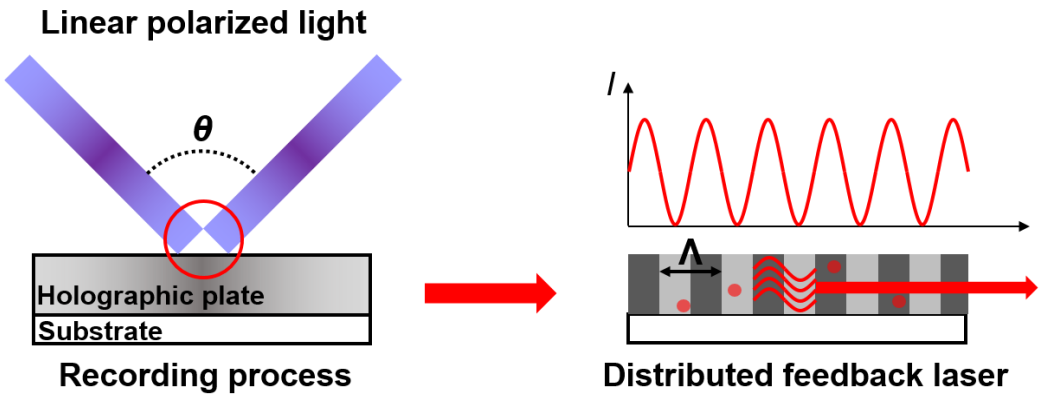


Figure 4.1 Fabrication process of the volume holograms for DFL. The two LP lights create an interference pattern in which the intensity is periodically modulated with periodicity of Λ. The interference pattern induces the periodic modulation in the refractive index of the holographic plate. The red dots indicate a doped gain medium.

ChLCs self-organize into a periodic modulation in the refractive index along the helical axis, providing a cavity for lasing oscillation through a distributed feedback at the edge of the Bragg reflection band when doped by a gain medium such as laser dyes [46, 117] and quantum dots [118, 119]. An easy fabrication owing to the self-assembled structures and a low threshold energy make the ChLCs attractive for PC laser applications. In particular, the external stimuli-responsivity of the LCs enables a number of PC lasers with a tunable emission wavelength by modulating either the refractive indices and helical pitch through temperature control [47, 120], application of an electric field [46], and the illumination of light [121]. In addition, flexible free-standing film-type PC lasers have been proposed using photo-polymerizable ChLCs [45, 122]. In ChLC-based PC lasers, the cavity modes are always formed along the helical axis, resulting in the emission direction to be either parallel (for planar aligned ChLC) [46, 48] or perpendicular (for uniformly lying helical structure) [123, 124] to the device normal. Recently, lasers with an omnidirectional [125] and cone-shaped [126, 127] emission have been demonstrated, but it remains a challenge to control the emission direction.

In this chapter, an emission direction-controllable PC band-edge laser is demonstrated based on a slanted ChLC. In a conventional ChLC where the helical axis is uniformly aligned in a direction perpendicular to a substrate, an additional short-pitch periodic modulation in the LC director is introduced in a direction perpendicular to the helical axis. The additional periodicity causes the cavity for the laser oscillation to be slanted from the device normal, resulting in the emission to be tilted at an angle of ~ 30° from the device normal. The theoretical analysis also

shows that the emission angle can be tuned by manipulating the periodicity, which is experimentally demonstrated by modulating the helical pitch through the control of temperature.

4.2 Device design and its photonic band structure

First, I theoretically investigate the photonic band structures of a conventional ChLC and the ChLC proposed in this chapter to analyze how the additional modulation of the LC director in a direction perpendicular to the helical axis affects the lasing cavity. Figure 4.2 shows schematic representations of a dye-doped conventional ChLC and the ChLC proposed in this chapter. The conventional ChLC has a uniform alignment in the LC director on a substrate, and shows its helical axis aligned in a direction perpendicular to the substrate, pointed by the Γ–X direction, as shown in Fig. 4.2 (a). The helical pitch p is defined as a distance where the LC director rotates 2π radians. Figures 4.2 (b) and (c) show the modeled orientation of the LC director and dielectric constant (ε) distribution of the conventional ChLC, which is taken by one periodic area. Because of the head-tail symmetry of the LC director, the dielectric constant is periodically varied with a periodicity of $p/2$. In the conventional ChLC, the cavity for lasing oscillation is created along the helical axis pointed by the Γ–X direction in Fig. 4.2 (a).

The ChLC proposed in this chapter is illustrated in Fig. 4.2 (d). The proposed ChLC has the same helical pitch as a conventional ChLC, but possesses an additional in-plane periodic modulation in a direction perpendicular to the helical axis, as pointed by the Γ–P direction. The in-plane modulation of the LC director has a periodicity of Λ, which is defined as a distance in which the LC director rotates π radians. As shown in Figs. 4.2 (d) to (f), the periodicity along the Γ–P direction results in a layered structure to be slanted at an angle of α,

$$\alpha = \tan^{-1}\left(\frac{p}{2\Lambda}\right). \tag{4.1}$$

Hereafter, the proposed ChLC with a slanted layer structure is referred to as the slanted ChLC. As a result, the dielectric tensor distribution also shows periodicity in a direction perpendicular to the slanted structure, as shown in Fig. 4.2 (f). It is thus expected that the cavity for lasing oscillation based on a distributed feedback becomes off-axis from the helical axis, which will be explained below through an analysis of the photonic band structures.

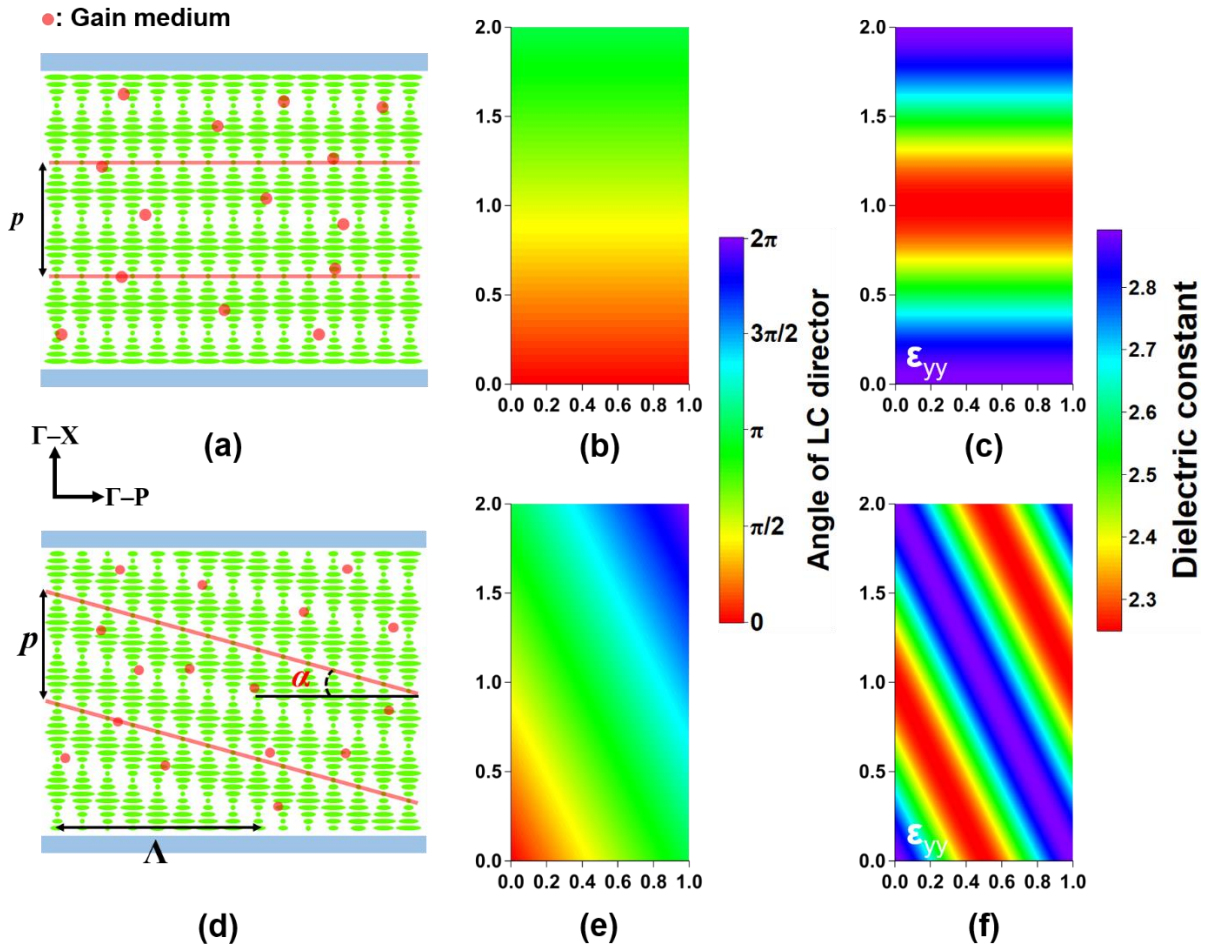


Figure 4.2 Design of conventional and slanted ChLCs. (a) Schematic of conventional ChLC. (b, c) Modeled (b) orientation of LC director and (c) ε_{yy} component of dielectric tensor distribution of conventional ChLC. (d) Schematic of slanted ChLC. (e, f) Modeled (e) orientation of LC director and (f) ε_{yy} component of dielectric tensor distribution of slanted ChLC. In (b) and (e), the angle of LC director is defined as the angle between the long axis of the LC molecule with respect to the Γ–P direction. The angle of the LC director is defined as an angle between the long-axis of LC molecules and the Γ–P direction.

Figure 4.3 shows the photonic band structures of the conventional ChLC and the slanted ChLCs with an in-plane periodicity of $\Lambda = p$, giving a slant angle of 26.6°. The physical parameters of the ChLCs were modeled as $n_o = 1.5$ and $n_e = 1.7$. In the photonic band structures, the value of $\partial\boldsymbol{\omega}/\partial\boldsymbol{k}$ (the slope of the graph) indicates the group velocity of the photons, and the

photonic band-edge is observed at where $\partial\boldsymbol{\omega}/\partial\boldsymbol{k}$ value approaches zero. In the conventional ChLC, the photonic band-edge is clearly visualized at X-point indicated by a red circle, implying the cavity for laser oscillation to be created in the Γ–X direction parallel to the helical axis. The band-edges appear at $\boldsymbol{\omega}_{\mathrm{h}} = 0.5/n_{\mathrm{o}}$ and $\boldsymbol{\omega}_{\mathrm{l}} = 0.5/n_{\mathrm{e}}$, where $\boldsymbol{\omega}_{\mathrm{h}}$ and $\boldsymbol{\omega}_{\mathrm{l}}$ are high- and low-frequency edges, resulting in $\lambda_{\text{short band-edge}} = n_{\mathrm{o}}p$ and $\lambda_{\text{long band-edge}} = n_{\mathrm{e}}p$, respectively.

On the other hand, in the photonic band structure of the slanted ChLC shown in Fig. 4.3 (b), the band-edge is not observed at the X-point, but a new band-edge appears at the M-point indicated by the red circle. Thus, the cavity for a laser oscillation is no longer formed in a direction parallel to the helical axis, but is created in a direction perpendicular to the slanted structure. The frequencies are also shifted proportional to 1/cos(α) in comparison to the conventional ChLC, where at $\boldsymbol{\omega}_{\mathrm{h}} = 0.5/n_{\mathrm{o}}\cos(\alpha)$ and $\boldsymbol{\omega}_{\mathrm{l}} = 0.5/n_{\mathrm{e}}\cos(\alpha)$. Thus, the wavelengths of the band-edges can be expressed by the following:

$$\lambda_{\text{shortband–edge}} = n_{\boldsymbol{e}}\, p\cos\alpha\,, \tag{4.2}$$

$$\lambda_{\text{longband–edge}} = n_{\boldsymbol{e}}\, p\cos\alpha\,. \tag{4.3}$$

Eqs. (4.2) and (4.3) show that the emission wavelength is affected by not only the helical pitch, but also the slant angle (grating period). When the laser beam is emitted from the device into free-space, it is refracted to the interface between the device and air according to Snell's law described as follows:

$$n_{\text{air}}\sin\theta_{\text{lasing}} = n_{\text{ChLC}}\sin\alpha\,, \tag{4.4}$$

where n_{air} and n_{ChLC} are the refractive indices of air ($n_{\text{air}} = 1$) and the ChLCs. The combination of Eqs. (4.1) to (4.4) leads to a PC band-edge laser with an emission angle in free-space with respect to the device normal as

$$\theta_{\text{lasing}} = \sin^{-1}\left(\frac{\lambda_{\text{lasing}}}{2\Lambda}\right), \tag{4.5}$$

where θ_{lasing} and λ_{lasing} are the emission angle and wavelength, respectively. Eq. (4.5) shows that the emission direction can be controlled by modulating either the helical pitch or the grating period, which will be experimentally demonstrated in Section 4.4.

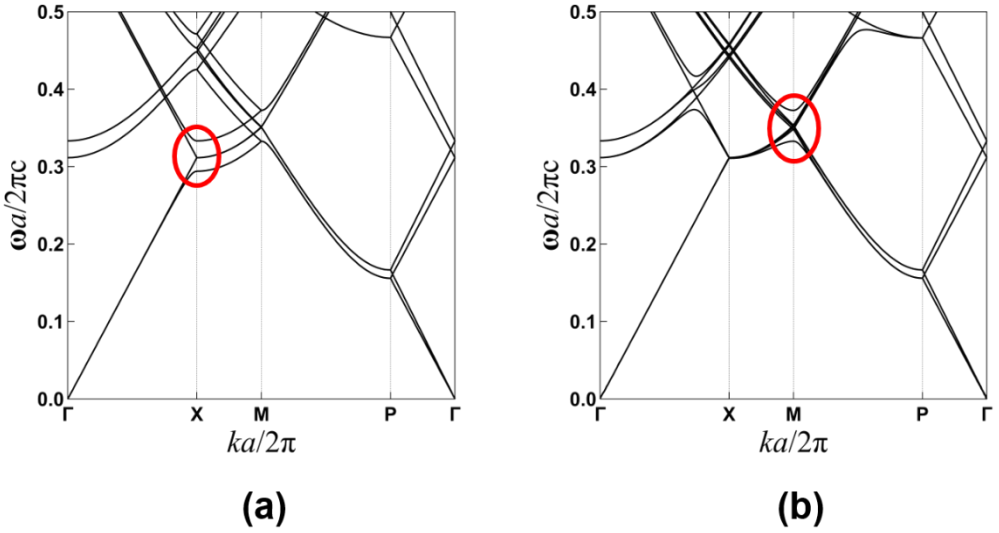


Figure 4.3 Photonic band structures of (a) conventional and (b) slanted ChLCs.

4.3 Off-axis laser emission

In Chapter 4.2, it was theoretically described that the emission-direction deviates from the helical axis by artificially introducing an additional periodicity along the Γ–P direction. There are various methods for creating a periodic modulation of the LC director along the Γ–P direction on a substrate such as maskless photo-patterning using a digital mirror device (DMD) [77] and polarization holography method [78]. In this section, a polarization holography method is employed to introduce an additional periodicity of the LC director along the Γ–P direction.

4.3.1 Device fabrication and materials

Two types of devices were prepared for the experiment: a cell-type device and a film-type device. The sandwiched cell was prepared by assembling two glass substrates covered by a photoalignment material, with a cell-gap of 9 μm. For the film-type device, a glass substrate was prepared by coating the photoalignment material. Both devices were first illuminated by LP UV light to induce a planar alignment across the whole region of the device. The devices were then photo-patterned using a polarization holography method to introduce the periodic modulation of the LC director in the Γ–P direction.

Figure 4.4 (a) shows a laser setup for polarization holography method. A sappier laser (Sapphire SF 488, Coherent) was employed as a light source. The light was converted into LCP light after passing an optical isolator (also acting as a polarizer) and a BS compensator, and enlarged to a beam size of approximately 1 cm using a beam-expander. The LCP light passed through the sample and a quarter-wave plate (QWP), was reflected by a dielectric mirror. The

reflected light passed through the same QWP again such that it impinged on the sample as LCP light. The samples were placed in the optical path between the BS compensator and the QWP. Two counter-propagating LCP lights were superimposed, creating an interference pattern such that the angle of LP light was continuously rotated along the direction perpendicular to the two beams [78]. When the sample is rotated to an angle of θ with respect to the direction perpendicular to the light propagation, the periodicity (Λ) of the rotatable LP light is given by $\Lambda = \lambda/2\sin\theta$, where λ is the wavelength of the laser light (488 nm) as shown in Fig. 4.4 (b). In experiment, the sample was rotated with an angle of 23°, giving a theoretical grating period of ~620 nm. The light with an intensity of 76 mW/cm^2 was illuminated on the samples for 3 min.

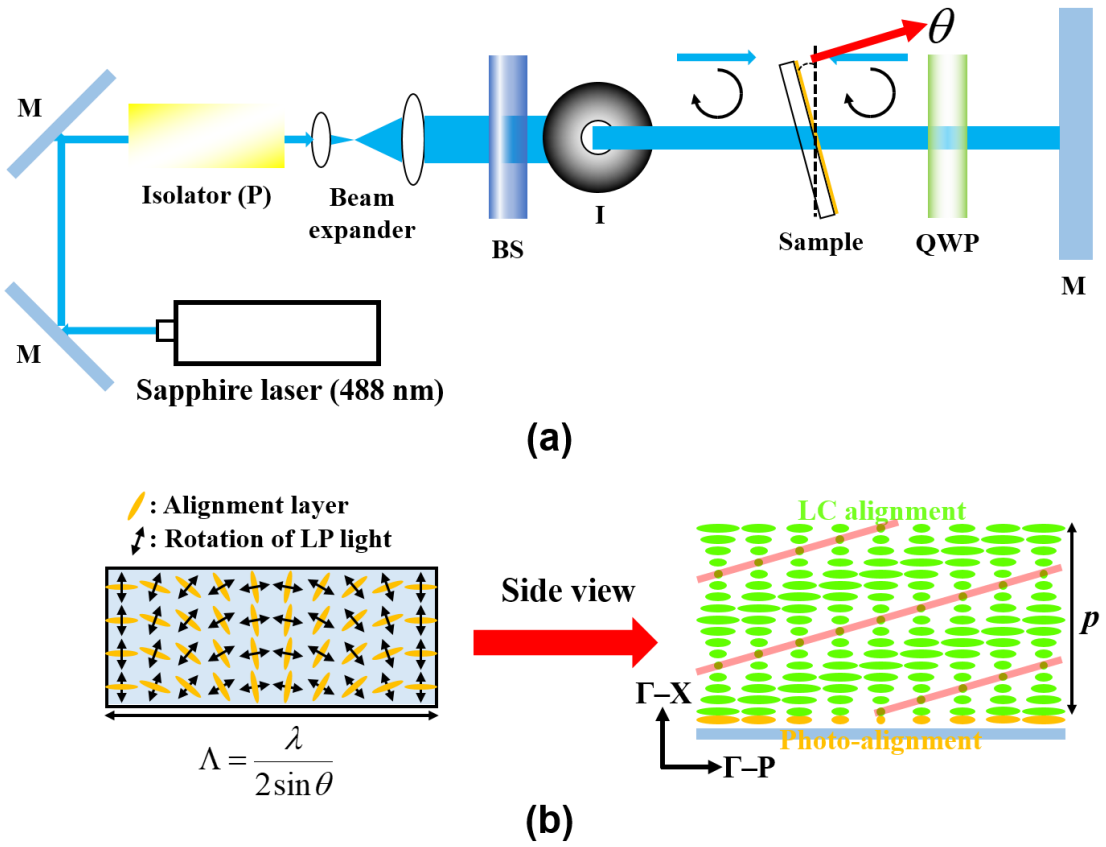


Figure 4.4 Polarization holography method. (a) A schematic of the laser setup for polarization holography process. P: polarizer; BS: Babinet-Soleil compensator; I: iris; QWP: quarter-wave plate; M: dielectric mirror. (b) Orientation of the LC molecules on the patterned substrate.

For the fabrication of the cell-type device, a ChLC material doped by a gain medium was prepared by blending a host nematic LC (MLC-2140, Merck), a left-handed chiral dopant (S-5011, HCCH), and a 4-(dicyanomethylene)-2-methyl-6-(4-dimethylaminostyryl)-4H-pyran

dye (DCM, Exciton) at a weight ratio of 96.5:2.5:1. The chemical structure of the dye is shown in Fig. 4.5, and the absorption and fluorescence band of the dye can be obtained from ref. 123. To homogeneously blend the materials, the mixture was dissolved in chloroform and heated at 80°C for 2h to evaporate the solvent. The ChLC mixture was injected in the photo-pattenred cell at isotropic phase (100°C) and cooled to room temperature (25°C) at a rate of 0.1°C/min.

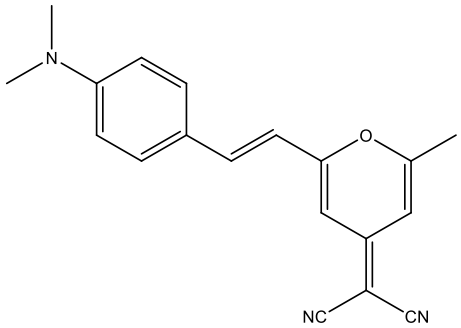


Figure 4.5 Chemical structure of the laser dye used in experiments.

For the fabrication of the film-type device, a photopolymerizable ChLC precursor was prepared by blending a photocurable reactive mesogen monomer (LC242, BASF Japan Ltd.), a mesogenic chiral monomer (LC756, BASF Japan Ltd.), a photo-initiator (IrgacureOxe04, BASF Japan Ltd.), and a surface additive (BYK-361N, BYK) at a weight ratio of 94.8:4.1:1.0:0.1. The chemical structures of the mesogen monomers are illustrated in Fig. 4.6 The precursor was dissolved in toluene at a concentration of 200 mg/ml, and filtered out using a membrane filter (pore size: 200 nm) to remove undissolved materials. The precursor was spin-coated on the patterned substrate by 2000 rpm for 30 s, and cured by UV light (λ = 365 nm, 220 mW/cm^2) for 5 min in a nitrogen environment. The coating process was carried out 7 times to make a device with a thickness of approximately 5 μm.

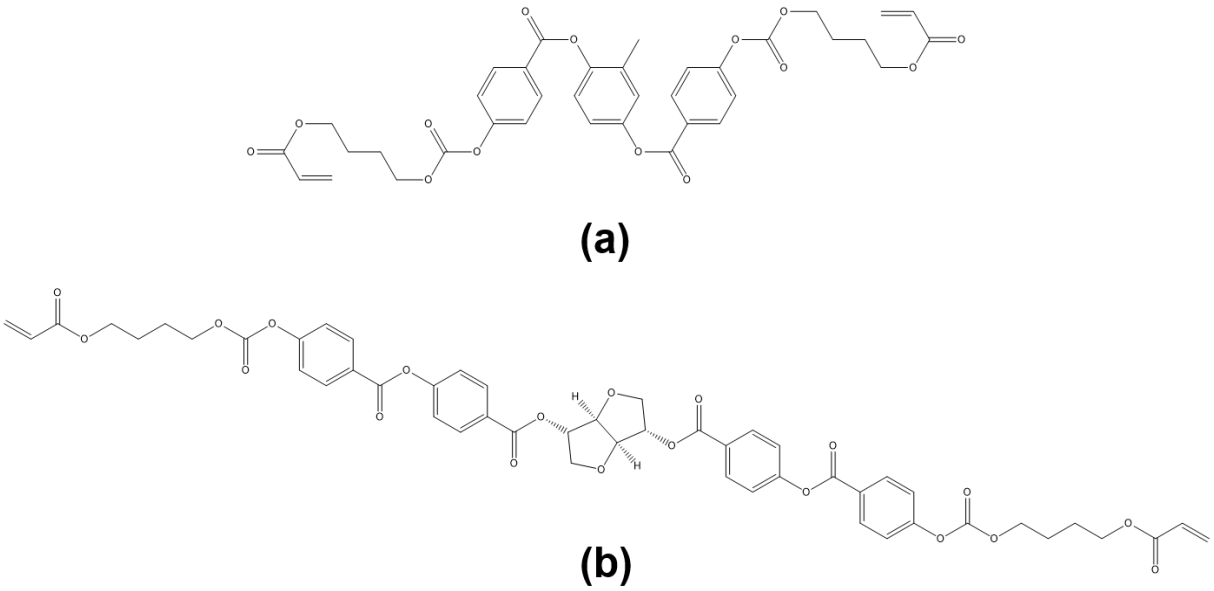


Figure 4.6 Chemical structures of the reactive mesogens: (a) LC 242 and (b) LC 756.

4.3.2 POM texture and transmission spectrum

Figure 4.7 (a) shows a POM texture of the slanted ChLC observed in reflection mode. In the magnified image, a periodic variation in the reflection intensity is observed because the periodic modulation of the LC director makes the Bragg-reflected optical phase to be continuously modulated [32]. The sinusoidal modulation in the reflection intensity with a period of ~620 nm corresponds to the grating period, which is well-matched with the design described in the previous section. Figure 4.7 (b) shows the transmission spectrum of the slanted ChLC, which is measured along the Γ–X direction. The Bragg reflection band of the slanted ChLC upon normal incidence appears at a wavelength proportional to $\cos^2(\alpha)$ as compared to the conventional ChLC [128]. The $\lambda_{\text{long band-edge}}$ of the Bragg reflection is observed at 597 nm. Through the values of Λ = 620 nm and $\lambda_{\text{long band-edge}}$ = 597 nm obtained from the experiments and the values of n_o = 1.53 and n_e = 1.75 obtained from datasheet, the helical pitch of the slanted ChLC is calculated as 373 nm, giving a slant angle of approximately 17°. Based on these values, the wavelength and angle of the laser emission from slanted ChLC can be expected through Eqs. (4.3) and (4.5) as 625 nm and 30.3°, respectively.

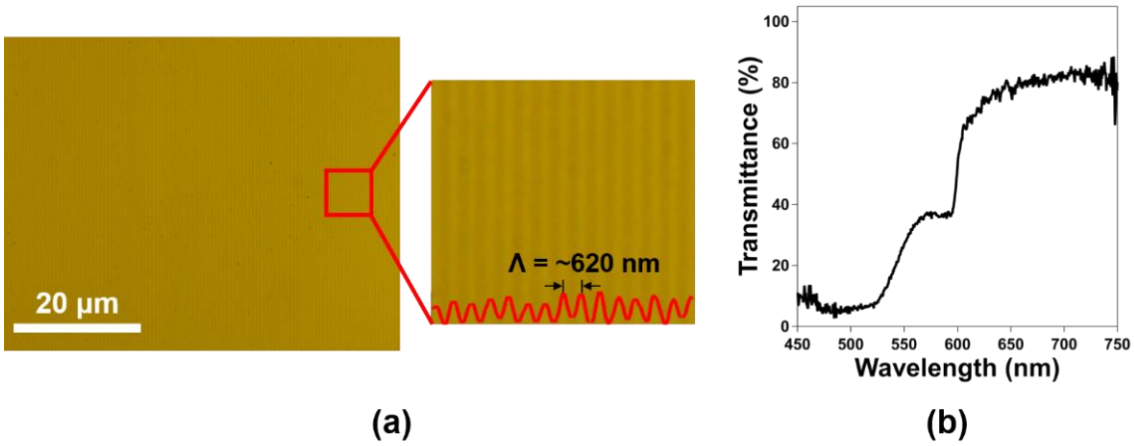


Figure 4.7 A fabricated ChLC with slanted structure. (a) POM image taken in reflection mode and its magnified image. (b) Transmission spectrum measured in the Γ–X direction.

4.3.3 Transmission electron microscope images

A cross-sectional TEM observation is a powerful tool to observe the layer structure of the ChLCs because as it can directly confirm the periodic structure through alternating dark and light lines originated from the LC director aligned parallel and perpendicular to the film surface, respectively [129]. For the observation of TEM images, the film-type ChLCs (both conventional and slanted ChLC) was separated from the glass substrate, embedded in an epoxy resin (Quetol 812, NisshinEM) and cured at 40°C for 3 days. The ultrathin cross-section films with a thickness of 80 nm were obtained through an ultramicrotome (EM UC7, LEICA), and deposited on the mesh grids with a size of 150 μm. A TEM observation was conducted with an accelerating voltage of 100 kV.

Figure 4.8 shows the cross-sectional TEM images of the conventional and slanted ChLCs. In the conventional ChLC, alternating bright and dark lines are observed parallel to the substrate, indicating that the helical axis is along the device normal. The distance between two bright lines (dark lines) along the Γ–X direction shows half of the helical pitch because the LC direction has a head-tail symmetry. On the other hand, in the slanted ChLC, it can clearly be seen that the lines are tilted from the substrate, corresponding to the slanted layer structure, as shown in Fig. 4.2 (d). The distance between two bright lines (dark lines) along the Γ–P direction indicates the grating period of the slanted ChLC. Through the TEM images, it is confirmed that the periodic structure responsible for a laser cavity is tilted from the device normal. In addition, the alignment of the LC molecules in the depth-direction is achieved on the substrate although the coating process was carried out several times on a alignment layer having a thickness of a few 10 nm.

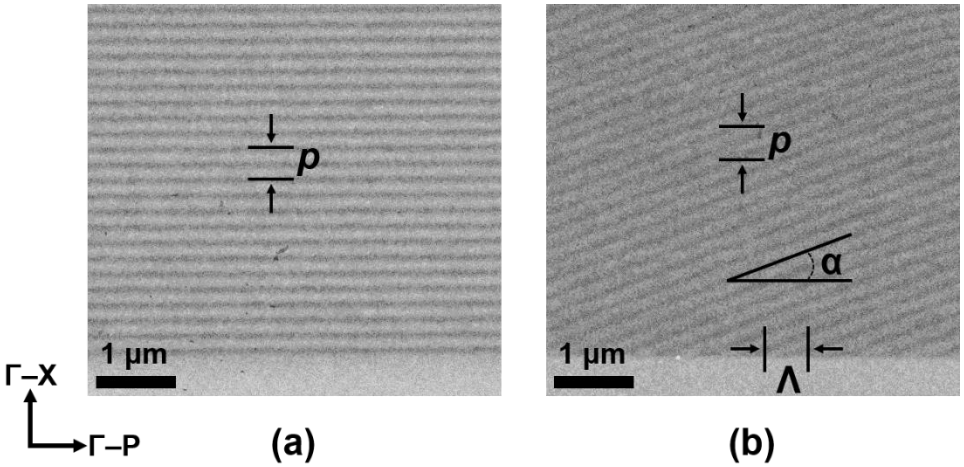


Figure 4.8 Cross-sectional TEM images for (a) conventional and (b) slanted ChLCs.

4.3.4 Laser emission characteristics

Figure 4.9 shows a laser setup to observe the laser emission from the slanted ChLC. A second-harmonic of a Q-switched DPSS YAG laser (λ = 532 nm, pulse repetition = 10 Hz, and pulse width = 10 ns) was used as an incident light source to pump the laser dye. The intensity and polarization of the laser were controlled by placing neutral density (ND) filters, a HWP, a polarizer, and a QWP in the optical path. The laser was focused on the device through a lens with focal length of 3 cm. The laser emission from the device was projected onto a screen placed at a distance of 10 cm from the sample, or collected by an optical fiber connected to a spectrometer (Hamamatsu, PMA-11).

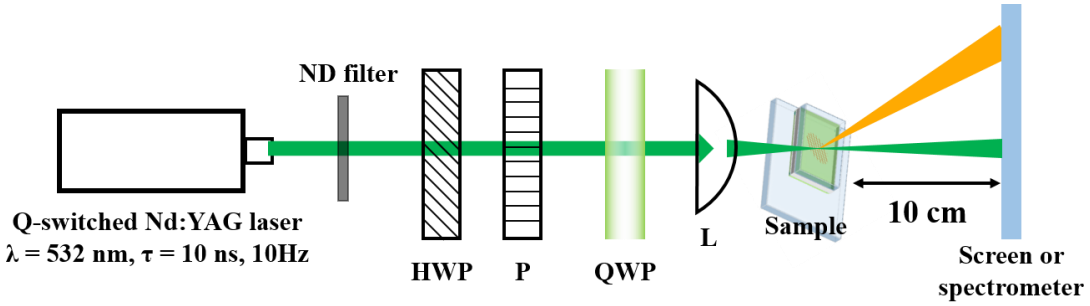


Figure 4.9 A schematic of the experimental laser setup for observation of laser emission from slanted ChLC. HWP: half-wave plate; P: polarizer; QWP: quarter-wave plate; L: focusing lens with focal length of 3 cm.

Figure 4.10 shows a photograph of the emission from the slanted ChLC, observed on the screen. A red laser emission from the slanted ChLC is projected at a distance of 5.8 cm from

the zero-order light (incident green laser). The emission angle is evaluated as 30° from the device normal, which is in agreement with the theory predicted by Eq. (4.5). Figure 4.11 shows the laser emission characteristics of the conventional and slanted ChLCs. In the conventional ChLC, the wavelength of the laser emission is observed at a wavelength of 614 nm, which corresponds to the long band-edge wavelength of the transmission spectrum, as shown in Fig. 4.11 (a). This is a common phenomenon of ChLC-based PC band-edge lasers. By contrast, the emission wavelength of the slanted ChLC (observed at 624 nm) is inconsistent with the edge of the transmission spectrum (observed at 597 nm), as shown in Fig. 4.11 (b). This is because the cavity for a lasing oscillation (along Γ–M direction) and Bragg reflection (along Γ–X direction) appears at a wavelength proportional to $\cos(\alpha)$ and $\cos^2(\alpha)$ when compared to the conventional ChLC, respectively. Therefore, the emission is observed at a wavelength larger than the long-band edge by a value of $1/\cos(\alpha)$. The experimentally obtained values are well-matched with the theoretical values expected in Section 4.3.2. Because of the helical structure of the ChLC, the emission is circular-polarized, as shown in Fig. 4.11 (c), which is the advantages of the proposed device. Because the slanted ChLC possesses a left-handed helix, the device emits only LCP light. The intensity ratio of LCP and RCP components is measured as 96:1. The threshold energy for the laser emission was obtained by measuring the peak intensity of the laser emission spectrum at various pumping energies, which is 8.1 mJ/cm^2 per pulse, as shown in Fig. 4.11 (d). A slightly higher threshold energy is obtained from the slanted ChLC that the conventional ChLC (5.5 mJ/cm^2 per pulse); however, this is because the fluorescence efficiency of the DCM dye is higher at wavelength of 614 nm than 624 nm.

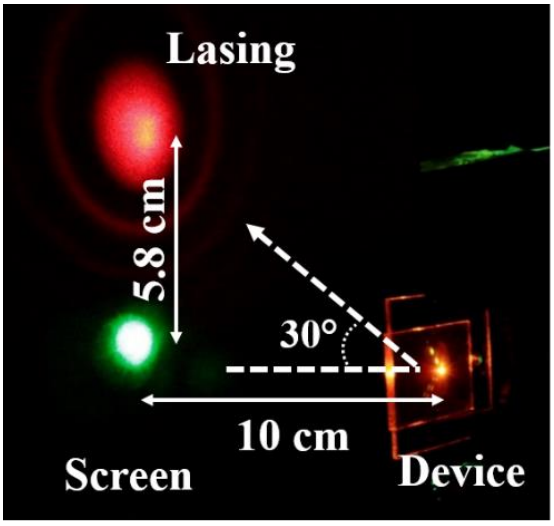


Figure 4.10 Photograph of the emission spot observed on a screen placed at a distance of 10 cm from slanted ChLC.

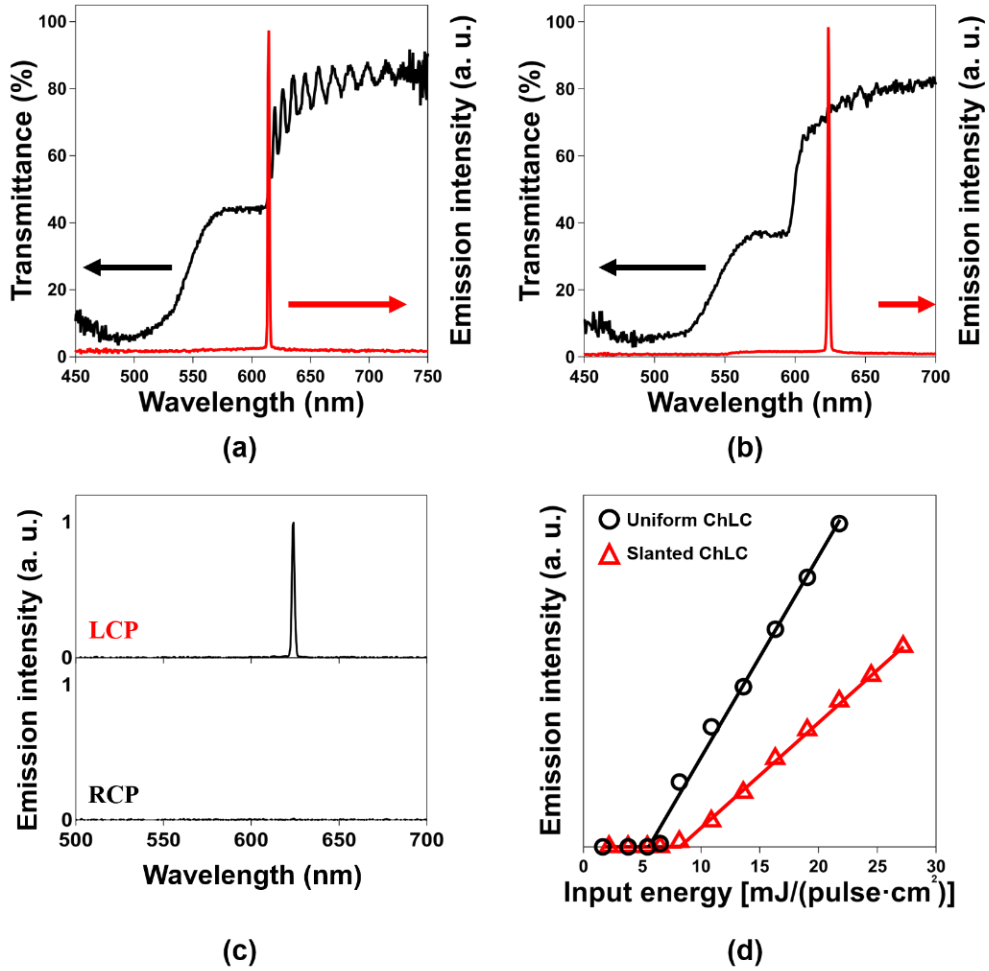


Figure 4.11 Laser emission characteristics of conventional and slanted ChLCs. (a) Laser emission and transmission spectrum of the conventional ChLC. Both are measured in the Γ–X direction. (b) Laser emission of the slanted ChLC measured in the Γ–M direction with transmission spectrum measured in the Γ–X direction. (c) The LCP and RCP components of the laser emission from the slanted ChLC. (d) Typical threshold energy of the two devices.

4.4 Emission-direction tuning through external stimuli

Eq. (4.5) reveals that the emission angle can be modulated by controlling either the helical pitch or grating period. Various tunable PC band-edge lasers have been proposed by modulating the helical pitch through external stimuli [46, 120, 121]; however, the devices are limited in controlling the emission wavelength. In this section, an emission direction-controllable PC laser is demonstrated by tuning the helical pitch of the slanted ChLC through varying the temperature.

4.4.1 Materials

To prepare a largely tunable device, a chiral dopant-saturated ChLC [47] was prepared by blending a host nematic LC mixture (BL-006, Merck), a chiral dopant (S-811, HCCH), and the laser dye at a weight concentration of 66:33:1. The material enables to tune the band-edge wavelengths of the slanted ChLC from the UV region to the IR region by controlling the temperature.

4.4.2 Laser emission characteristics

The laser emission was characterized using a laser setup coupled to a home-made optical microscope, as shown in Fig. 4.12. The incident laser is connected to a microscope through an optical fiber and a × 20 objective after controlling the intensity through ND filters, a HWP, and a polarizer (P_1). The polarization of incident laser was controlled by another polarizer (P_2) and a QWP. The incident laser was divided through a 50:50 beam splitter; one is illuminated on an optical power meter (OPHIR, VEGA) and the other is focused on the device through a × 50 objective with a numerical aperture of 0.55. The size of the focused beam size has a diameter of ~3.5 μm on the sample. The emission spectrum from the device was collected by an optical fiber (diameter: 1 mm) connected to a spectrometer (Hamamatsu, PMA-11). The lasing spot at the back focal plane of the objective was obtained by inserting a focusing lens (f = 175 mm) in the optical path, and was captured by an image sensor (IDS, UI-3370CP-C-HQ Rev.2). The transmission spectrum in the Γ–X direction was measured by illuminating a white light (MORITEX, MHAA-100W). The temperature of the sample was controlled by a commercial thermal controller (TS350, Rinkam), at a rate of 0.1°C/min. Both the conventional and slanted ChLCs are used to measure the lasing properties for comparison.

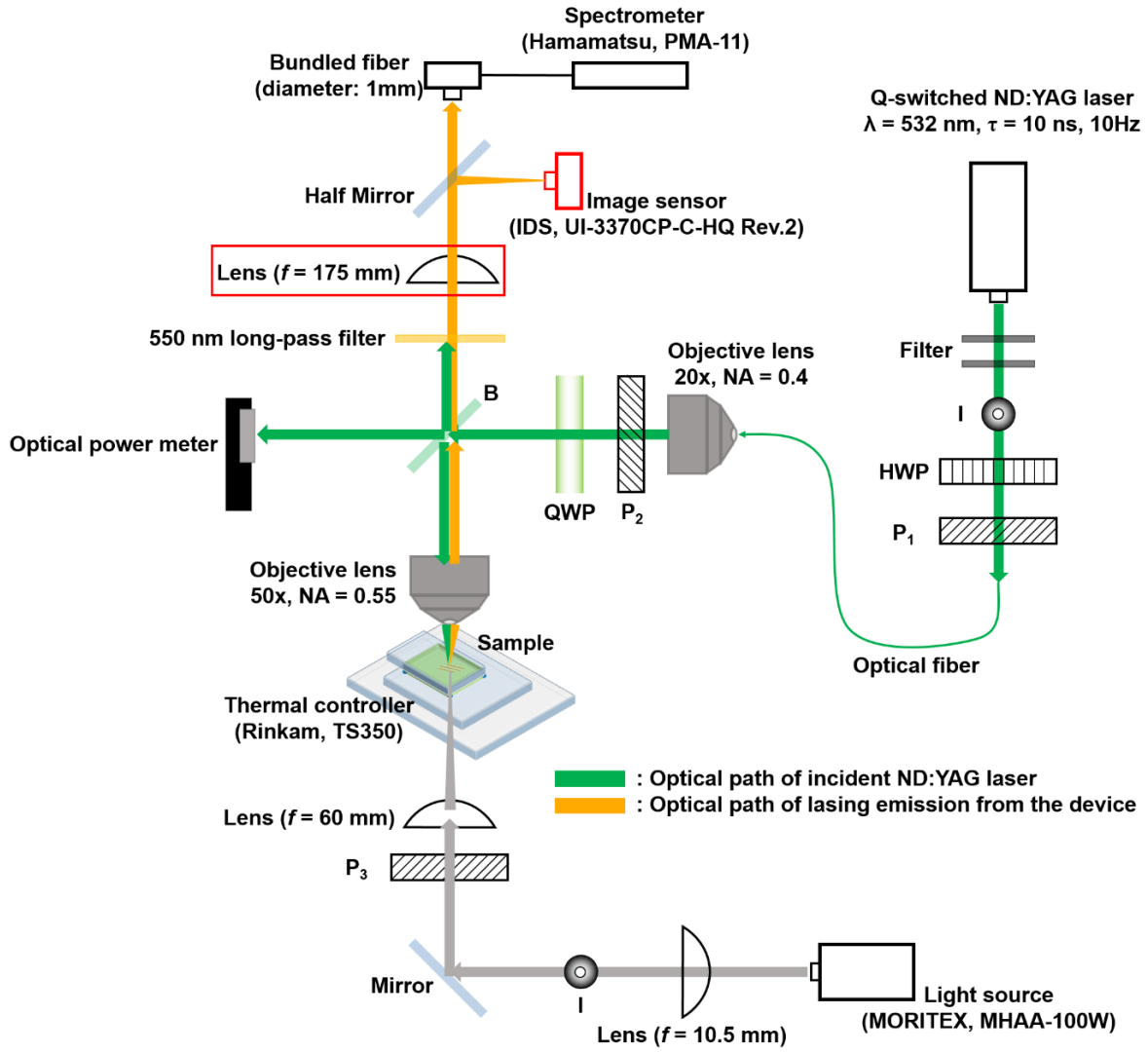


Figure 4.12 A schematic of optical setup to characterize the laser emission from tunable device. HWP: half-wave plate; QWP: quarter-wave plate; P: polarizer; I: iris; B: 50/50 beam splitter. The lens (*f* = 175 mm) in the red square was only used to observe the emission spot in the back focal plane of the objective.

Figure 4.13 shows the temperature-dependent emission wavelength from the conventional and slanted ChLCs. The solubility of the doped chiral dopant is increased as the temperature is increased, causing the helical pitch to be shortened. Thus, the wavelength of the laser emission blue-shifts by increasing the temperature in both ChLCs. The emission wavelength shifts from 657 nm at 31.4°C to 570 nm at 35.2° for the conventional ChLC, and from 655 nm at 28.5°C to 570 nm at 32.9°C for the slanted ChLC, which cover the entire fluorescence band of the doped gain medium. The tuning of the emission wavelength is discontinuous in both devices

because the helical structure allows only a half-integer pitch owing to the surface anchoring in the sandwiched cell [120].

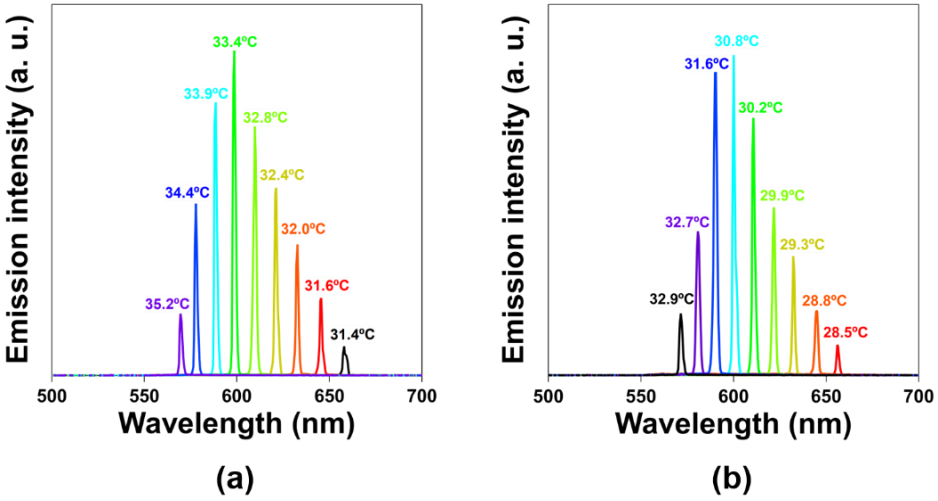
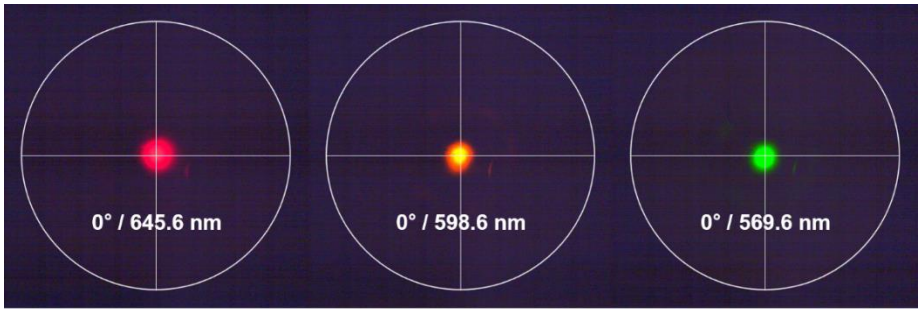
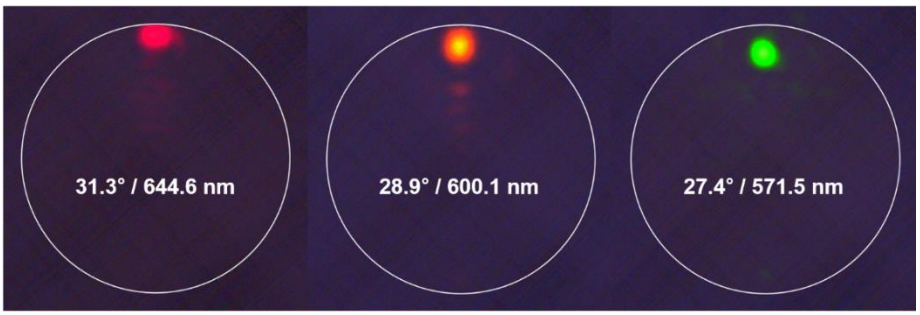


Figure 4.13 Laser emission wavelength of (a) conventional and (b) slanted ChLCs.

Figure 4.14 shows the emission beam spots from the conventional and slanted ChLCs observed at the back focal plane of the objective. The white circles indicate the maximum collection angle of the objective, which is given by $\sin^{-1}(NA) = 33.4°$. As shown in Fig. 4.14 (a), for conventional ChLC, the emission spots are observed at the center of the back focal plane because the emission direction is always parallel to the helical axis. On the other hand, as shown in Fig. 4.14 (b), the beam spot from the slanted ChLC with an emission wavelength of 644.6 nm is observed at the edge of the back focal plane, and shifts to the center of the back focal plane as the helical pitch shortens, demonstrating the capability to tune the emission direction from the slanted ChLC. As shown in Fig. 4.15, the emission angle is changed from 31.3° for 645 nm to 27.4° for 572 nm, showing the tunable range of approximately 4°, which is well-matched with the expected values obtained from Eq. (4.5).



(a)



(b)

Figure 4.14 Observed laser emission spots at back focal plane from (a) conventional and (b) slanted ChLCs. The white circles show the maximum collection angle through the objective with NA of 0.55 as given by the equation $\sin^{-1}(NA) = 33.4°$.

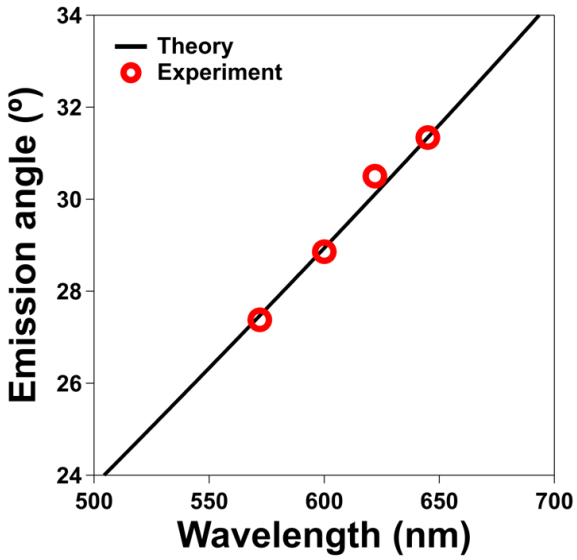


Figure 4.15 Theoretical and experimental emission angle from the slanted ChLC. The theoretical values are obtained from Eq. (4.3).

4.5 Discussion

In this chapter, the direction-controllable PC laser has been demonstrated by controlling the helical pitch through modulating temperature, but the response time is quite slow. A ChLC/nanocomposite can be a candidate as a direction-controllable laser, which enables control of the refractive index of the device by an electric field with a fast response time through the reorientation of the LC molecules in the nanopores [46]. The ChLC/nanocomposite also shows additional advantages such as a continuous wavelength tuning. However, the maximum tuning range is one half of the Bragg reflection bandwidth. Another approach is to use a ChLC doped with a light-sensitive chiral dopant [49]. The helical twisting power of the chiral dopant is modulated by illuminating UV or visible light due to the photo-isomerization of azo-benzene, enabling the Bragg reflection spectrum to be modulated from the UV region to the IR region, and an inversion of the helix. Thus, the use of a light-sensitive dopant enables large range direction-controllable and direction-reversible PC lasers.

With the slanted ChLC studied in this chapter, it is supposed that the LC director is aligned parallel to the substrate within the entire region in the cell. However, recent studies have theoretically revealed that the LC director is tilted from the substrate in the bulk [130, 131], as shown in Fig. 4.16 (a). When the grating period is comparable to the helical pitch, for a cell-type device, the LC director close to the substrate is aligned parallel to the substrate due to the strong surface anchoring, whereas the director in the bulk is gradually tilted from the substrate to minimize the elastic energy for the alignment. Thus, the slant angle of the structure is different at the substrate surface and bulk. This structure causes the helical axis to be tilted from the device normal in contrast to the slanted ChLC proposed in this chapter. However, the TEM image shown in Fig. 4.8 has the same slant structure at both the substrate surface and bulk. This implies that the alignment behaviors of the LC director in the cell-type and film-type devices are different. For the film-type slanted ChLCs described in this chapter, a spin-coating process gives a film with a thickness of ~700 nm. Owing to its thin thickness, the LC director is strongly anchored on the substrate, and thus aligned parallel to the surface. Therefore, the film-type slanted ChLCs obtained by repeatedly applying the coating process has a helical axis along the device normal, as shown in Fig. 4.16 (b). Because the alignment of the LC director on a patterned substrate affects the diffraction properties of the ChLC-based HOEs, it is further necessary to investigate the effects on the LC director with respect to various conditions such as the fabrication procedures, cell-gap, physical values of the LCs, and anchoring energy of the alignment layers.

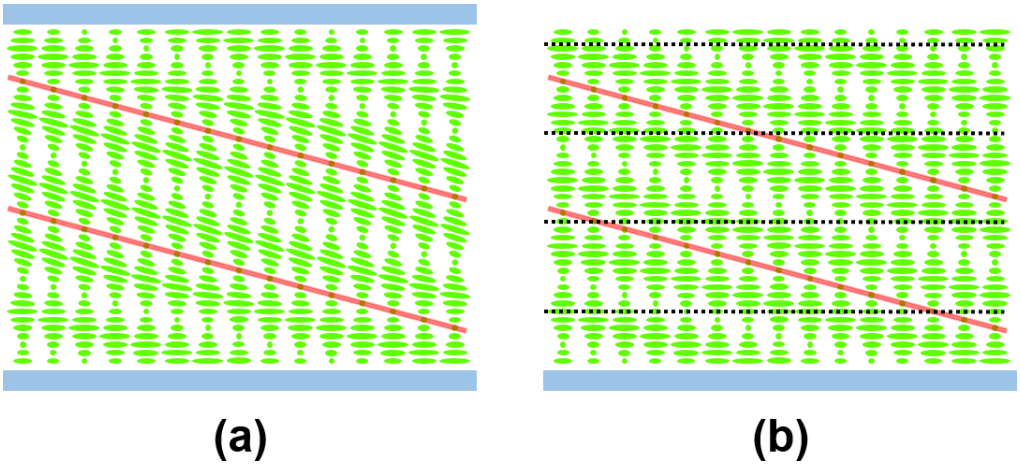


Figure 4. 16 Another configuration of the orientation of LC molecules on a sub-micrometer-patterned substrate. LC orientation in the (a) cell-type and (b) film-type devices.

4.6 Conclusion

In this chapter, a direction-controllable PC band-edge laser was demonstrated based on a ChLC with a slanted structure. The theoretical analysis of the PC structures has shown that the additional periodicity of the LC director tilts the cavity mode in a direction perpendicular to the slanted structure. The theoretical prediction was experimentally demonstrated through the fabrication of a slanted ChLC that shows the emission angle of approximately 30° from the device normal. It was also demonstrated that the device possesses the capability to tune the emission direction over a range of directions by controlling the helical pitch of the ChLC through external stimuli. The author believes that a device with a larger tuning range can be achieved by using a gain medium, i.e., either a laser dye with a broadband fluorescent spectrum or mixed nanoparticles with a different emission spectrum. Because the device demonstrated in this chapter is based on a self-organized helical structure, the fabrication does not require complex vacuum technologies such as electron and focused ion beam lithography. In addition, a large area and flexible film-type device can be realized through spin-coating or a roll-to-roll process.

Chapter 5 Conclusion

In this dissertation, various volume HOEs with advanced optical functionalities such as optical transparency, omnidirectional CP selectivity, and a direction-controllable laser emission were proposed based on two-types of chiral LCs. The advanced optical functionalities were theoretically investigated through a 4 × 4 matrix and photonic band structure, and experimentally demonstrated through the fabrication of the volume HOEs. The achievements described in each chapter are summarized as follows.

In Chapter 2, a completely transparent HOE was demonstrated using a ChLC that possesses only a single Fourier component owing to the sinusoidal dielectric tensor distribution along the helical axis. A ChLC that reflects only IR light under ambient lighting conditions was employed, which was theoretically designed using Berreman's 4 × 4 matrix method. The transparent ChLC was applied to the fabrication of a volume HOE the transparent capability of which is maintained despite the patterning process of the optical phase distribution. The transparent volume HOE has an exotic capability in which the encoded phase information can be played back by visible light illuminated at a sufficiently large angle. Two designs were employed to achieve incident light to be illuminated at the designed angle: an index-matching prism-coupled device and a device integrated to a waveguide structure. The encoded phase information was clearly reconstructed in free-space, demonstrating the capability of the volume HOEs as see-through optical components.

In Chapter 3, an omnidirectional CP-selective volume HOE was demonstrated based on 3D cubic structures. The omnidirectional CP selectivity was theoretically described by analyzing the photonic band structure of the 3D cubic structure. Through the simulation, it was confirmed that the BP maintains CP-selectivity for all angles of incidence accessible from air. For the fabrication of the volume HOEs based on the BB effect of the BPs, a field-reorientation process that simultaneously controls the [110] and [001] crystal axes on a patterned substrate was proposed. The possible mechanism of the field-reorientation process was also explained by investigating the structure of the field-induced N* and BP X. It was revealed that the N* phase is responsible for the [001] crystal axis to be aligned along the surface anchoring, while the BP X is responsible for the [110] crystal axis oriented parallel to the substrate normal. The hologram fabricated through the field-reorientation process shown a dichroic ratio upon LCP and RCP illumination of >85:1. In addition to the BB hologram using body-centered BP I, a large-angle (~41.7°), defect-free, and reflective volume deflector based on simple cubic BP II

was also demonstrated. It was suggested that the [100] crystal axis is tilted from the device normal when a short-pitch periodic modulation of the LC director (~690 nm) is introduced on a substrate. Further, it was demonstrated that the deflection characteristics of the proposed device can be tuned and switched by the application of the electric field.

In Chapter 4, I described a direction-controllable PC band-edge laser based on a ChLC with slanted helical structure. I theoretically investigated the photonic band structure of the slanted ChLC, showing that the additional modulation of the LC director in a direction perpendicular to the helical axis causes the cavity responsible for the distributed feedback to be tilted from the surface normal. In addition, the calculation predicted that the emission direction can be tuned by controlling the helical pitch. The prediction was experimentally demonstrated by pattering the LC director of the ChLC on a substrate through a polarization holography method, resulting in a laser emission with an angle of approximately 30° from the surface normal. In addition, the emission angle is tuned within an angle range of 4° by modulating the helical pitch through the control of the temperature.

Throughout this dissertation, I demonstrated various advanced optical functionalities that cannot be achieved in previous technologies such as conventional HOEs and metasurfaces. I would like to emphasize that LCs are fascinating materials for practical applications owing to a number of advantages such as self-organized 1D and 3D helical structures, and an external-stimuli responsivity. In particular, the simple fabrication and capabilities of a large-area and the mass-production of film-type devices through spin-coating or roll-to-roll processes are attractive features compared to the inorganic counterparts.

Despite the advantages of chiral LCs, several issues have to be addressed for use in practical devices. Because the main contribution of this dissertation is to propose devices with advanced optical functionalities, the optical performances are not optimized. For example, the efficiency and the SNR of the BB hologram can be further improved by employing a de-noising algorithm [82]. For the ChLC-based BB hologram, the use of a prism makes the device thick, which can be substituted into a ChLC- [34, 35] or BP-based HOEs with a large deflection angle. For the BP-based BB hologram, it is necessary to investigate the practical resolution of patterning and the actual orientation of the LC director on the substrate. Although the azimuthal orientation can be controlled through the field-reorientation process, the alignment at the interface between two regions with different easy axes is also unclear. In addition, an improvement of the alignment quality is required by employing an alignment layer with extremely high surface anchoring. In the case of the direction-controllable laser, this was proposed through a photo-pumping gain medium; however, for practical application, a current-injection emission is required. One possible solution is to use an organic gain medium that can be pumped by a

current injection [132]. In addition, it is necessary to control the emission direction without change in the emission wavelength. Another functionality for a laser device such as a collimated emission beam can be also expected with a parabolic orientation of the LC director on a substrate.

This dissertation illustrates the potential of chiral LCs for controlling the light-matter interaction, which will come to hold a unique position as compact, tunable HOEs complementing inorganic metasurfaces and conventional HOEs.

Bibliography

[1] N. Yu, P. Genevet, M. A. Kats, F. Aieta, J.-P. Tetienne, F. Capasso and Z. Gaburro, "Light propagation with phase discontinuities: generalized laws of reflection and refraction", *Science* **334**, 333-337 (2011).

[2] N. Yu and F. Capasso, "Flat optics with designer metasurfaces", *Nat. Mater.* **13**, 139-150 (2014).

[3] S. Jahani and Z. Jacob, "All-dielectric metamaterials", *Nat. Nanotechnol.* **11**, 23-36 (2016).

[4] D. Wen, F. Yue, G. Li, G. Zheng, K. Chan, S. Chen, M. Chen, K. F. Li, P. W. H. Wong and K. W. Cheah, "Helicity multiplexed broadband metasurface holograms", *Nat. Commun.* **6**, 8241 (2015).

[5] G. Zheng, H. Mühlenbernd, M. Kenney, G. Li, T. Zentgraf and S. Zhang, "Metasurface holograms reaching 80% efficiency", *Nat. Nanotechnol.* **10**, 308-312 (2015).

[6] W. T. Chen, A. Y. Zhu, V. Sanjeev, M. Khorasaninejad, Z. Shi, E. Lee and F. Capasso, "A broadband achromatic metalens for focusing and imaging in the visible", *Nat. Nanotechnol.* **13**, 220-226 (2018).

[7] S. Wang, P. C. Wu, V.-C. Su, Y.-C. Lai, M.-K. Chen, H. Y. Kuo, B. H. Chen, Y. H. Chen, T.-T. Huang and J.-H. Wang, "A broadband achromatic metalens in the visible", *Nat. Nanotechnol.* **13**, 227-232 (2018).

[8] X. Chen, Y. Zhang, L. Huang and S. Zhang, "Ultrathin metasurface laser beam shaper", *Adv. Opt. Mater.* **2**, 978-982 (2014).

[9] D. R. Smith, W. J. Padilla, D. Vier, S. C. Nemat-Nasser and S. Schultz, "Composite medium with simultaneously negative permeability and permittivity", *Phys. Rev. Lett.* **84**, 4184 (2000).

[10] N. I. Landy, S. Sajuyigbe, J. J. Mock, D. R. Smith and W. J. Padilla, "Perfect metamaterial absorber", *Phys. Rev. Lett.* **100**, 207402 (2008).

[11] R. W. Gerchberg, "A practical algorithm for the determination of phase from image and diffraction plane pictures", *Optik* **35**, 237-246 (1972).

[12] F. Wyrowski and O. Bryngdahl, "Iterative Fourier-transform algorithm applied to computer holography", *J. Opt. Soc. Am. A* **5**, 1058-1065 (1988).

[13] D. Gabor, A new microscopic principle. *Nature* **161**, 777-778 (1948).

[14] P. Bañares-Palacios, S. Álvarez-Álvarez, J. Marín-Sáez, M.-V. Collados, D. Chemisana and J. Atencia, "Broadband behavior of transmission volume holographic optical elements for solar concentration", *Opt. Express* **23**, A671-A681 (2015).

[15] H. Mukawa, K. Akutsu, I. Matsumura, S. Nakano, T. Yoshida, M. Kuwahara and K. Aiki, "A full-color eyewear display using planar waveguides with reflection volume holograms", *J. Soc. Inf. Disp.* **17**, 185-193 (2009).

[16] G. Li, D. Lee, Y. Jeong, J. Cho and B. Lee, "Holographic display for see-through augmented reality using mirror-lens holographic optical element", *Opt. Lett.* **41**, 2486-2489 (2016).

[17] M. Liu, Y. Liu, G. Zhang, Z. Peng, D. Li, J. Ma and L. Xuan, "Organic holographic polymer dispersed liquid crystal distributed feedback laser from different diffraction orders", *J. Phys. D: Appl. Phys.* **49**, 465102 (2016).

[18] L. Criante, D. Lucchetta, F. Vita, R. Castagna and F. Simoni, "Distributed feedback all-organic microlaser based on holographic polymer dispersed liquid crystals", *Appl. Phys. Lett.* **94**, 111114 (2009).

[19] Y N. Denisyuk, "On the reflection of optical properties of an object in a wave field of light scattered by it", *Dokl. Akad. Nauk SSSR* **144**, 1275-1276 (1962).

[20] E. N. Leith and J. Upatnieks, "Reconstructed wavefronts and communication theory", *J. Opt. Soc. Am.* **52**, 1123-1130 (1962).

[21] B. J. Chang and C. D. Leonard, "Dichromated gelatin for the fabrication of holographic optical elements", *Appl. Opt.* **18**, 2407-2417 (1979).

[22] D. J. Cooke and A. A. Ward, "Reflection-hologram processing for high efficiency in silver-halide emulsions", *Appl. Opt.* **23**, 934-941 (1984).

[23] M. Beesley and J. Castledine, "The use of photoresist as a holographic recording medium", *Appl. Opt.* **9**, 2720-2724 (1970).

[24] C. Yu, Y. Peng, Q. Zhao, H. Li and X. Liu, "Highly efficient waveguide display with space-variant volume holographic gratings", *Appl. Opt.* **56**, 9390-9397 (2017).

[25] F.-K. Bruder, H. Bang, T. Fäcke, R. Hagen, D. Hönel, E. Orselli, C. Rewitz, T. Rölle, D. Vukicevic and G. Walze, "Precision holographic optical elements in Bayfol HX photopolymer", *Proc. SPIE* **9771**, 977103 (2016).

[26] Z. Yue, G. Xue, J. Liu, Y. Wang and M. Gu, "Nanometric holograms based on a topological insulator material", *Nat. Commun.* **8**, 15354 (2017).

[27] G. A. Rakuljic and V. Leyva, "Volume holographic narrow-band optical filter", *Opt. Lett.* **18**, 459-461 (1993).

[28] K. Yin, T. Zhan, J. Xiong, Z. He and S.-T. Wu, "Polarization Volume Gratings for Near-Eye Displays and Novel Photonic Devices", *Crystals* **10**, 561 (2020).

[29] J. Xiong, K. Yin, K. Li and S.-T. Wu, "Holographic Optical Elements for Augmented Reality: Principles, Present Status, and Future Perspectives", *Adv. Photon. Res.* **2**, 2000049 (2020).

[30] D.-K. Yang and S.-T. Wu, *Fundamentals of liquid crystal devices*. John Wiley & Sons: 2014.

[31] P.-G. De Gennes and J. Prost, *The physics of liquid crystals*. Oxford university press: 1993; Vol. 83.

[32] J. Kobashi, H. Yoshida and M. Ozaki, "Planar optics with patterned chiral liquid crystals", *Nat. Photon.* **10**, 389-392 (2016).

[33] H. Yoshida and J. Kobashi, "Flat optics with cholesteric and blue phase liquid crystals", *Liq. Cryst.* **43**, 1909-1919 (2016).

[34] J. Kobashi, Y. Mohri, H. Yoshida and M. Ozaki, "Circularly-polarized, large-angle reflective deflectors based on periodically patterned cholesteric liquid crystals", *Opt. Data Process. Storage* **3**, 61-66 (2017).

[35] Y.-H. Lee, K. Yin and S.-T. Wu, "Reflective polarization volume gratings for high efficiency waveguide-coupling augmented reality displays", *Opt. Express* **25**, 27008-27014 (2017).

[36] K. Yin, Z. He and S. T. Wu, "Reflective Polarization Volume Lens with Small f-Number and Large Diffraction Angle", *Adv. Opt. Mater.* **8**, 2000170 (2020).

[37] J. Kobashi, H. Yoshida and M. Ozaki, "Circularly-polarized, semitransparent and double-sided holograms based on helical photonic structures", *Sci. Rep.* **7**, 16470 (2017).

[38] S. Cho, M. Ono, H. Yoshida and M. Ozaki, "Bragg-Berry flat reflectors for transparent computer-generated holograms and waveguide holography with visible color playback capability", *Sci. Rep.* **10**, 8201 (2020).

[39] Y. Mohri, J. Kobashi, H. Yoshida and M. Ozaki, "Morpho-Butterfly-Inspired Patterning of Helical Photonic Structures for Circular-Polarization-Sensitive, Wide-Angle Diffuse Reflection", *Adv. Opt. Mater.* **5**, 1601071 (2017).

[40] J. Kobashi, H. Yoshida and M. Ozaki, "Polychromatic optical vortex generation from patterned cholesteric liquid crystals", *Phys. Rev. Lett.* **116**, 253903 (2016).

[41] M. Rafayelyan and E. Brasselet, "Bragg-Berry mirrors: reflective broadband q-plates", *Opt. Lett.* **41**, 3972-3975 (2016).

[42] F. Reinitzer, "Beitrage zur Kenntniss des Cholesterins", *Monatshefte für Chemie* **9**, 421-441 (1888).

[43] D. W. Berreman, "Optics in stratified and anisotropic media: 4× 4-matrix formulation", *J. Opt. Soc. Am.* **62**, 502-510 (1972).

[44] P. Yeh and C. Gu, *Optics of liquid crystal displays*. John Wiley & Sons: 2009; Vol. 67.

[45] T. Matsui, R. Ozaki, K. Funamoto, M. Ozaki and K. Yoshino, "Flexible mirrorless laser based on a free-standing film of photopolymerized cholesteric liquid crystal", *Appl. Phys. Lett.* **81**, 3741-3743 (2002).

[46] Y. Inoue, H. Yoshida, K. Inoue, Y. Shiozaki, H. Kubo, A. Fujii and M. Ozaki, "Tunable lasing from a cholesteric liquid crystal film embedded with a liquid crystal nanopore network", *Adv. Mater.* **23**, 5498-5501 (2011).

[47] Y. Huang, Y. Zhou, C. Doyle and S.-T. Wu, "Tuning the photonic band gap in cholesteric liquid crystals by temperature-dependent dopant solubility", *Opt. Express* **14**, 1236-1242 (2006).

[48] Y. Inoue, H. Yoshida, H. Kubo and M. Ozaki, "Deformation-Free, Microsecond Electro-Optic Tuning of Liquid Crystals", *Adv. Opt. Mater.* **1**, 256-263 (2013).

[49] P. Chen, L.-L. Ma, W. Hu, Z.-X. Shen, H. K. Bisoyi, S.-B. Wu, S.-J. Ge, Q. Li and Y.-Q. Lu, "Chirality invertible superstructure mediated active planar optics", *Nat. Commun.* **10**, 2518 (2019).

[50] P. V. Shibaev, P. Rivera, D. Teter, S. Marsico, M. Sanzari, V. Ramakrishnan and E. Hanelt, "Color changing and lasing stretchable cholesteric films", *Opt. Express* **16**, 2965-2970 (2008).

[51] J. Thoen, "Adiabatic scanning calorimetric results for the blue phases of cholesteryl nonanoate", *Phys. Rev. A* **37**, 1754 (1988).

[52] S. Tanaka, H. Yoshida, Y. Kawata, R. Kuwahara, R. Nishi and M. Ozaki, "Double-twist cylinders in liquid crystalline cholesteric blue phases observed by transmission electron microscopy", *Sci. Rep.* **5**, 16180 (2015).

[53] K. Higashiguchi, K. Yasui and H. Kikuchi, "Direct observation of polymer-stabilized blue phase I structure with confocal laser scanning microscope", *J. Am. Chem. Soc.* **130**, 6326-6327 (2008).

[54] H. Kikuchi, M. Yokota, Y. Hisakado, H. Yang and T. Kajiyama, "Polymer-stabilized liquid crystal blue phases", *Nat. Mater.* **1**, 64-68 (2002).

[55] S.-Y. Jo, S.-W. Jeon, B.-C. Kim, J.-H. Bae, F. Araoka and S.-W. Choi, "Polymer stabilization of liquid-crystal blue phase II toward photonic crystals", *ACS Appl. Mater. Interfaces* **9**, 8941-8947 (2017).

[56] H. J. Coles and M. N. Pivnenko, "Liquid crystal 'blue phases' with a wide temperature range", *Nature* **436**, 997-1000 (2005).

[57] A. Yoshizawa, M. Sato and J. Rokunohe, "A blue phase observed for a novel chiral compound possessing molecular biaxiality", *J. Mater. Chem.* **15**, 3285-3290 (2005).

[58] S.-T. Hur, M.-J. Gim, H.-J. Yoo, S.-W. Choi and H. Takezoe, "Investigation for correlation between elastic constant and thermal stability of liquid crystalline blue phase I", *Soft Matter* **7**, 8800-8803 (2011).

[59] H. Yoshida, Y. Tanaka, K. Kawamoto, H. Kubo, T. Tsuda, A. Fujii, S. Kuwabata, H. Kikuchi and M. Ozaki, "Nanoparticle-stabilized cholesteric blue phases", *Appl. Phy. Express* **2**, 121501 (2009).

[60] T. Noma, M. Ojima, H. Asagi, Y. Kawahira, A. Fujii, M. Ozaki and H. Kikuchi, "Effects of polymer network surfaces on expansion of cholesteric blue phases temperature", *e-J. Surf. Sci. Nanotech.* **6**, 17-20 (2008).

[61] J.-i. Fukuda, M. Yoneya and H. Yokoyama, "Simulation of cholesteric blue phases using a Landau–de Gennes theory: Effect of an applied electric field", *Phys. Rev. E* **80**, 031706 (2009).

[62] H. Yoshida, K. Anucha, Y. Ogawa, Y. Kawata, M. Ozaki, J.-i. Fukuda and H. Kikuchi, "Bragg reflection band width and optical rotatory dispersion of cubic blue-phase liquid crystals", *Phys. Rev. E* **94**, 042703 (2016).

[63] W. Cao, A. Munoz, P. Palffy-Muhoray and B. Taheri, "Lasing in a three-dimensional photonic crystal of the liquid crystal blue phase II", *Nat. Mater.* **1**, 111-113 (2002).

[64] S.-T. Hur, B. R. Lee, M.-J. Gim, K.-W. Park, M. H. Song and S.-W. Choi, "Liquid-crystalline blue phase laser with widely tunable wavelength", *Adv. Mater.* **25**, 3002 (2013).

[65] S. Pancharatnam, In Generalized theory of interference and its applications, *Proc. Indian Acad. Sci. A* **44**, 247-262 (1956).

[66] M. V. Berry, "Quantal phase factors accompanying adiabatic changes", *Proc. R. Soc. A* **392**, 45-57 (1984).

[67] M. Honma and T. Nose, "Liquid-crystal blazed grating with azimuthally distributed liquid-crystal directors", *Appl. Opt.* **43**, 5193-5197 (2004).

[68] D. Mawet, E. Serabyn, K. Liewer, C. Hanot, S. McEldowney, D. Shemo and N. O'Brien, "Optical vectorial vortex coronagraphs using liquid crystal polymers: theory, manufacturing and laboratory demonstration", *Opt. Express* **17**, 1902-1918 (2009).

[69] J. Kobashi, H. Yoshida and M. Ozaki, "Broadband optical vortex generation from patterned cholesteric liquid crystals", *Mol. Cryst. Liq. Cryst.* **646**, 116-124 (2017).

[70] C. Mock-Knoblauch, O. S. Enger and U. D. Schalkowsky, In L-7: Late-News Paper: Novel Polymerisable Liquid Crystalline Acrylates for the Manufacturing of Ultrathin Optical Films, *SID Symp. Dig. Tech. Pap.* **37**, 1673-1676 (2006).

[71] J.-H. Kim, M. Yoneya and H. Yokoyama, "Tristable nematic liquid-crystal device using micropatterned surface alignment", *Nature* **420**, 159-162 (2002).

[72] K. Ichimura, "Photoalignment of liquid-crystal systems", *Chem. Rev.* **100**, 1847-1874 (2000).

[73] V. G. Chigrinov, V. M. Kozenkov and H.-S. Kwok, *Photoalignment of liquid crystalline materials: physics and applications*. John Wiley & Sons: 2008; Vol. 17.

[74] C. H. Lee, H. Yoshida, Y. Miura, A. Fujii and M. Ozaki, "Local liquid crystal alignment on patterned micrograting structures photofabricated by two photon excitation direct laser writing", *Appl. Phys. Lett.* **93**, 173509 (2008).

[75] K. Ichimura, Y. Suzuki, T. Seki, A. Hosoki and K. Aoki, "Reversible change in alignment mode of nematic liquid crystals regulated photochemically by command surfaces modified with an azobenzene monolayer", *Langmuir* **4**, 1214-1216 (1988).

[76] T. Seki, "New strategies and implications for the photoalignment of liquid crystalline polymers", *Polym. J.* **46**, 751-768 (2014).

[77] C. Culbreath, N. Glazar and H. Yokoyama, "Note: Automated maskless micro-multidomain photoalignment", *Rev. Sci. Instrum.* **82**, 126107 (2011).

[78] T. Todorov, L. Nikolova and N. Tomova, "Polarization holography. 2: Polarization holographic gratings in photoanisotropic materials with and without intrinsic birefringence", *Appl. Opt.* **23**, 4588-4591 (1984).

[79] Z. Huang, D. L. Marks and D. R. Smith, "Out-of-plane computer-generated multicolor waveguide holography", *Optica* **6**, 119-124 (2019).

[80] J. W. Goodman, *Introduction to Fourier optics*. Roberts and Company Publishers: 2005.

[81] O. K. Ersoy, *Diffraction, Fourier optics and imaging*. John Wiley & Sons: 2006; Vol. 30.

[82] V. Bianco, P. Memmolo, M. Leo, S. Montresor, C. Distante, M. Paturzo, P. Picart, B. Javidi and P. Ferraro, "Strategies for reducing speckle noise in digital holography", *Light Sci. Appl.* **7**, 1-16 (2018).

[83] F. Shen and A. Wang, "Fast-Fourier-transform based numerical integration method for the Rayleigh-Sommerfeld diffraction formula", *Appl. Opt.* **45**, 1102-1110 (2006).

[84] J. E. Ford, F. Xu, K. Urquhart and Y. Fainman, "Polarization-selective computer-generated holograms", *Opt. Lett.* **18**, 456-458 (1993).

[85] W. Yu, T. Konishi, T. Hamamoto, H. Toyota, T. Yotsuya and Y. Ichioka, "Polarization-multiplexed diffractive optical elements fabricated by subwavelength structures", *Appl. Opt.* **41**, 96-100 (2002).

[86] J. Kim, Y. Li, M. N. Miskiewicz, C. Oh, M. W. Kudenov and M. J. Escuti, "Fabrication of ideal geometric-phase holograms with arbitrary wavefronts", *Optica* **2**, 958-964 (2015).

[87] M. Honma and T. Nose, "Liquid-crystal blazed grating with azimuthally distributed liquid-crystal directors", *Appl. Opt.* **43**, 5193-5197 (2004).

[88] L. Marrucci, C. Manzo and D. Paparo, "Optical spin-to-orbital angular momentum conversion in inhomogeneous anisotropic media", *Phys. Rev. Lett.* **96**, 163905 (2006).

[89] R. C. Devlin, M. Khorasaninejad, W. T. Chen, J. Oh and F. Capasso, "Broadband high-efficiency dielectric metasurfaces for the visible spectrum", *Proc. Natl. Acad. Sci.* **113**, 10473-10478 (2016).

[90] S. Wang, P. C. Wu, V.-C. Su, Y.-C. Lai, C. H. Chu, J.-W. Chen, S.-H. Lu, J. Chen, B. Xu and C.-H. Kuan, "Broadband achromatic optical metasurface devices", *Nat. Commun.* **8**, 187 (2017).

[91] C.-W. Chen, C.-T. Hou, C.-C. Li, H.-C. Jau, C.-T. Wang, C.-L. Hong, D.-Y. Guo, C.-Y. Wang, S.-P. Chiang and T. J. Bunning, "Large three-dimensional photonic crystals based on monocrystalline liquid crystal blue phases", *Nat. Commun.* **8**, 727 (2017).

[92] Y. Chen and S.-T. Wu, "Electric field-induced monodomain blue phase liquid crystals", *Appl. Phys. Lett.* **102**, 171110 (2013).

[93] M. Chen, Y.-H. Lin, H.-S. Chen and H.-Y. Chen, "Electrically assisting crystal growth of blue phase liquid crystals", *Opt. Mater. Express* **4**, 953-959 (2014).

[94] K. Kim, S.-T. Hur, S. Kim, S.-Y. Jo, B. R. Lee, M. H. Song and S.-W. Choi, "A well-aligned simple cubic blue phase for a liquid crystal laser", *J. Mater. Chem. C* **3**, 5383-5388 (2015).

[95] Z. G. Zheng, C. L. Yuan, W. Hu, H. K. Bisoyi, M. J. Tang, Z. Liu, P. Z. Sun, W. Q. Yang, X. Q. Wang and D. Shen, "Light-patterned crystallographic direction of a self-organized 3d soft photonic crystal", *Adv. Mater.* **29**, 1703165 (2017).

[96] J. A. Martínez-González, X. Li, M. Sadati, Y. Zhou, R. Zhang, P. F. Nealey and J. J. De Pablo, "Directed self-assembly of liquid crystalline blue-phases into ideal single-crystals", *Nat. Commun.* **8**, 15854 (2017).

[97] K. Zhou, H. K. Bisoyi, J. Q. Jin, C. L. Yuan, Z. Liu, D. Shen, Y. Q. Lu, Z. G. Zheng, W. Zhang and Q. Li, "Light-Driven Reversible Transformation between Self-Organized

Simple Cubic Lattice and Helical Superstructure Enabled by a Molecular Switch Functionalized Nanocage", *Adv. Mater.* **30**, 1800237 (2018).

[98] X. Li, J. A. Martínez-González, O. Guzmán, X. Ma, K. Park, C. Zhou, Y. Kambe, H. M. Jin, J. A. Dolan and P. F. Nealey, "Sculpted grain boundaries in soft crystals", *Sci. Adv.* **5**, eaax9112 (2019).

[99] M. Takahashi, T. Ohkawa, H. Yoshida, J.-i. Fukuda, H. Kikuchi and M. Ozaki, "Orientation of liquid crystalline blue phases on unidirectionally orienting surfaces", *J. Phys. D: Appl. Phys.* **51**, 104003 (2018).

[100] Y. Inoue and H. Moritake Formation of a defect-free uniform lying helix in a thick cholesteric liquid crystal cell. *Appl. Phys. Lett.* **8**, 071701 (2015).

[101] H.-S. Kitzerow, "The effect of electric fields on blue phases", *Mol. Cryst. Liq. Cryst.* **202**, 51-83 (1991).

[102] G. Alexander and D. Marenduzzo, "Cubic blue phases in electric fields", *Europhys. Lett.* **81**, 66004 (2008).

[103] G. Alexander and J. Yeomans, "Numerical results for the blue phases", *Liq. Cryst.* **36**, 1215-1227 (2009).

[104] J. Yan, Y. Chen, D. Xu and S.-T. Wu, "Angular dependent reflections of a monodomain blue phase liquid crystal", *J. Appl. Phys.* **114**, 113106 (2013).

[105] A. Stathopoulos and J. R. McCombs, "PRIMME: preconditioned iterative multimethod eigensolver—methods and software description", *ACM Trans. Math. Software* **37**, 1-30 (2010).

[106] J.-i. Fukuda, Y. Okumura and H. Kikuchi, "Calculation of confocal microscope images of cholesteric blue phases", *Proc. SPIE* **9769**, 976906 (2016).

[107] E. Anderson, Z. Bai, C. Bischof, L. S. Blackford, J. Demmel, J. Dongarra, J. Du Croz, A. Greenbaum, S. Hammarling and A. McKenney, "*LAPACK User's Guide*", Third edition (Society for Industrial and Applied Mathematics, 1999).

[108] E. Yablonovitch, "Inhibited spontaneous emission in solid-state physics and electronics", *Phys. Rev. Lett.* **58**, 2059 (1987).

[109] K. Busch and S. John, "Photonic properties of strongly correlated colloidal liquids", *Phys. Rev. Lett.* **83**, 967 (1999).

[110] M. Yoshida, M. De Zoysa, K. Ishizaki, Y. Tanaka, M. Kawasaki, R. Hatsuda, B. Song, J. Gelleta and S. Noda, "Double-lattice photonic-crystal resonators enabling high-brightness semiconductor lasers with symmetric narrow-divergence beams", *Nat. Mater.* **18**, 121-128 (2019).

[1 1 1] Y. Kurosaka, S. Iwahashi, Y. Liang, K. Sakai, E. Miyai, W. Kunishi, D. Ohnishi and S. Noda, "On-chip beam-steering photonic-crystal lasers" *Nat. Photon.* **4**, 447 (2010). 2010.

[1 1 2] S. Noda, M. Yokoyama, M. Imada, A. Chutinan and M. Mochizuki, "Polarization mode control of two-dimensional photonic crystal laser by unit cell structure design", *Science* **293**, 1123-1125 (2001).

[1 1 3] Y. Kurosaka, K. Hirose, T. Sugiyama, Y. Takiguchi and Y. Nomoto, "Phase-modulating lasers toward on-chip integration", *Sci. Rep.* **6**, 30138 (2016).

[1 1 4] W. Huang, Z. Diao, Y. Liu, Z. Peng, C. Yang, J. Ma and L. Xuan, "Distributed feedback polymer laser with an external feedback structure fabricated by holographic polymerization technique", *Org. Electron.* **13**, 2307-2311 (2012).

[1 1 5] T. Smirnova, O. Sakhno, J. Stumpe, V. Kzianzou and S. Schrader, "Distributed feedback lasing in dye-doped nanocomposite holographic transmission gratings", *J. Opt.* **13**, 035709 (2011).

[1 1 6] W. Huang, Z. Diao, L. Yao, Z. Cao, Y. Liu, J. Ma and L. Xuan, "Electrically tunable distributed feedback laser emission from scaffolding morphologic holographic polymer dispersed liquid crystal grating", *Appl. Phys. Express* **6**, 022702 (2013).

[1 1 7] S. Cho, H. Yoshida and M. Ozaki, "Emission Direction-Tunable Liquid Crystal Laser", *Adv. Opt. Mater.* **8**, 2000375 (2020).

[1 1 8] L.-J. Chen, J.-D. Lin and C.-R. Lee, "An optically stable and tunable quantum dot nanocrystal-embedded cholesteric liquid crystal composite laser", *J. Mater. Chem. C* **2**, 4388-4394 (2014).

[1 1 9] L.-J. Chen, J.-H. Dai, J.-D. Lin, T.-S. Mo, H.-P. Lin, H.-C. Yeh, Y.-C. Chuang, S.-A. Jiang and C.-R. Lee, "Wavelength-Tunable and Highly Stable Perovskite-Quantum-Dot-Doped Lasers with Liquid Crystal Lasing Cavities", *ACS Appl. Mater. Interfaces* **10**, 33307-33315 (2018).

[1 2 0] K. Funamoto, M. Ozaki and K. Yoshino, "Discontinuous shift of lasing wavelength with temperature in cholesteric liquid crystal", *Jpn. J. Appl. Phys.* **42**, L1523 (2003).

[1 2 1] T.-H. Lin, Y.-J. Chen, C.-H. Wu, A. Y.-G. Fuh, J.-H. Liu and P.-C. Yang, "Cholesteric liquid crystal laser with wide tuning capability", *Appl. Phys. Lett.* **86**, 161120 (2005).

[1 2 2] T. Ali, J. D. Lin, B. Snow, X. Wang, S. J. Elston and S. M. Morris, "A Thin-Film Flexible Defect-Mode Laser", *Adv. Opt. Mater.* **8**, 1901891 (2020).

[1 2 3] H. Yoshida, Y. Shiozaki, Y. Inoue, M. Takahashi, Y. Ogawa, A. Fujii and M. Ozaki, "Threshold improvement in uniformly lying helix cholesteric liquid crystal laser using auxiliary π-conjugated polymer active layer", *J. Appl. Phys.* **113**, 203105 (2013).

[124] Y. Inoue, H. Yoshida, K. Inoue, A. Fujii and M. Ozaki, "Improved Lasing Threshold of Cholesteric Liquid Crystal Lasers with In-Plane Helix Alignment", *Appl. Phys. Express* **3**, 102702 (2010).

[125] B. Park, M. Kim, S. W. Kim, W. Jang, H. Takezoe, Y. Kim, E. H. Choi, Y. H. Seo, G. S. Cho and S. O. Kang, "Electrically Controllable Omnidirectional Laser Emission from a Helical-Polymer Network Composite Film", *Adv. Mater.* **21**, 771-775 (2009).

[126] C. s. L. Folcia, J. Ortega and J. s. Etxebarria, "Cone-shaped emissions in cholesteric liquid crystal lasers: The role of anomalous scattering in photonic structures", *ACS Photonics* **5**, 4545-4553 (2018).

[127] C.-R. Lee, S.-H. Lin, H.-C. Yeh, T.-D. Ji, K.-L. Lin, T.-S. Mo, C.-T. Kuo, K.-Y. Lo, S.-H. Chang and A. Y.-G. Fuh, "Color cone lasing emission in a dye-doped cholesteric liquid crystal with a single pitch", *Opt. Express* **17**, 12910-12921 (2009).

[128] R. Ozaki, S. Hashimura, S. Yudate, K. Kadowaki, H. Yoshida and M. Ozaki, "Optical properties of selective diffraction from Bragg-Berry cholesteric liquid crystal deflectors", *OSA Continuum* **2**, 3554-3563 (2019).

[129] T. J. Bunning, D. L. Vezie, P. F. Lloyd, P. D. Haaland, E. L. Thomas and W. W. Adams, "Cholesteric liquid crystals: image contrast in the TEM", *Liq. Cryst.* **16**, 769-781 (1994).

[130] I. Nys, M. Stebryte, Y. Y. Ussembayev, J. Beeckman and K. Neyts, "Tilted Chiral Liquid Crystal Gratings for Efficient Large-Angle Diffraction", *Adv. Opt. Mater.* **7**, 1901364 (2019).

[131] M. Stebryte, I. Nys, Y. Y. Ussembayev, J. Beeckman and K. Neyts, "Large Angle Forward Diffraction by Chiral Liquid Crystal Gratings with Inclined Helical Axis", *Crystals* **10**, 807 (2020).

[132] A. S. Sandanayaka, T. Matsushima, F. Bencheikh, S. Terakawa, W. J. Potscavage Jr, C. Qin, T. Fujihara, K. Goushi, J.-C. Ribierre and C. Adachi, "Indication of current-injection lasing from an organic semiconductor", *Appl. Phy. Express* **12**, 061010 (2019).

[133] G.-z. Yang, B.-z. Dong, B.-y. Gu, J.-y. Zhuang and O. K. Ersoy, "Gerchberg–Saxton and Yang–Gu algorithms for phase retrieval in a nonunitary transform system: a comparison", *Appl. Opt.* **33**, 209-218 (1994).

Acknowledgments

I would like to express my sincere appreciation to my supervisor professor Masanori Ozaki, who has guided me to complete this PhD dissertation. His leadership and encouragement have assisted me to continue my research and pursue my life's goal in Japan. This dissertation could not have been written without his guidance. I would also like to extend my gratitude to associate professor Hiroyuki Yoshida. He has attentively instructed me in the fundamental physics and optics of liquid crystals, as well as techniques for experiments with microscopes and lasers. I am also thankful to associate professor Akihiko Fujii for his perceptive comments and advice.

I would like to extend my gratitude to all the professors at the Division of Electrical, Electronic and Infocommunications Engineering at Osaka University. I particularly appreciate professor Ryuji Katayama for reviewing this dissertation. I am also grateful to professor Yusuke Mori, professor Mitsuhiro Katayama, professor Masahiko Kondow, professor Nobuya Mori, professor Tetsuya Hirose, professor Tetsuya Yagi for serving on my dissertation committee. I also thank professor Masayoshi Tonouchi and professor Akira Oiwa, for their wonderful lectures about electronic device engineering while taking my PhD course.

I would like to extend my appreciation to professor Jun-ichi Fukuda at Kyushu University for providing the simulated optical properties of BPs and taking the time to discuss about the results. I would not have been able to understand the optical properties of BPs if we did not have that time for discussions. I also thank to Mr. Kenzo Uehira, Prof. Satoshi Ichikawa, and Prof. Hidehiro Yasuda at the Research Center for Ultra-High Voltage Electron Microscopy, Osaka University, for technical assistance with the TEM observations.

I also thank both the present and former members of Ozaki laboratory: Dr. Giichi Shibuya, Dr. Sunri Lee, Dr. Koki Imamura, Mr. Ken Watanabe, Mr. Kanta Sunami, Mr. Tomohiro Ouchi, Mr. Masaru Ono, Ms. Misaki Takahashi, Mr. Yuki Nishikawa, Mr. WooJin Kim, Mr. Fun Zijan, Mr. Yuto Iwata, Mr, Yuji Tsukamoto, Mr. Yuto Tsuboi, Mr. Ryo Hasegawa, and Mr. Shogo Mitsuhashi. It has been a pleasure working with them and I really enjoyed the time we spent together.

I also thank BASF Japan Ltd. for providing photo-reactive mesogens and photo-initiator, and DIC and JNC Corporation for providing the photo-alignment materials, used for the experiments described in this dissertation.

Most of all, I would like to extend my heartfelt gratitude to my parents and younger brother for their supports, love, and encouragement.

Achievements

Publications

1. **S. Cho**, M. Ono, H. Yoshida, and M. Ozaki, Bragg-Berry flat reflectors for transparent computer-generated holograms and waveguide holography with visible color playback capability, *Sci. Rep.* **10**, 8201, (2020).
2. **S. Cho**, H. Yoshida, and M. Ozaki, Emission Direction-Tunable Liquid Crystal Laser, *Adv. Opt. Mater.* **8**, 2000375, (2020).
3. **S. Cho**, M. Takahashi, J. Fukuda, H. Yoshida and M. Ozaki, Directed self-assembly of soft 3D photonic crystals for holograms with omnidirectional circular-polarization selectivity, accepted to *Commun. Mater.*
4. M. G. Nassiri, **S. Cho**, H. Yoshida, M. Ozaki, and E. Brasselet, High-order Laguerre-Gauss polychromatic beams from Bragg-Berry flat-optics, *Phys. Rev. E* **98**, 063834, (2018).
5. W. Zhang, S. Suzuki, **S. Cho**, G. Watanabe, H. Yoshida, T. Sakurai, M. Aotani, Y. Tsutsui, M. Ozaki, and S. Seki, Highly Miscible Hybrid Liquid-Crystal Systems Containing Fluorescent Excited-State Intramolecular Proton Transfer Molecules, *Langmuir* **35**, 14031-14041, (2019).

Conferences

1. **S. Cho**, H. Yoshida, and M. Ozaki, Fully Transparent Hologram using Photo Patterned Cholesteric Liquid Crystals, 6th TOYOTA RIKEN International Workshop on Chirality in Soft Matter, Toyota commemorative museum of industry and technology, Nagoya, Japan, 2017. (Poster)
2. **S. Cho**, M. Ono, H. Yoshida, and M. Ozaki, Photo-Patterned Cholesteric Liquid Crystals for Transparent Hologram, Global Nanophotonics 2017, Sheridan Beach Resort and Spa, Palawan, Philippines, 2017. (Poster)
3. **S. Cho**, M. Ono, H. Yoshida, and M. Ozaki, Transparent Hologram based on Photo-Patterned Cholesteric Liquid Crystals, Japan society of applied physics (Spring meeting), Waseda University, Tokyo, Japan, 2018. (Poster)

4. **S. Cho**, M. Ono, H. Yoshida, and M. Ozaki, Fully Transparent Hologram with Photo-Patterned Cholesteric Liquid Crystals, 27th International Liquid Crystal Conference, Kyoto international conference center, Kyoto, Japan, 2018. (Poster)
5. H. Yoshida, M. Ono, **S. Cho**, and M. Ozaki, Enhanced Pancharatnam-Berry Phase in Reflective Diffractive Optical Elements based on Liquid Crystals, The 18th International Meeting on Information displays, Bexco, Busan, Republic of Korea 2018. (Oral)
6. **S. Cho**, M. Takahashi, H. Yoshida and M. Ozaki, Angular Dependence of the Bragg Reflection Band of Blue Phase Liquid Crystals, The Japanese Liquid Crystal Conference, Gifu University, Gifu, Japan, 2018. (Poster)
7. H. Yoshida, **S. Cho**, M. Ono, Y. Tsuboi, Z. Fan, and M. Ozaki, Cholesteric Liquid Crystals as Solution-Processable Holographic Optical Elements, The 25th International Display Workshops, Nagoya congress center, Nagoya, Japan, 2018. (Oral)
8. **趙 成龍**, 小野 優, 吉田 浩之, 尾崎 雅則, Photo-Patterned Cholesteric Liquid Crystals for Transparent Holographic Optical Elements, 平成 30 年度第 3 回支部講演会, 大阪大学, 大阪, 日本, 2019. (poster)
9. **S. Cho**, M. Ono, H. Yoshida, and M. Ozaki, Transparent Computer-Generated Hologram based on Photo-Patterned Cholesteric Liquid Crystals, Optics & Photonics international 2019, Pacifico Yokohama, Yokohama, Japan, 2019. (Oral)
10. H. Yoshida, **S. Cho**, and M. Ozaki, Transparent Waveguide Holography based on Cholesteric Liquid Crystals, Japan society of applied physics (Autumn meeting), Hokkaido University, Sapporo, Japan, 2019. (Oral)
11. H. Yoshida, **S. Cho**, M. Ono, Y. Tsuboi, Z. Fan, and M. Ozaki, Enhanced Pancharatnam-Berry Phase in Double-layered Liquid Crystal Structure, Photonics & Electromagnetics Research Symposium 2019 in Rome, University of Rome "La Sapienza", Rome, Italy, 2019. (Oral)
12. **S. Cho**, H. Yoshida, and M. Ozaki, Photo-Patterned Cholesteric Liquid Crystals for Transparent Computer-Generated Waveguide Holography with Visible Playback Capability, 26th International Display Workshops, Sapporo convention center, Sapporo, Japan, 2019. (Poster)
13. **S. Cho**, H. Yoshida, and M. Ozaki, Transparent Computer-Generated Waveguide Hologram based on a Photo-Patterned Cholesteric Liquid Crystal, Optics & Photonics Japan 2019, Osaka university, Osaka, Japan, 2019. (Oral)
14. H. Yoshida, **S. Cho**, R. Ozaki, and M. Ozaki, Bragg-Berry Reflective Flat Optics based on Chiral Liquid Crystals, NJU-Wiley Joint Conference on Metamaterials and Advanced

Applications, Nanjing University International Conference Center, Nanjing, China, 2019. (Oral)

15. H. Yoshida, R. Ozaki, **S. Cho**, Z. Fan, and M. Ozaki, Optical Properties of Bragg-Berry Cholesteric Liquid Crystal Deflectors, The 9th International Symposium on Liquid Crystals Phonics, Beijing, China, 2020. (Oral)
16. **S. Cho**, H. Yoshida, and M. Ozaki, Directional Lasing Emission based on Self-Organized Photonic Crystals with Helical Nanostructures, Japan society of applied physics (Autumn meeting), Sophia University, Tokyo, Japan, 2020. (Oral)
17. M. Ozaki, **S. Cho**, and H. Yoshida, Lattice Orientation Control of Cholesteric Blue Phase and Its Hologram Application, SPIE Optics & Photonics, Online conference, 2020. (Oral)
18. **S. Cho**, H. Yoshida, and M. Ozaki, Field-Induced Reorientation of Three-dimensional Photonic Structure for Computer-Generated Holograms, SPIE Photonics West, Online conference, 2021. (Oral)

Appendices

Appendix A. Berreman's 4 × 4 matrix

Berreman's 4 × 4 matrix is a powerful technique for numerically solving the light propagation in a stratified anisotropic medium using Maxwell's equation [43]. Through this method, various information on propagating light in a medium can be obtained, such as the reflectance, transmittance, and polarization. Because ChLCs are created through one-dimensional twist of the LC director, the behavior of light in ChLC can be also analyzed. Here, a mathematical derivation on the Berreman's 4 × 4 matrix is introduced.

Maxwell's equations without free-charges and currents in a medium are expressed as

$$\nabla \cdot \boldsymbol{E} = 0, \tag{B.1a}$$

$$\nabla \cdot \boldsymbol{H} = 0, \tag{B.1b}$$

$$\nabla \times \boldsymbol{E} = -\frac{\partial \boldsymbol{B}}{\partial t}, \tag{B.1c}$$

$$\nabla \times \boldsymbol{H} = \frac{\partial \boldsymbol{D}}{\partial t}, \tag{B.1d}$$

where $\boldsymbol{E}$ and $\boldsymbol{H}$ are electric and magnetic field, and $\boldsymbol{B}$ and $\boldsymbol{D}$ are the electric and magnetic densities in a medium, and are described as

$$\boldsymbol{D} = \varepsilon_0 \boldsymbol{\varepsilon} \boldsymbol{E}, \tag{B.2a}$$

$$\boldsymbol{B} = \mu_0 \boldsymbol{H}, \tag{B.2b}$$

where ε_0 and μ_0 are the permittivity and permeability of a vacuum, and $\boldsymbol{\varepsilon}$ is the dielectric tensor distribution in the medium, which is described as

$$\boldsymbol{\varepsilon} = \begin{pmatrix} \varepsilon_{xx} & \varepsilon_{xy} & \varepsilon_{xz} \\ \varepsilon_{yx} & \varepsilon_{yy} & \varepsilon_{yz} \\ \varepsilon_{zx} & \varepsilon_{zy} & \varepsilon_{zz} \end{pmatrix}. \tag{B.3}$$

When the dielectric tensor is a function along the helical axis, the Maxwell equation can be solved as

$$\boldsymbol{E} = \boldsymbol{E}_0(z) e^{i(k_x z - \omega t)}, \tag{B.4a}$$

$$\boldsymbol{H} = \boldsymbol{H}_0(z) e^{i(k_x z - \omega t)}, \tag{B.4b}$$

where ω and k_x are the angular frequency and wavevector. When the light is propagated through a homogeneous medium with refractive index of n_o, k_x is obtained as $k_x = \frac{n_o \omega}{c} \sin\theta_i$, where θ_i is the incident angle. From Eq. (B.1) to (B.4), a 6 × 6 matrix of Maxwell's equation can be obtained as

$$\begin{pmatrix} -\frac{\partial E_{0z}}{\partial z} \\ \frac{\partial E_{0x}}{\partial z} - ik_x E_{0z} \\ ik_x E_{0y} \\ \frac{\partial H_{0y}}{\partial z} \\ -\frac{\partial H_{0x}}{\partial z} + ik_x H_{0z} \\ -ik_x H_{0x} \end{pmatrix} = i\omega \begin{pmatrix} 0 & 0 & 0 & \mu_0 & 0 & 0 \\ 0 & 0 & 0 & 0 & \mu_0 & 0 \\ 0 & 0 & 0 & 0 & 0 & \mu_0 \\ \varepsilon_0\varepsilon_{xx} & \varepsilon_0\varepsilon_{xy} & \varepsilon_0\varepsilon_{xz} & 0 & 0 & 0 \\ \varepsilon_0\varepsilon_{yx} & \varepsilon_0\varepsilon_{yy} & \varepsilon_0\varepsilon_{yz} & 0 & 0 & 0 \\ \varepsilon_0\varepsilon_{zx} & \varepsilon_0\varepsilon_{zy} & \varepsilon_0\varepsilon_{zz} & 0 & 0 & 0 \end{pmatrix} \begin{pmatrix} E_{0x} \\ E_{0y} \\ E_{0z} \\ H_{0x} \\ H_{0y} \\ H_{0z} \end{pmatrix}. \tag{B.5}$$

Equation (B.5) can be reduced to a 4 × 4 matrix by eliminating two components E_{oz} and H_{oz}

$$\frac{\partial}{\partial z}\begin{pmatrix} \overline{E}_{0x} \\ \overline{E}_{0y} \\ \overline{H}_{0x} \\ \overline{H}_{0y} \end{pmatrix} = \frac{i\omega}{c} \begin{pmatrix} -\frac{\varepsilon_{zx}}{\varepsilon_{zz}}\frac{ck_x}{\omega} & 1-\frac{1}{\varepsilon_{zz}}\left(\frac{ck_x}{\omega}\right)^2 & -\frac{\varepsilon_{zy}}{\varepsilon_{zz}}\frac{ck_x}{\omega} & 0 \\ 0 & 0 & 0 & -1 \\ \varepsilon_{xx}-\frac{\varepsilon_{xz}\varepsilon_{zx}}{\varepsilon_{zz}} & -\frac{\varepsilon_{xz}}{\varepsilon_{zz}}\frac{ck_x}{\omega} & \varepsilon_{xy}-\frac{\varepsilon_{xz}\varepsilon_{zy}}{\varepsilon_{zz}} & 0 \\ \frac{\varepsilon_{yz}\varepsilon_{zx}}{\varepsilon_{zz}}-\varepsilon_{yx} & \frac{\varepsilon_{yz}}{\varepsilon_{zz}}\frac{ck_x}{\omega} & \left(\frac{ck_x}{\omega}\right)^2-\varepsilon_{yy}+\frac{\varepsilon_{yz}\varepsilon_{zy}}{\varepsilon_{zz}} & 0 \end{pmatrix} \begin{pmatrix} \overline{E}_{0x} \\ \overline{E}_{0y} \\ \overline{H}_{0x} \\ \overline{H}_{0y} \end{pmatrix}, \tag{B.6}$$

where $\overline{E}_{0x} = \sqrt{\varepsilon_0}\, E_{0x}$, $\overline{E}_{0y} = \sqrt{\varepsilon_0}\, E_{0y}$, $\overline{H}_{0x} = \sqrt{\mu_0}\, H_{0x}$, $\overline{H}_{0y} = \sqrt{\mu_0}\, H_{0y}$, and $c = \frac{1}{\sqrt{\varepsilon_0\mu_0}}$ is the speed of light. When the column matrix representing the electromagnetic wave and the 4 × 4 matrix are $\boldsymbol{\Psi}(z)$ and $\mathbf{D}(z)$, respectively, Eq. (B.6) can be simplified as

$$\frac{\partial \boldsymbol{\Psi}(z)}{\partial z} = \frac{i\omega}{c}\mathbf{D}(z)\boldsymbol{\Psi}(z), \tag{B.7}$$

where $\mathbf{D}(z)$ is differential propagation matrix. If $\mathbf{D}(z)$ is not depend on z (the refractive index of a medium is not varied along the z-axis), Eq. (B.7) can be solved as

$$\boldsymbol{\Psi}(z) = \boldsymbol{\Psi}(0)e^{\frac{i\omega}{c}\mathbf{D}z}, \tag{B.8}$$

where, based on the Cayley-Hamilton theorem,

$$e^{\frac{i\omega}{c}\mathbf{D}z} = \sum_{n=0}^{\infty}\frac{1}{n!}\left(\frac{i\omega\Delta z}{c}\right)^n \mathbf{D}^n = \mathbf{P}(z,\Delta z), \tag{B.9}$$

where **P** is called a local propagation matrix. If the value of $\omega\Delta z/c$ is significantly smaller than 1 ($\omega\Delta z/c$ <<1), only three terms in Eq. (B.9) is sufficient to obtain an accurate solution. In the simulation the value of $\omega\Delta z/c$ can be also expressed as $2\pi\Delta z/\lambda n_o$, which has an order of 10^{-3} ~ 10^{-4} for the values used for simulation.

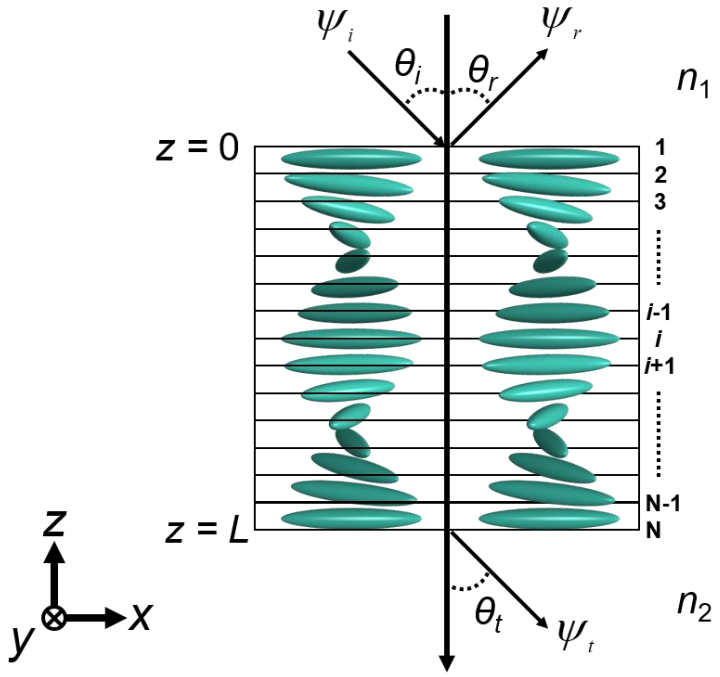


Figure B.1 A schematic of ChLC divided by slap for 4 × 4 calculation. The helical axis is along the z-axis. The incident angle is varied in the z-x plane. The dielectric tensor for each slap is assumed to be constant.

However, the dielectric tensor of ChLC is varied along the z-axis with helical modulation described in Eq. (1.5). Figure B.1 shows a schematic to obtain the propagation of light in ChLCs in which the $\mathbf{D}(z)$ is varied along the *z*-axis. The ChLC medium is divided into *N* slap with a sufficiently small thickness of Δz, and the dielectric tensor between *z* and $z + \Delta z$ is a constant value. The equation of light propagation in the slap can be derived from Eq. (B.7) and (B.9) as follows:

$$\boldsymbol{\Psi}(z+\Delta z)=\mathbf{P}(z,\Delta z)\boldsymbol{\Psi}(z). \tag{B.10}$$

If the total thickness of the ChLC is assumed as a length *L*, the electromagnetic field can be obtained by repeatedly solving Eq. (B.10) for each layer. Thus, the electromagnetic field at $z = L$ can be obtained by

$$\begin{aligned}\boldsymbol{\Psi}(z) &= \mathbf{P}(L,\Delta z)\mathbf{P}(L-\Delta z,\Delta z)\cdots\mathbf{P}(\Delta z,\Delta z)\mathbf{P}(0,\Delta z)\boldsymbol{\Psi}(0) \\ &= \mathbf{F}(L,\Delta z)\boldsymbol{\Psi}(0)\end{aligned}, \tag{B.11}$$

where

$$\mathbf{F}(L,\Delta z) = \mathbf{P}(L,\Delta z)\mathbf{P}(L-\Delta z,\Delta z)\cdots\mathbf{P}(\Delta z,\Delta z)\mathbf{P}(0,\Delta z). \tag{B.12}$$

Here, $\mathbf{F}(L,\Delta z)$ is called the propagation matrix.

The propagation matrix $\mathbf{F}(L,\Delta z)$ can provide various information of propagating light in a ChLC such as the eigenvalues and eigen-polarization. In addition, the reflection and transmission spectra can be obtained by considering the boundary conditions

$$\boldsymbol{\Psi}(0) = \boldsymbol{\Psi}_i + \boldsymbol{\Psi}_r \text{ and } \boldsymbol{\Psi}(L) = \boldsymbol{\Psi}_t, \tag{B.13}$$

where

$$\boldsymbol{\Psi}_i = \begin{pmatrix} E_{ip}\cos\theta_i \\ E_{ip}n_1 \\ E_{is} \\ -E_{is}n_1\cos\theta_i \end{pmatrix}, \boldsymbol{\Psi}_r = \begin{pmatrix} -E_{rp}\cos\theta_r \\ E_{rp}n_1 \\ E_{rs} \\ E_{rs}n_1\cos\theta_r \end{pmatrix}, \text{ and } \boldsymbol{\Psi}_t = \begin{pmatrix} E_{tp}\cos\theta_t \\ E_{tp}n_2 \\ E_{ts} \\ -E_{ts}n_2\cos\theta_t \end{pmatrix}. \tag{B.14}$$

Here, n_1 and n_2 is the refractive indices of the input and output media, and θ_i, θ_r (= θ_i), and θ_t $\left[=\sin^{-1}\left\{\left(n_1/n_2\right)\sin\theta_1\right\}\right]$ are the incident, reflected, and transmitted angles, respectively. In addition, E_i, E_r, and E_t indicate the electric field of the incident, reflected, and transmitted light, the *s*- and *p*-components of which are expressed by (E_{is}, E_{ip}), (E_{rs}, E_{rp}), and (E_{ts}, E_{tp}), respectively. By substituting Eq. (B.13) and (B.14) into Eq. (B.11), we can obtain

$$\begin{pmatrix} E_{tp}\cos\theta_t \\ E_{tp}n_2 \\ E_{ts} \\ -E_{ts}n_2\cos\theta_t \end{pmatrix} = \mathbf{F}\begin{pmatrix} \left(E_{ip}-E_{rp}\right)\cos\theta_i \\ \left(E_{ip}+E_{rp}\right)n_1 \\ \left(E_{ip}+E_{rs}\right) \\ \left(E_{ip}-E_{rs}\right)n_1\cos\theta_i \end{pmatrix}, \tag{B.15}$$

and

$$\begin{pmatrix} E_{tp}\cos\theta_t \\ E_{tp}n_2 \\ E_{ts} \\ -E_{ts}n_2\cos\theta_t \end{pmatrix} + \mathbf{F}\begin{pmatrix} E_{rp}\cos\theta_i \\ -E_{rp}n_1 \\ -E_{rs} \\ -E_{rs}n_1\cos\theta_i \end{pmatrix} = \mathbf{F}\begin{pmatrix} E_{ip}\cos\theta_i \\ E_{ip}n_1 \\ E_{is} \\ -E_{is}n_1\cos\theta_i \end{pmatrix}. \tag{B.16}$$

Equation (B.15) and (B.16) can be simplified by

$$\mathbf{G}\begin{pmatrix} E_{tp} \\ E_{ts} \\ E_{rp} \\ E_{rs} \end{pmatrix} = \mathbf{H}\begin{pmatrix} E_{ip} \\ E_{is} \end{pmatrix}, \tag{B.17}$$

where

$$\mathbf{G} = \begin{pmatrix} \cos\theta_t & 0 & F_{11}\cos\theta_i - F_{12}n_1 & -F_{13} - F_{14}n_1\cos\theta_i \\ n_2 & 0 & F_{21}\cos\theta_i - F_{22}n_1 & -F_{23} - F_{24}n_1\cos\theta_i \\ 0 & -1 & F_{31}\cos\theta_i - F_{32}n_1 & -F_{33} - F_{34}n_1\cos\theta_i \\ 0 & -n_2\cos\theta_t & F_{41}\cos\theta_i - F_{42}n_1 & -F_{43} - F_{44}n_1\cos\theta_i \end{pmatrix}, \tag{B.18}$$

$$\mathbf{H} = \begin{pmatrix} F_{11}\cos\theta_i + F_{12}n_1 & F_{13} - F_{14}n_1\cos\theta_i \\ F_{21}\cos\theta_i + F_{22}n_1 & F_{23} - F_{24}n_1\cos\theta_i \\ F_{31}\cos\theta_i + F_{32}n_1 & F_{33} - F_{34}n_1\cos\theta_i \\ F_{41}\cos\theta_i + F_{42}n_1 & F_{43} - F_{44}n_1\cos\theta_i \end{pmatrix}. \tag{B.19}$$

From Eq. (B.17), the information of electric field propagating through ChLCs such as the reflectance, transmittance, optical phase, and polarization state can be obtained. For example, the reflectance (R), transmittance (T), and optical phase can be obtained from

$$\mathrm{T} = \frac{\left|E_{tp}\right|^2 + \left|E_{ts}\right|^2}{\left|E_{ip}\right|^2 + \left|E_{is}\right|^2} \times \frac{n_2\cos\theta_t}{n_1\cos\theta_i}, \tag{B.20}$$

$$\mathrm{R} = \frac{\left|E_{rp}\right|^2 + \left|E_{rs}\right|^2}{\left|E_{ip}\right|^2 + \left|E_{is}\right|^2}, \tag{B.21}$$

$$\Phi_{rp} = \arg\left(E_{rp}\right), \tag{B.22a}$$

$$\Phi_{rs} = \arg\left(E_{rs}\right), \tag{B.22b}$$

$$\Phi_{tp} = \arg\left(E_{tp}\right), \tag{B.22c}$$

$$\Phi_{ts} = \arg\left(E_{ts}\right). \tag{B.22d}$$

where Φ_{rp}, and Φ_{rs} are the reflected optical phase of *p*- and *s*-components, and Φ_{tp} and Φ_{ts} are the transmitted optical phase of the *p*- and *s*-components, respectively.

Appendix B. Gerchberg-Saxton algorithm

Computer-generated holograms (CGHs) that make a desired diffraction pattern in an image plane have been numerically calculated using phase retrieval algorithms such as the Gerchberg-Saxton (G-S) [11, 12] and Yang-Gu (Y-G) [133] algorithms. Among them, the G-S algorithm is a powerful method used to find the phase-only information of propagating light in a homogeneous medium with a uniform intensity. It can be applied to HOEs based on the chiral liquid crystals (LCs) demonstrated in this dissertation because the chiral LCs show the capability to control the optical phase with a planar reflection intensity within the entire region. The implementation of the G-S algorithm is described in Fig. G.1. First, a light distribution on an image plane [$A'(X,Y)$] was prepared by combining a random phase distribution [$\Phi(X,Y)$] with a desired diffraction pattern [$a(X,Y)$] within a projection area of 512 × 384. The diffraction pattern in the image plane was converted into optical information [$U(x,y)=I(x,y)e^{i\Phi(x,y)}$] in an aperture plane through an inverse-Fourier transform. The amplitude of the optical information [$I(x,y)$] was then substituted into a uniform wave [$I'(x,y)$], and converted into a new diffraction pattern on the image plane through a Fourier transform [$A'(X,Y)=a'(X,Y)e^{i\Phi(X,Y)}$]. The diffraction pattern [$a'(X,Y)$] was replaced with the desired diffraction pattern (source image) [$a(X,Y)$], and again converted into the optical information in the aperture plane. This process was repeated 100 times to increase the similarity between the designed diffraction pattern (source image) and the reconstructed hologram from the fabricated devices. After repeating the algorithm, the phase-only information was converted into a helix or azimuthal orientation distribution by multiplying by a factor of 0.5.

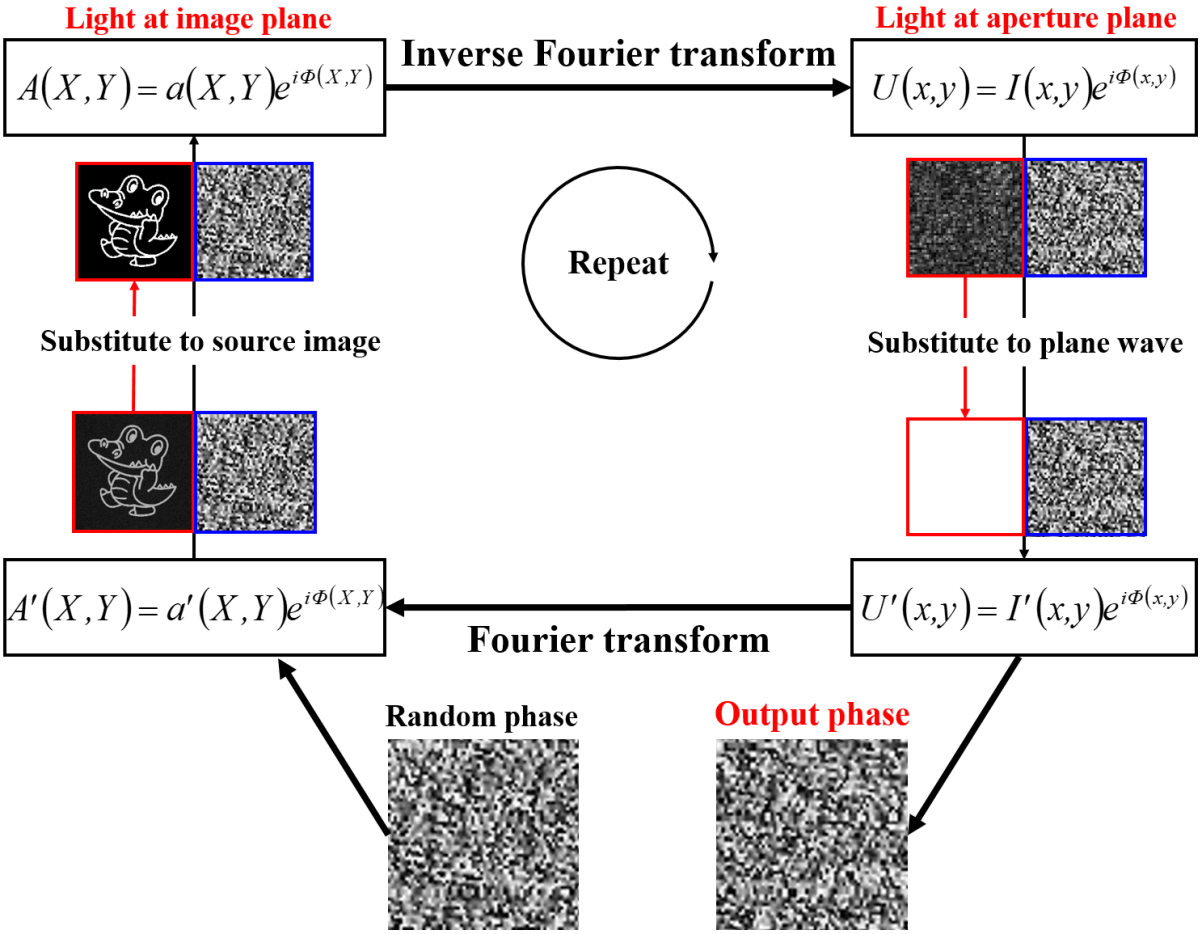


Figure C.1 A schematic of G-S algorithm.

Appendix C. Simulation of diffraction pattern

The diffraction pattern of the hologram devices can be simulated using scalar diffraction theory. This theory is described herein and it is shown how they can be used for the simulation of the diffraction patterns from HOEs using chiral LCs. Figure D.1 shows a schematic of the simulation for which a monochromatic light ($\lambda = 2\pi/k$) diffracted from the devices is propagated through a homogeneous medium along the z-axis. The devices are placed on an aperture plane at $z = 0$ with a pixel number and size of N_x and N_y, and Δx and Δy in the x-y plane, respectively. The electric field outside the aperture plane is assumed to be zero. The diffraction pattern is formed at an image plane placed at a distance of Δz from the aperture plane. The electric field in the aperture and image planes are indicated as $U(x, y, 0)$ and $U(X, Y, \Delta z)$, respectively.

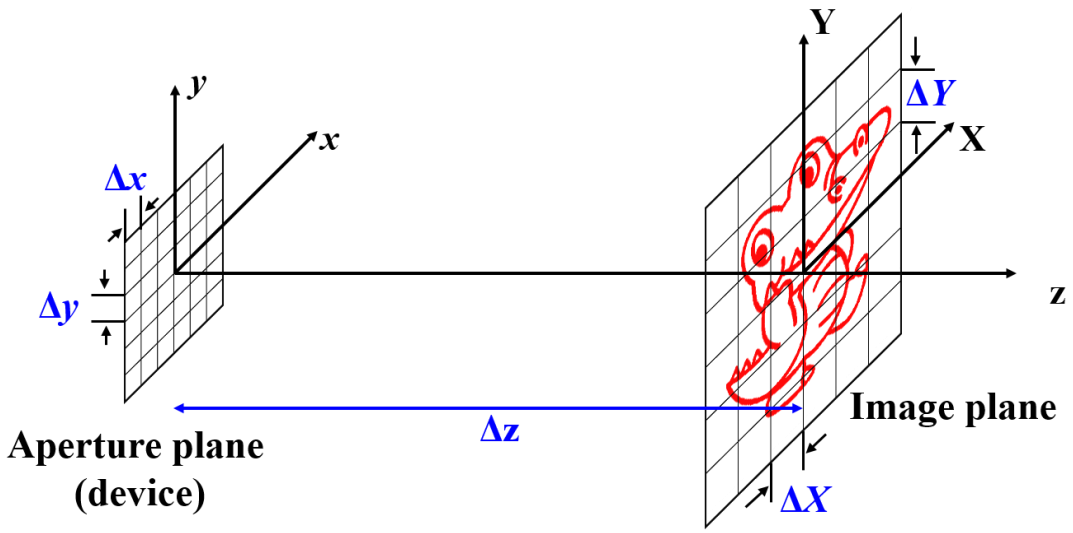


Figure D.1 A schematic for diffraction simulation. The light propagates from the aperture plane to the image plane through a homogeneous medium.

C. 1 Rayleigh-Sommerfeld diffraction

The most accurate method for simulating the diffraction pattern is Rayleigh-Sommerfeld diffraction integrals because they enable calculation of the diffraction pattern with a large angular direction [80, 83]. The light distribution at the aperture and image plane can be expressed in terms of a two-dimensional (2D) Fourier transform,

$$U(x,y,0) = \iint_A A(f_x, f_y, 0) e^{2\pi(f_x x + f_y y)} dxdy, \qquad \text{(D.1)}$$

where

$$A(f_x, f_y, 0) = \iint_A U(x, y, 0) e^{-2\pi(f_x x + f_y y)} dx dy, \tag{D.2}$$

for the light at the aperture plane, and

$$U(X, Y, z) = \iint_A A(f_X, f_Y, z) e^{2\pi(f_X X + f_Y Y)} dX dY, \tag{D.3}$$

where,

$$A(f_X, f_Y, z) = \iint_A U(X, Y, z) e^{-2\pi(f_X X + f_Y Y)} dX dY, \tag{D.4}$$

for the image plane. Here, $A(f_X, f_Y, z)$ is called the angular spectrum of $U(X, Y, z)$. The electric field must satisfy the Helmholtz equation, which is written as

$$\nabla^2 U(X, Y, z) + k^2 U(X, Y, z) = 0. \tag{D.5}$$

The substitution of Eq. (D.3) into the Helmholtz equation Eq. (D.5) yields

$$\iint \left[\frac{d^2}{dz^2} A(f_X, f_Y, z) + \left(k^2 - 4\pi^2 \left(f_X{}^2 + f_Y{}^2\right)\right) A(f_X, f_Y, z) \right] e^{i2\pi(f_X X + f_Y Y)} df_X df_Y = 0. \tag{D.6}$$

Eq. (D.6) is valid if the inside of the integral become zero. Thus, the solution can be obtained by solving the differential equation as

$$A(f_X, f_Y, z) = A(f_x, f_y, 0) G(x, y, z), \tag{D.7}$$

where

$$G(x, y, z) = e^{iz\sqrt{k^2 - 4\pi^2 \left(f_x{}^2 + f_y{}^2\right)}}, \tag{D.8}$$

where $G(x, y, z)$ is the optical transfer function, and its inverse Fourier transform is given by

$$\begin{aligned} g(x, y, z) &= FT^{-1}\{G(x, y, z)\} \\ &= \frac{1}{2\pi} \frac{\exp(ikr)}{r} \frac{\Delta z}{r} \left(\frac{1}{r} - ik \right), \end{aligned} \tag{D.9}$$

where FT and FT^{-1} are the operator of the Fourier and inverse-Fourier transform, and r is the distance from a point in the aperture plane to a point in an image plane expressed by

$$r = \sqrt{(X - x)^2 + (Y - y)^2 + \Delta z^2}. \tag{D.10}$$

In Eq. (D.7), the light field can be propagated in a homogeneous medium if $G(x, y, z)$ is larger than zero, and otherwise, the light is evanescent in the medium. Substituting Eq. (D.7) into (D.3) can be expressed by the following:

$$\begin{aligned} U(x, y, z) &= \iint A(f_x, f_y, 0) G(x, y, z) e^{i2\pi(f_x x + f_y y)} df_x df_y \\ &= FT^{-1}\left[FT\{U(x, y, 0)\} \times FT\{G(x, y, z)\} \right] \end{aligned}. \tag{D.11}$$

Based on the convolution theorem [80], Eq. (D.11) can be expressed as follows:

$$U(X,Y,z) = \iint_A U(x,y,0)\frac{\exp(ikr)}{2\pi r}\left(\frac{1}{r}-ik\right)\frac{\Delta z}{r}\,dxdy\,. \tag{D.12}$$

Eq. (D.12) is the R-S diffraction equation, which is valid for the diffraction of a propagating spherical wave in a homogeneous medium. Compared to the Fresnel and Fraunhofer diffraction theory described below, the R-S method is an exact solution for the diffraction pattern, which can be used when the distance between the aperture and image planes is longer than the wavelength of the propagating light. For a calculation of the pixelated CGH in Fig. 2.8 (b), the equation can be solved through a direct numerical integration with a discrete U (x, y, 0) in a sample grid, as through a Riemann summation:

$$U(X,Y,z) = \sum_{i=1}^{N_x}\sum_{j=1}^{N_y} U(x,y,0)\frac{\exp(ikr)}{2\pi r}\left(\frac{1}{r}-ik\right)\frac{\Delta z}{r}\Delta x\,\Delta y\,. \tag{D.13}$$

The discrete U (x, y, 0) was prepared by converting the helical phase distribution into a reflected optical phase based on the relationship described in Figs. 2.15 (b) and (c). The examples of an R-S diffraction are described in Section 2.6.

C.2 Fresnel diffraction

Although the R-S diffraction integral gives an accurate solution, the method is a quite complex and time-consuming to obtain the diffraction pattern. The theory can be approximated under a certain condition, allowing the calculations to be comparatively simple and fast. Here, I mathematically derive two approximations of the R-S theory, Fresnel and Fraunhofer diffraction theory, with a discussion regarding under what conditions they can be appropriately used [80].

The Fresnel diffraction is derived from the R-S equation in Eq. (D.12). Note that in the Fresnel equation, the propagating light is assumed as a parabolic wavefront. If the distance Δz is larger than the size of the aperture and image planes, that is,

$$(X-x)^2 + (Y-y)^2 << \Delta z\,, \tag{D.14}$$

the values of Δz and r are assumed to be equal, and the term $\frac{\exp(ikr)}{2\pi r}\left(\frac{1}{r}-ik\right)\frac{\Delta z}{r}$ in Eq. (D.12) can be simplified as $\frac{\exp(ikr)}{i\lambda\,\Delta z}$ (the value of $1/r$ is eliminated because the value of k is significantly larger than $1/r$). In addition, the point-to-point distance r can be expressed by a binominal expansion of a square root as

$$r = \sqrt{(X-x)^2 + (Y-y)^2 + \Delta z^2}$$
$$= z\left[1 + \frac{1}{2}\left\{\left(\frac{X-x}{z}\right)^2 + \left(\frac{Y-y}{z}\right)^2\right\} - \frac{1}{8}\left\{\left(\frac{X-x}{z}\right)^2 + \left(\frac{Y-y}{z}\right)^2\right\}^2 + \cdots\right]. \quad \text{(D.15)}$$

The number of terms in Eq. (D.15) relates to the accuracy of the calculation. Using a first term for the calculation, the distance r can be simplified as follows:

$$r \approx z\left[1 + \frac{1}{2}\left(\frac{X-x}{z}\right)^2 + \frac{1}{2}\left(\frac{Y-y}{z}\right)^2\right]. \quad \text{(D.16)}$$

By substituting Eq. (D.16) into Eq. (D.12), a simplified equation can be obtained as follows

$$U(X,Y,z) = \frac{e^{ik\Delta z}}{i\lambda\Delta z}\iint_A U(x,y,0)e^{i\frac{k}{2\Delta z}\left[(X-x)^2+(Y-y)^2\right]}dxdy. \quad \text{(D.17)}$$

Based on the convolution theorem, Eq. (D.17) is simplified into a Fresnel diffraction equation as

$$U(X,Y,z) = \frac{e^{ikz}e^{i\frac{k}{2z}\left(X^2+Y^2\right)}}{iz\lambda}\iint_A\left[U(x,y,0)e^{i\frac{k}{2z}\left(x^2+y^2\right)}\right]e^{-i\frac{2\pi}{z\lambda}(Xx+Yy)}dxdy. \quad \text{(D.18)}$$

The Fresnel diffraction can be simplified using a Fourier transform

$$U(X,Y,z) = \frac{e^{ikz}e^{i\frac{k}{2z}\left(X^2+Y^2\right)}}{iz\lambda}FT\left(U(x,y,0)e^{i\frac{k}{2z}\left(x^2+y^2\right)}\right). \quad \text{(D.19)}$$

Because the Fresnel diffraction is based on the Fourier transform of the light field in the aperture plane and multiplied by the quadratic terms, it is simple to quickly find the simulated diffraction pattern as compared to the R-S method. However, owing to the approximation in the Fresnel equation, there is a condition for the equation to be used. In Eq. (D.14), the second term has to be less than the first order for an accurate simulation. As a sufficient condition, the second term is less than 1 radian, which can be attained when the distance Δz satisfies

$$\Delta z^3 >> \frac{\pi}{4\lambda}\left[(X-x)^2 + (Y-y)^2\right]^2_{max}. \quad \text{(D.20)}$$

If the condition is satisfied, the Fresnel theory is valid and provide an accurate diffraction pattern on the image plane. The distance within which Eq. (D.20) is satisfied is called the near field of the aperture plane.

Figure D.2 shows an example of the Fresnel diffraction. The optical information at the aperture plane is prepared by integrating a uniform intensity with an optical phase distribution in Fig. 2.16 (a). The simulation was conducted using the wavelength of light (632 nm), the pixel

numbers (N_x = 512 and N_y = 384), the pixel sizes ($\Delta x = \Delta y$ = 2.7 μm), and various distance between the aperture and image plane. The distance for a calculation to be valid in this simulation is 18 cm, which is obtained from Eq. (D.20). Only a simulation pattern where the calculation distance is over 18 cm reconstructs the desired diffraction pattern, whereas the other patterns cannot reconstruct the hologram, or they show a high signal-to-noise ratio.

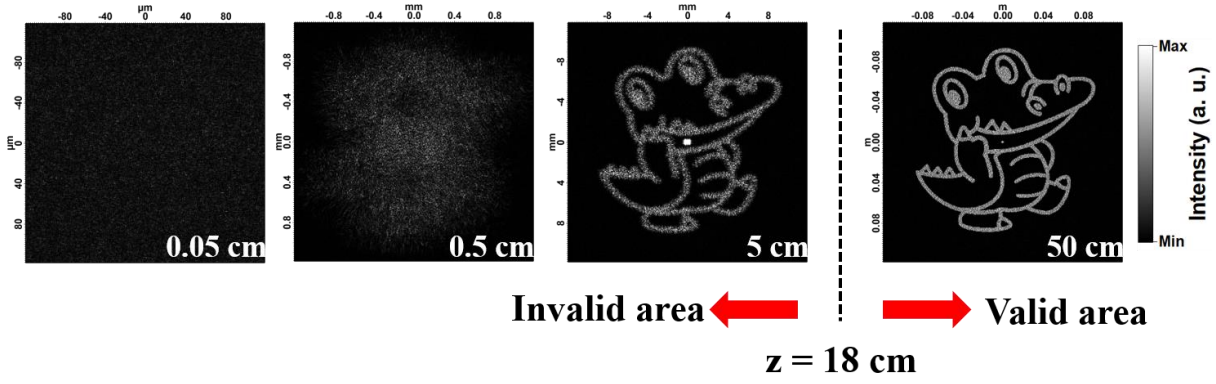


Figure D.2 An example of Fresnel diffraction. The correct pattern is created only when Eq. (D.20) is satisfied

C.3 Fraunhofer diffraction

The Fresnel diffraction can be also approximated when the quadratic terms in Eq. (D.19) are similar to 1 as shown in the following equation:

$$e^{i\frac{k}{2z}\left(x^2+y^2\right)} \approx 1. \tag{D.21}$$

Note that in the Fraunhofer equation, the propagating light is assumed as a planar wavefront. In this case, Eq. (D.19) can be simplified as

$$U(X,Y,z) = \frac{e^{ikz}e^{i\frac{k}{2z}\left(X^2+Y^2\right)}}{iz\lambda}\iint_A U(x,y,0)e^{-i\frac{2\pi}{z\lambda}(Xx+Yy)}\,dxdy. \tag{D.22}$$

This equation is called as Fraunhofer diffraction, enabling a far-field diffraction pattern to be simulated. Eq. (D.22) can be simplified using a Fourier transform as

$$U(X,Y,z) = \frac{e^{ikz}e^{i\frac{k}{2z}\left(X^2+Y^2\right)}}{iz\lambda}FT\left[U(x,y,0)\right]. \tag{D.23}$$

The condition for Eq. (D.23) to be used is obtained from Eq. (D.21) and expressed by

$$\Delta z >> \frac{k}{2z}\left(x^2+y^2\right). \tag{D.24}$$

If the condition is satisfied, the Fraunhofer theory is valid and provides an accurate diffraction pattern on the image plane. The distance where Eq. (D.24) is satisfied is called the far-field region of the aperture plane.

Figure D.3 shows an example of the Fraunhofer diffraction. The optical information at the aperture plane is prepared by integrating an intensity distribution in Fig. D.3 (a) with an optical phase distribution in Fig. D.3 (b) with a grating period of 25 μm. The simulation was performed with the wavelength of light (λ = 632 nm), the pixel numbers (N_x = 512 and N_y = 384), the pixel sizes ($\Delta x = \Delta y$ = 2.7 μm), and a distance of 20 m to satisfy Eq. (D.24). As shown in Figs. D.3 (c) and (d), the light is deflected at a distance of 0.5 m from the zero-order light, giving a deflection angle of 1.4°. This value is well-matched with a value obtained by an equation for deflection angle of grating devices, that is $\theta_d = \sin^{-1}(\lambda/\Lambda)$, where θ_d and Λ are the deflection angle and the grating period, respectively.

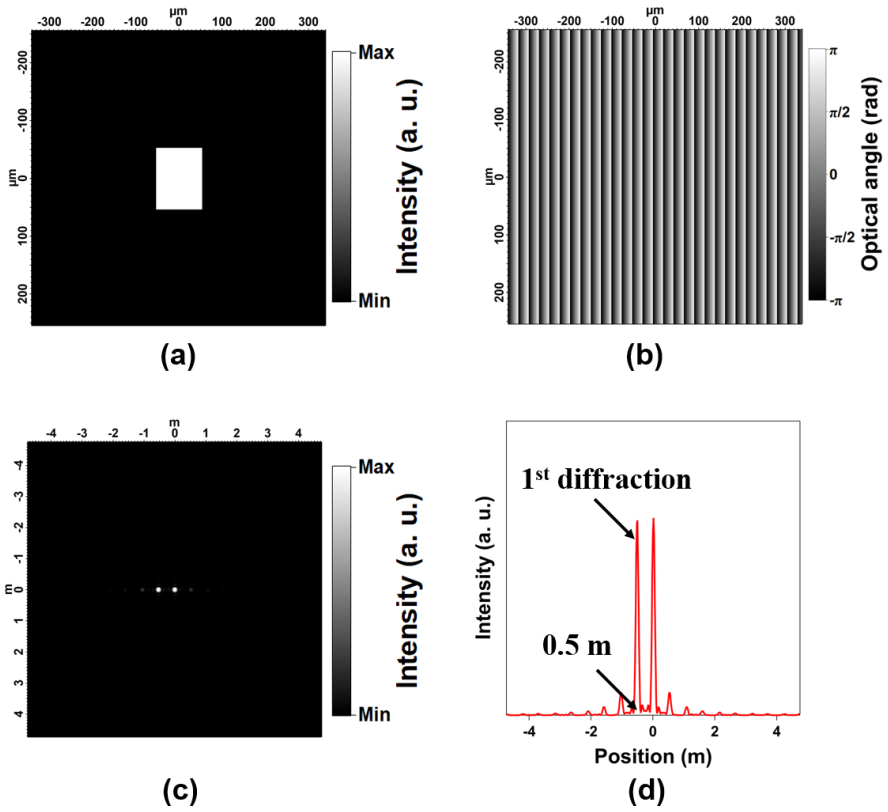


Figure D.3 Simulation of Fraunhofer diffraction. (a) Intensity and optical phase distribution at aperture plane. (c) Simulated 2D diffraction pattern through Fraunhofer diffraction. (d) Diffracted light intensity in horizontal axis of the 2D pattern.

As such, R-S diffraction can always provide an accurate solution if the calculation distance is larger than the wavelength of propagating light, but the calculation is complicated. The diffraction patterns simulated in Fig. 2.17 through the R-S diffraction have took 12 h to generate for each pattern. Fresnel and Fraunhofer diffraction give an accurate solution only under certain conditions, but the calculation is easy and fast. The simulation can be finished within 1 min, but cannot be applied to Fig. 2.17 because the distance is quite short.